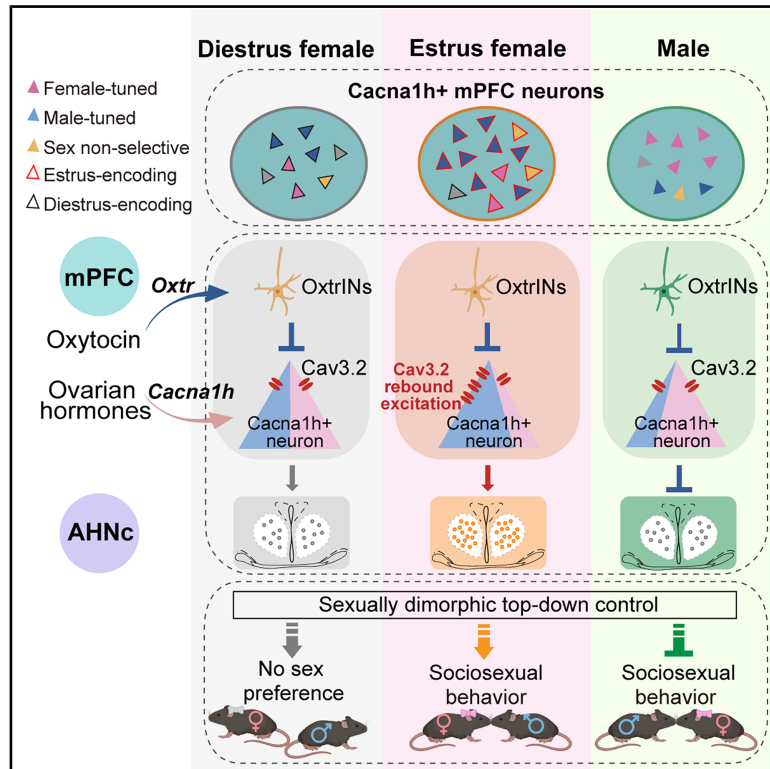


Integrating reproductive states and social cues in the control of sociosexual behaviors

Graphical abstract



Authors

Yuping Wang, Xinli Song, Xiangmao Chen, ..., Xiaoxuan Jia, Nathaniel Heintz, Kun Li (李坤)

Correspondence

heintz@rockefeller.edu (N.H.), kli@mail.tsinghua.edu.cn (K.L.)

In brief

A subset of neurons in the medial prefrontal cortex is shown to exert top-down regulation of adaptive innate reproductive behaviors by integrating social cues with estrous states to orchestrate sociosexual behaviors.

Highlights

- *Cacna1h*-defined estrous-tracking mPFC neurons drive sex-specific sociosexual behavior
- *Cacna1h*+ neurons selectively tune to opposite-sex cues in estrus females and males
- *Cacna1h* elevation drives T-type rebound for dynamic encoding of estrus and male cues
- mPFC-AHN circuits exert sexually dimorphic top-down control of sociosexual behavior

Article

Integrating reproductive states and social cues in the control of sociosexual behaviors

Yuping Wang,^{1,4} Xinli Song,^{1,4} Xiangmao Chen,^{3,4} Ying Zhou,^{1,4} Jihao Ma,^{1,4} Fang Zhang,^{1,4} Liqiang Wei,^{1,4} Guoxu Qi,¹ Nakul Yadav,² Benjie Miao,¹ Yiming Yan,¹ Guohua Yuan,¹ Da Mi,¹ Priyamvada Rajasethupathy,² Ines Ibañez-Tallon,² Xiaoxuan Jia,¹ Nathaniel Heintz,^{2,*} and Kun Li (李坤)^{1,5,*}

¹IDG/McGovern Institute for Brain Research at Tsinghua, Tsinghua-Peking Center for Life Sciences, School of Life Sciences, Tsinghua University, Beijing 100084, China

²The Rockefeller University, 1230 York Avenue, New York, NY 10065, USA

³Academy for Advanced Interdisciplinary Studies, Peking University, Beijing 100871, China

⁴These authors contributed equally

⁵Lead contact

*Correspondence: heintz@rockefeller.edu (N.H.), kli@mail.tsinghua.edu.cn (K.L.)

<https://doi.org/10.1016/j.cell.2025.04.035>

SUMMARY

Female sociosexual behaviors, essential for survival and reproduction, are modulated by ovarian hormones and triggered in the context of appropriate social cues. Here, we identify primary estrous-sensitive Cacna1h -expressing medial prefrontal cortex (mPFC ^{Cacna1h^+}) neurons that integrate hormonal states with recognition of potential mates to orchestrate these complex cognitive behaviors. Bidirectional manipulation of mPFC ^{Cacna1h^+} neurons shifts opposite-sex-directed social behaviors between estrus and diestrus females via anterior hypothalamic outputs. In males, these neurons serve opposite functions compared with estrus females. Miniscope imaging reveals mixed representation of self-estrous states and social target sex in distinct mPFC ^{Cacna1h^+} subpopulations, with biased encoding of opposite-sex cues in estrus females and males. Mechanistically, ovarian-hormone-induced Cacna1h upregulation enhances T-type rebound excitation after oxytocin inhibition, driving estrus-specific activity changes and the sexually dimorphic function of mPFC ^{Cacna1h^+} neurons. These findings uncover a prefrontal circuit that integrates internal hormonal states and target-sex information to exert sexually bivalent top-down control over adaptive social behaviors.

INTRODUCTION

Ovarian hormone fluctuations intricately orchestrate female internal physiological states^{1,2} and distinctly influence sex-specific social and emotional responses,^{3–5} significantly contributing to the observed sex disparities in psychiatric disorder susceptibilities.^{6–8} Across species, female social preference and sexual receptivity toward males are synchronized with the estrous cycle, specifically ovulation, optimizing reproductive success.⁹ This suggests that female brains integrate social cues related to sex with their reproductive states to guide adaptive sociosexual interactions, such as social approach, investigation, avoidance, or sexual receptivity toward males.^{10–13}

Female adaptive sociosexual behaviors toward males require flexible adjustment across estrous states, aligning with the role of the mPFC in integrating diverse information¹⁴ and modulating behavioral flexibility.¹⁵ The mPFC, a critical node in the social brain network, governs various aspects of social behavior, including social recognition,¹⁶ investigation,¹⁷ representation of conspecific sex,¹⁸ and perception of social status.¹⁹ The mPFC receives substantial inputs from olfactory pathways and projects to discrete subcortical areas mediating social reward,

memory, aggression, and avoidance.^{20,21} The evidence above suggests that the mPFC may exert a top-down role in the social brain network by integrating internal and external social contexts and controlling hardwired subcortical circuits to guide adaptive social behaviors.

Neuroimaging studies in humans have linked mPFC activity fluctuations to cognitive stimuli throughout the menstrual cycle.^{22,23} Functional MRI studies in female rats have shown that the estrous cycle significantly alters neural activity across the brain.^{23,24} The estrous cycle has been shown to modulate stress-triggered immediate early gene (IEG) expression, dendritic remodeling, synaptic plasticity, and behavioral responses to stress in the mPFC.^{25–27} Specifically, conditional deletion of the *Oxtr* gene or *Oxtr*+/Sst+ interneurons (*Oxtr*INs) in the mPFC attenuates females' social preference for males during estrus, emphasizing the mPFC's significant role in estrus-specific sociosexual preference.³ Yet, how mPFC neurons encode self-estrous states and integrate external social cues with self-estrous states to adaptively regulate sociosexual behaviors in females remains unknown.

To address this critical knowledge gap, we employed comprehensive, unbiased screening techniques to identify a subset of

Cacna1h-expressing layer 5 pyramidal tract (L5_PT) neurons in the mPFC (mPFC^{Cacna1h+} neurons) that exhibit high sensitivity to estrous cycle changes in gene expression and neuronal activity. Through bidirectional neural modulation, *in vivo* calcium imaging, computational analysis, and mechanistic investigations, we demonstrate that mPFC^{Cacna1h+} neurons integrate social cues with self-estrous states to orchestrate increased male-directed sociosexual behaviors in estrus females, while conversely suppressing female-directed behaviors in males. We further provide circuit, cellular, and molecular mechanistic insights into the estrus-dependent and sex-specific cortical mechanisms. These findings offer insights into the top-down regulation of adaptive innate reproductive behaviors. The sexually bivalent roles of estrous-sensitive mPFC^{Cacna1h+} neurons and the *Cacna1h* gene suggest that prefrontal dysfunction may underlie the high prevalence of hypersexuality in males and hypo-sexuality in females, elucidating the neural basis of sexual dimorphism and highlighting potential therapeutic targets for sexual disorders.

RESULTS

Estrous cycle shapes mPFC neural type transcriptomes

To characterize mPFC neurons responsive to estrous cycle changes, we performed single-cell RNA sequencing (scRNA-seq) on adult mPFC samples from estrus females, diestrus females, and males (Figure 1A). t-distributed stochastic neighbor embedding (t-SNE) analysis identified six excitatory and four inhibitory neuron clusters, annotated by established gene markers (Figures 1B and 1C).^{28,29} Estrogen receptor expression was low, while progesterone and androgen receptors were broadly distributed across neuronal types (Figure 1D). Differentially expressed gene (DEG) analysis revealed that L5_PT, Parvalbumin+, and Lamp5+ interneurons exhibited the highest DEG counts between estrus and diestrus (Figure S1F).

To examine how ovarian hormone fluctuations influence neural activity indicated by transcriptomic changes, we analyzed the expression of IEG networks known to be regulated by ovarian hormones.^{30–32} L5_PT neurons exhibited the most dramatic IEG network changes between estrus and diestrus, indicating high sensitivity in neural activity to ovarian hormone changes during the diestrus-to-estrus transition (Figure 1E). To assess functional implications, we analyzed DEG clusters between estrus and diestrus across cell types using hierarchical clustering and Gene Ontology (GO)-term analysis. In L5_PT neurons, top enriched pathways included synaptic organization, protein phosphorylation, and GTPase activity (Figure S1I), suggesting estrous-cycle-dependent synaptic plasticity. Moreover, L5_PT neurons exhibited the highest DEG count between diestrus females and males (Figure S1F) and predominantly project to the hypothalamus,^{28,29} further supporting their role in sex-specific social behaviors.

Cacna1h-defined L5_PT neurons connecting OxtRINs and AHN sense estrous status by strengthening synaptic efficacy under hyperpolarization

To identify estrus-sensitive cell types involved in female sociosexual behaviors, we employed additional multi-faceted screening approaches. Previous work reported that OxtRINs in the mPFC are essential for female sociosexual preference during estrus,³ exerting stronger inhibition on layer 5 pyramidal neurons in females than in males.³³ As *Oxtr* mRNA expression remains constant across the estrous cycle (Figure S1O), we hypothesized that layer 5 pyramidal neurons receiving OxtRIN input may integrate estrous-state signals to regulate sociosexual behaviors.

To map OxtRIN-connected mPFC projection populations, we expressed a Cre-dependent, anterograde polysynaptic tracer H129ΔTK-TT³⁴ in the mPFC of *Oxtr*-Cre ON82 transgenic mice³ (Figure 1F). Labeled projections were enriched in subcortical regions (Figures 1F and S1J), with the central part of the anterior hypothalamic nucleus (AHNc) showing significantly

(F) Anterograde polysynaptic tracing of OxtRINs in the mPFC (left). Right: representative images depicting the downstream outputs are located within the lateral hypothalamus (LH), the central part of the anterior hypothalamic nucleus (AHNc), the parataenial thalamic nucleus (PT), the mediodorsal nucleus of the thalamus (MD), the anteromedial thalamic nucleus (AM), the basolateral amygdala (BLA), the basomedial amygdala (BMA), the claustrum (CLA), and the anterior piriform cortex (APC). Scale bar, 200 μm. DAPI, blue.

(G) Quantification of c-Fos+ cell counts triggered by sociosexual preference behavior across different brain regions in estrus and diestrus females ($n = 3$ mice/group).

(H) Immunofluorescence images of c-Fos expression in the AHNc activated by sociosexual preference behavior during diestrus (left) and estrus (right). Scale bar, 200 μm.

(I) The strategy for measuring synaptic connectivity between OxtRINs and mPFC^{AHNc-projecting} neurons (left). Percentage of responsive cells in AHN-projecting and non-AHN-projecting layer 5 pyramidal neurons upon OxtRINs activation (right). $n = 21$ –29 cells/group. AAV, adeno-associated virus.

(J) Example traces showing the light-evoked monosynaptic excitatory and inhibitory connectivity between OxtRINs and mPFC^{AHNc-projecting} neurons (left). Comparison of the amplitudes of light-evoked IPSCs and EPSCs in mPFC^{AHNc-projecting} neurons between estrus and diestrus females (right). $n = 60$ –67 cells/group (right). Two-way ANOVA, Bonferroni multiple comparisons tests.

(K) sEPSC recording in AHNc-projecting and non-AHNc-projecting mPFC neurons. Cumulative probability of frequency (left) and amplitude (middle) and representative traces (right) of sEPSCs. Insets in cumulative probability graphs represent average sEPSC frequency (left) and amplitudes (middle). One-way ANOVA, Bonferroni multiple comparisons tests.

(L) Summarized data of RMP recorded from mPFC^{AHNc-projecting} neurons. $n = 8$ –24 cells/group. Two-way ANOVA, Bonferroni multiple comparisons tests.

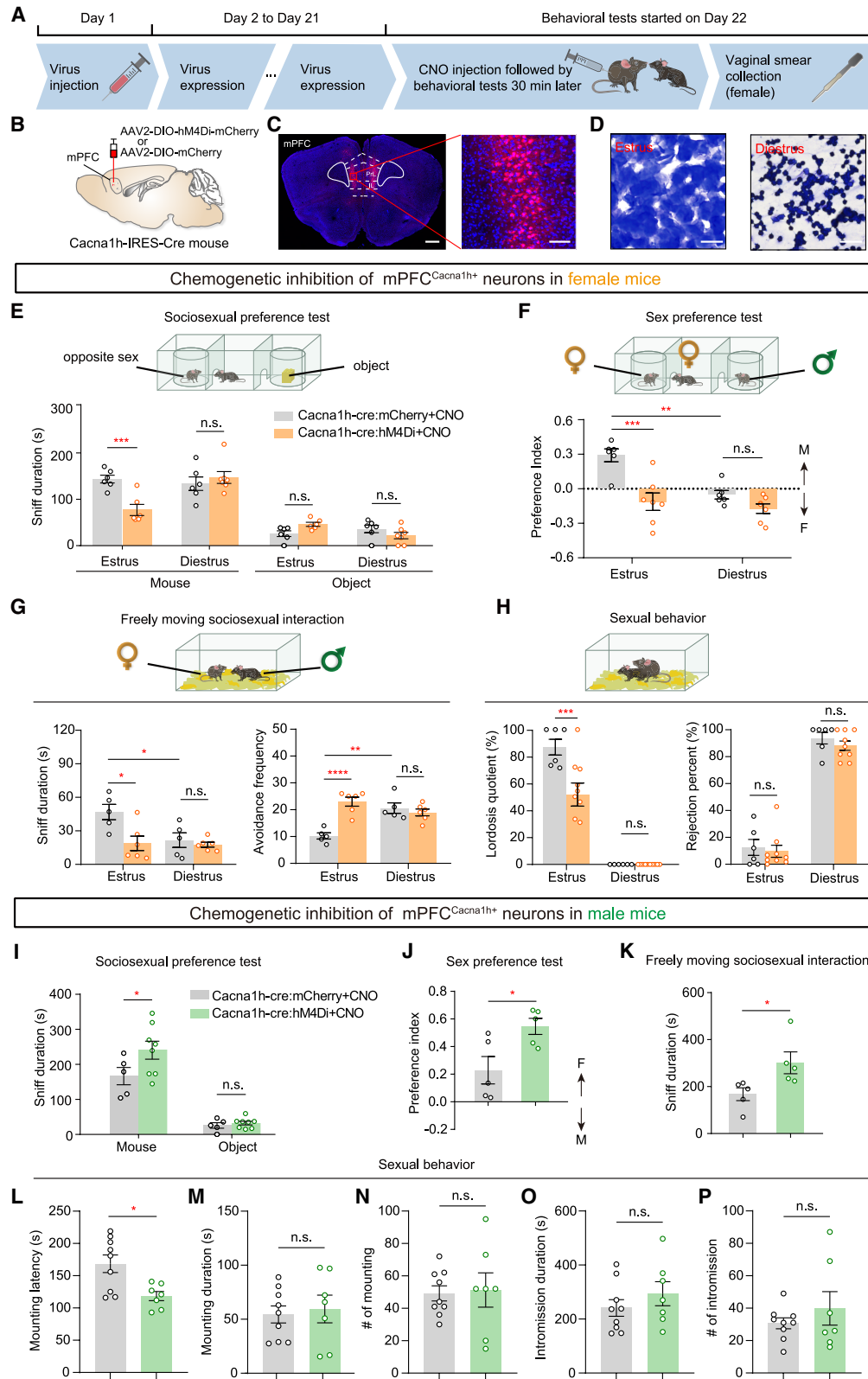
(M) Profiling translating mRNAs in mPFC^{AHNc-projecting} neurons using pathway-specific TRAP-seq. Right: scatterplot of TRAP-seq results showing normalized counts from INPUT (x axis) and immunoprecipitation (IP) (y axis). Dots represent individual genes (blue, significantly enriched genes in IP; red dot, *Cacna1h* gene).

(N) Coronal sections showing the expression of EGFP-Rpl10a (green) and *Cacna1h* mRNA (magenta) in the mPFC. Scale bar, 200 μm.

(O) Violin plot showing *Cacna1h* gene expression across mPFC neuronal types.

* $p < 0.05$, ** $p < 0.01$, *** $p < 0.001$; n.s., not significant; data represent mean \pm SEM.

See also Figure S1.



(legend on next page)

increased c-Fos+ activation during sociosexual preference in estrus females (Figures 1G and 1H). Notably, nearly all layer 5 mPFC neurons projecting to the anterior hypothalamic nucleus (AHN) responded to OxtrIN activation (Figure 1I). The AHN, a component of a sexually dimorphic nucleus complex in many species,^{35–37} is crucial for female rats' sexual behavior³⁸ and ovulation,³⁹ as lesions disrupt mating behavior,³⁸ and muscarinic receptor blockade prevents ovulation by suppressing ovarian follicular formation.³⁹ These results suggest that OxtrINs-innervated, AHNc-projecting layer 5 mPFC neurons (mPFC^{AHNc-projecting}) may play an estrus-dependent role in regulating female sociosexual behaviors.

To determine whether the electrophysiological properties of mPFC^{AHNc-projecting} neurons change over the estrous cycle, we performed whole-cell recordings. Optogenetic activation of OxtrINs evoked predominantly inhibitory postsynaptic currents (IPSCs) in mPFC^{AHNc-projecting} neurons in the presence of tetrodotoxin (TTX) and 4-aminopyridine (4-AP), confirming their monosynaptic inhibition (Figure 1J). The amplitude of light-evoked currents (Figure 1J) and the paired-pulse ratio (PPR) (Figure S1Q) did not differ between estrus and diestrus, indicating stable presynaptic neurotransmitter release. However, the frequency and amplitude of spontaneous excitatory postsynaptic currents (sEPSCs) recorded in the absence of TTX were significantly potentiated in the mPFC^{AHNc-projecting} neurons specifically during estrus (Figure 1K), suggesting that postsynaptic mPFC^{AHNc-projecting} neurons may primarily track estrous states in females. Notably, these neurons were more hyperpolarized in estrus females than in diestrus females and males (Figure 1L). In keeping with *Oxtr+* mRNA being predominantly enriched in inhibitory *Sst+* neurons (Figures S1L–S1N), oxytocin further hyperpolarized mPFC^{AHNc-projecting} neurons in diestrus but had no additional effect in estrus (Figure 1L), indicating an occluding hyperpolarized state during estrus. Importantly, the estrus-associated increase in synaptic efficacy was observed only in hyperpolarized mPFC^{AHNc-projecting} neurons and not in other layer 5 pyramidal neurons (Figure 1K), highlighting their estrous-cycle-dependent regulation.

To identify genes underlying estrus-dependent electrophysiological changes in mPFC^{AHNc-projecting} neurons, we employed a pathway-specific translating ribosome affinity purification (TRAP) approach to profile the translating mRNAs of these neurons (Figure 1M). Using three criteria—(1) expression in deep mPFC layers, (2) a potential role in synaptic potentiation under hyperpolarization, and (3) involvement in social behavior—we identified *Cacna1h* as the only candidate fulfilling all criteria. *Cacna1h*, highly expressed in layer 5 pyramidal neurons of the mPFC (Figure 1N), encodes the Cav3.2 T-type voltage-gated calcium channel, which facilitates calcium influx near the resting membrane potential (RMP).^{40,41} It has been implicated in hyperpolarization-induced synaptic potentiation,⁴² synaptic upscaling under TTX-mediated suppression,⁴³ and autism spectrum disorders in humans.^{44,45} Given this evidence, we hypothesized that *Cacna1h* may contribute to the synaptic strength potentiation in hyperpolarized mPFC^{AHNc-projecting} neurons during estrus.

scRNA-seq identified *Cacna1h* as a gene marker of L5_PT neurons (Figure 1O). Notably, these neurons exhibit the most pronounced changes in DEGs (Figure S1F), ovarian hormone-regulated IEG network (Figure 1E), and synapse-related gene modules between estrous cycle transitions (Figure S1I). Electrophysiologically, mPFC^{Cacna1h+} neurons closely resemble mPFC^{AHNc-projecting} neurons during estrus, characterized by enhanced synaptic efficacy and hyperpolarized membrane potential (Figures S1T and S1U). Taken together, these findings suggest that OxtrIN-innervated, *Cacna1h*-expressing L5_PT neurons projecting to the AHN are highly sensitive to estrous-state transitions and may regulate estrus-dependent sociosexual behaviors.

mPFC^{Cacna1h+} neurons bidirectionally regulate sociosexual behaviors in estrus-dependent and sexually dimorphic manners

To assess the role of mPFC^{Cacna1h+} neurons in opposite-sex sociosexual behaviors, we expressed the inhibitory chemogenetic receptor hM4Di in these neurons in male and female *Cacna1h*-IRES-Cre mice and conducted behavioral assays to evaluate

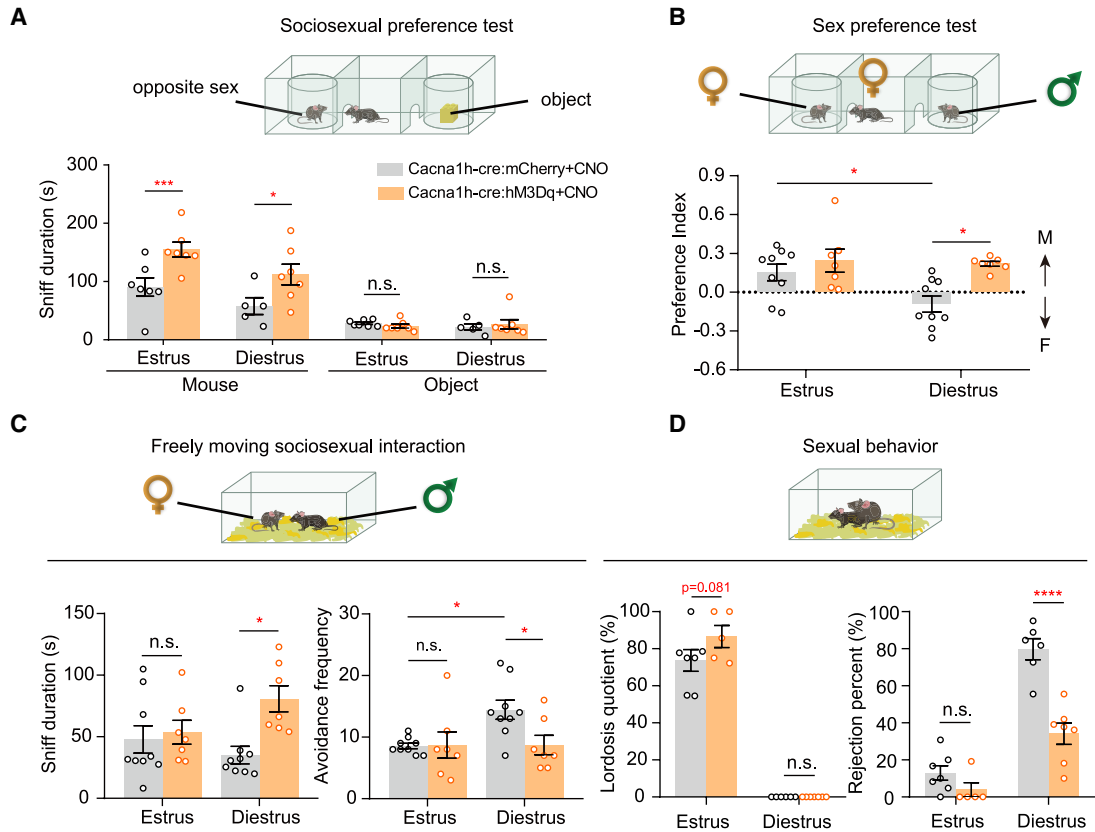
Figure 2. Chemogenetic inhibition of mPFC^{Cacna1h+} neurons suppresses sociosexual behaviors in estrus females but enhances them in males

- (A) Timeline of behavioral testing for female and male *Cacna1h*-IRES-Cre mice.
(B) Schematic of virus injection into the mPFC of *Cacna1h*-IRES-Cre mice.
(C) Representative coronal section showing hM4Di-mCherry expression (magenta) in the mPFC^{Cacna1h+} neurons. Scale bars, 500 μ m (left) and 100 μ m (right).
(D) Representative vaginal cytology images illustrating estrus and diestrus stages. Scale bar, 25 μ m.
(E) Sociosexual preference assay (top). Quantification of sniffing behaviors toward male or object (bottom). $n = 6$ –7 mice/group. Two-way ANOVA, Bonferroni multiple comparisons tests.
(F) Sex preference assay (top). Quantification of sniffing preference index toward male or female stimuli (bottom). $n = 6$ –7 mice/group. Two-way ANOVA, Bonferroni multiple comparisons tests.
(G) Freely moving opposite-sex social interaction assay (top). Quantification of female-initiated social interactions (bottom left) and frequency of female avoidance responses to male approaches (bottom right). $n = 5$ –6 mice/group. Two-way ANOVA, Bonferroni multiple comparisons tests.
(H) Female sexual receptivity assessment (top). Quantification of the lordosis quotient (bottom left) and the percentage of male mating attempts rejected by females (bottom right). $n = 6$ –9 mice/group. Two-way ANOVA, Bonferroni multiple comparisons tests.
(I–K) Quantification of male social behaviors. Sniffing behaviors toward female or object in the sociosexual preference assay (I), sniffing preference index for male vs. female stimuli in the sex preference assay (J), and male-initiated interaction duration with females during freely moving social interaction (K). $n = 5$ –8 mice/group. Two-way ANOVA, Bonferroni multiple comparisons tests for (I), two-tailed unpaired t test for (J) and (K).
(L–P) Quantification of male sexual behavior parameters, including mounting latency (L), mounting duration (M), number of mounts (N), intromission duration (O), and number of intromissions (P). $n = 7$ –9 mice/group. Two-tailed unpaired t test.

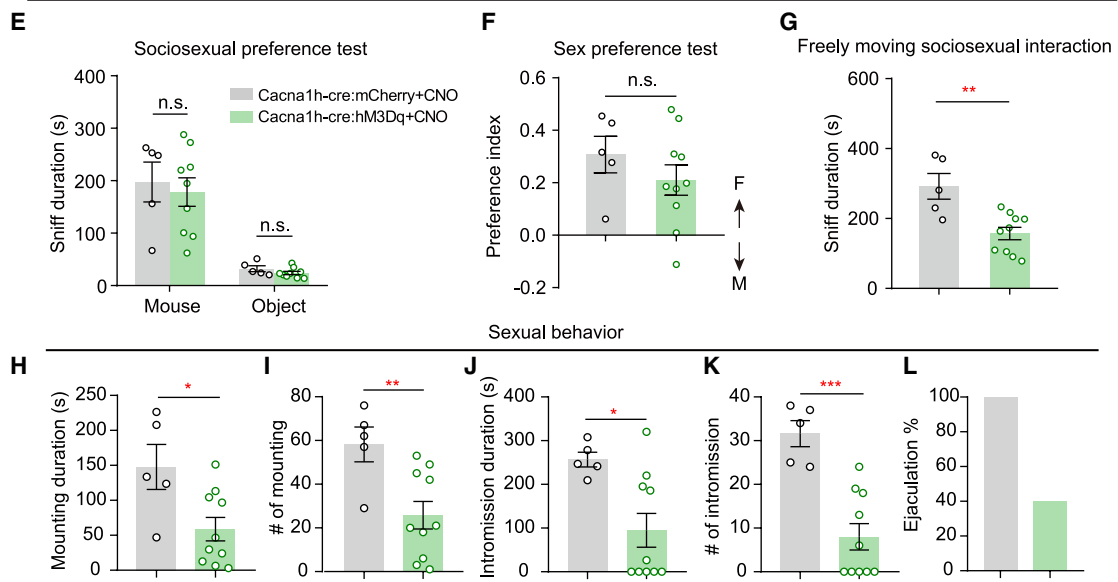
* $p < 0.05$, ** $p < 0.01$, *** $p < 0.001$, **** $p < 0.0001$; n.s., not significant; data represent mean \pm SEM.

See also Figure S2.

Chemogenetic activation of mPFC^{Cacna1h+} neurons in female mice



Chemogenetic activation of mPFC^{Cacna1h+} neurons in male mice



(legend on next page)

sociosexual interest and sexual behavior (Figures 2A–2C). Following behavioral testing, estrous phases of experimental females were determined via blinded vaginal cytology analysis (Figure 2D).

In sociosexual preference assays, female mice chose between a cup-restrained male and a novel object. Silencing mPFC^{Cacna1h+} neurons reduced male-directed sniffing by 47% exclusively in estrus females, with no effect in other estrous phases (Figures 2E and S2L). Estrus females exhibited a marked preference for sexually experienced males over females during the sex preference test, which was absent in diestrus (Figure 2F). Chemogenetic inhibition of mPFC^{Cacna1h+} neurons significantly attenuated this estrus-driven male preference, reducing the preference index by 139% in hM4Di-expressing estrus females compared with controls (Figure 2F). During free social interactions, estrus females displayed increased investigation time and reduced avoidance toward males compared with diestrus females (Figure 2G). Silencing mPFC^{Cacna1h+} neurons selectively reduced estrus female-initiated interactions with males and increased avoidance in response to male pursuit (Figure 2G). To assess their role in sexual receptivity, females at different estrous stages were introduced to sexually primed males. Inhibition of mPFC^{Cacna1h+} neurons suppressed estrus-specific sexual receptivity, as evidenced by a reduced lordosis quotient (Figure 2H).

Conversely, silencing mPFC^{Cacna1h+} neurons in males increased female-directed investigation in both sociosexual and sex preference assays, markedly enhancing interactions with freely moving females (Figures 2I–2K). Chemogenetic inhibition also reduced mounting latency by 30%, indicating heightened sexual motivation (Figure 2L). However, suppression of mPFC^{Cacna1h+} neurons had no significant effect on mounting frequency, intromission duration, or ejaculation latency (Figures 2M–2P).

To assess whether mPFC^{Cacna1h+} neurons drive sociosexual interest and sexual receptivity in females, we chemogenetically activated these neurons by expressing hM3Dq in Cacna1h-IRES-Cre mice. Activation increased female-initiated investigation toward males across both estrus and diestrus and induced estrus-like male preference in diestrus females (Figures 3A and 3B). It also significantly enhanced male-directed investigation,

reduced avoidance during free interactions (Figure 3C), and lowered rejection rates during male mounting attempts in the sexual behavior test in diestrus females (Figure 3D). In males, however, activation of mPFC^{Cacna1h+} neurons significantly reduced interaction duration with females without altering female preference (Figures 3E–3G). Notably, increased mPFC^{Cacna1h+} activity strongly suppressed male sexual behaviors, reducing mounting and intromission duration and frequency, as well as markedly decreasing ejaculation incidence (Figures 3H–3L).

Collectively, these findings unveil the pivotal role of mPFC^{Cacna1h+} neurons in orchestrating sociosexual behaviors, including opposite-sex preference, interaction, and copulatory behaviors, in estrus-specific and sexually dimorphic manners.

The representation of target sex by mPFC^{Cacna1h+} neurons is estrus dependent and sex specific

To examine the neural response of mPFC^{Cacna1h+} neurons during sociosexual preference behavior, we performed fiber photometry in Cacna1h-IRES-Cre mice expressing the genetically encoded calcium indicator GCaMP6f via AAV-Flex-GCaMP6f in the mPFC (Figures S3A and S3B). These recordings revealed distinct mPFC^{Cacna1h+} neuron responses to opposite-sex conspecifics and novel objects. In estrus females, activity decreased before sniffing males and then increased fivefold during sniffing compared with diestrus (Figures S3E and S3F). This response was absent during novel object exploration (Figures S3H and S3I). By contrast, males exhibited a modest decreasing trend in activity when sniffing females (Figure S3L).

To further dissect the estrus- and sex-dependent encoding of social cues by mPFC^{Cacna1h+} neurons at the single-neuron level, we performed micro-endoscopic calcium imaging in Cacna1h-IRES-Cre mice of both sexes (Figures 4A–4C). The calcium dynamics of GCaMP7b-expressing mPFC^{Cacna1h+} neurons were recorded during sociosexual and sex preference behaviors (Figures 4D and 4H).

During sociosexual preference tests (Figure 4D), mPFC^{Cacna1h+} neurons responsive to opposite-sex targets significantly outnumbered those responding to non-social objects in both sexes (Figures 4E–4G). While the proportions of socially tuned neurons were similar across groups, opposite-sex stimuli suppressed a greater percentage of mPFC^{Cacna1h+} neurons in diestrus females

Figure 3. Chemogenetic activation of mPFC^{Cacna1h+} neurons elevates sociosexual behaviors in diestrus females but suppresses them in males

(A) Sociosexual preference assay. Quantification of sniffing behaviors toward male or object in estrus and diestrus females. $n = 5–7$ mice/group. Two-way ANOVA, Bonferroni multiple comparisons tests.

(B) Sex preference assay. Quantification of sniffing preference index toward male or female stimuli. $n = 7–9$ mice/group. Two-way ANOVA, Bonferroni multiple comparisons tests.

(C) Opposite-sex social interaction assay. Quantification of female-initiated social interactions (bottom left) and frequency of female avoidance responses to male approaches (bottom right). $n = 7–9$ mice/group. Two-way ANOVA, Bonferroni multiple comparisons tests.

(D) Female sexual receptivity assessment. Quantification of the lordosis quotient (bottom left) and the percentage of male mating attempts rejected by females (bottom right). $n = 5–7$ mice/group. Two-way ANOVA, Bonferroni multiple comparisons tests.

(E–G) Quantification of male social behaviors. Sniffing behaviors toward female or object in the sociosexual preference assay (E), sniffing preference index in sex preference assay (F), and male-initiated interaction duration during social interaction assay (G). $n = 5–10$ mice/group. Two-way ANOVA, Bonferroni multiple comparisons tests for (E), and two-tailed unpaired t test for (F) and (G).

(H–L) Quantification of male sexual behavior. Parameters analyzed including mounting duration (H), number of mounts (I), intromission duration (J), number of intromissions (K), and percentage of ejaculation (L). $n = 5–10$ mice/group. Two-tailed unpaired t test (H and I) and Mann-Whitney test (J and K).

* $p < 0.05$, ** $p < 0.01$, *** $p < 0.001$, **** $p < 0.0001$; n.s., not significant; data represent mean \pm SEM.

See also Figure S2.

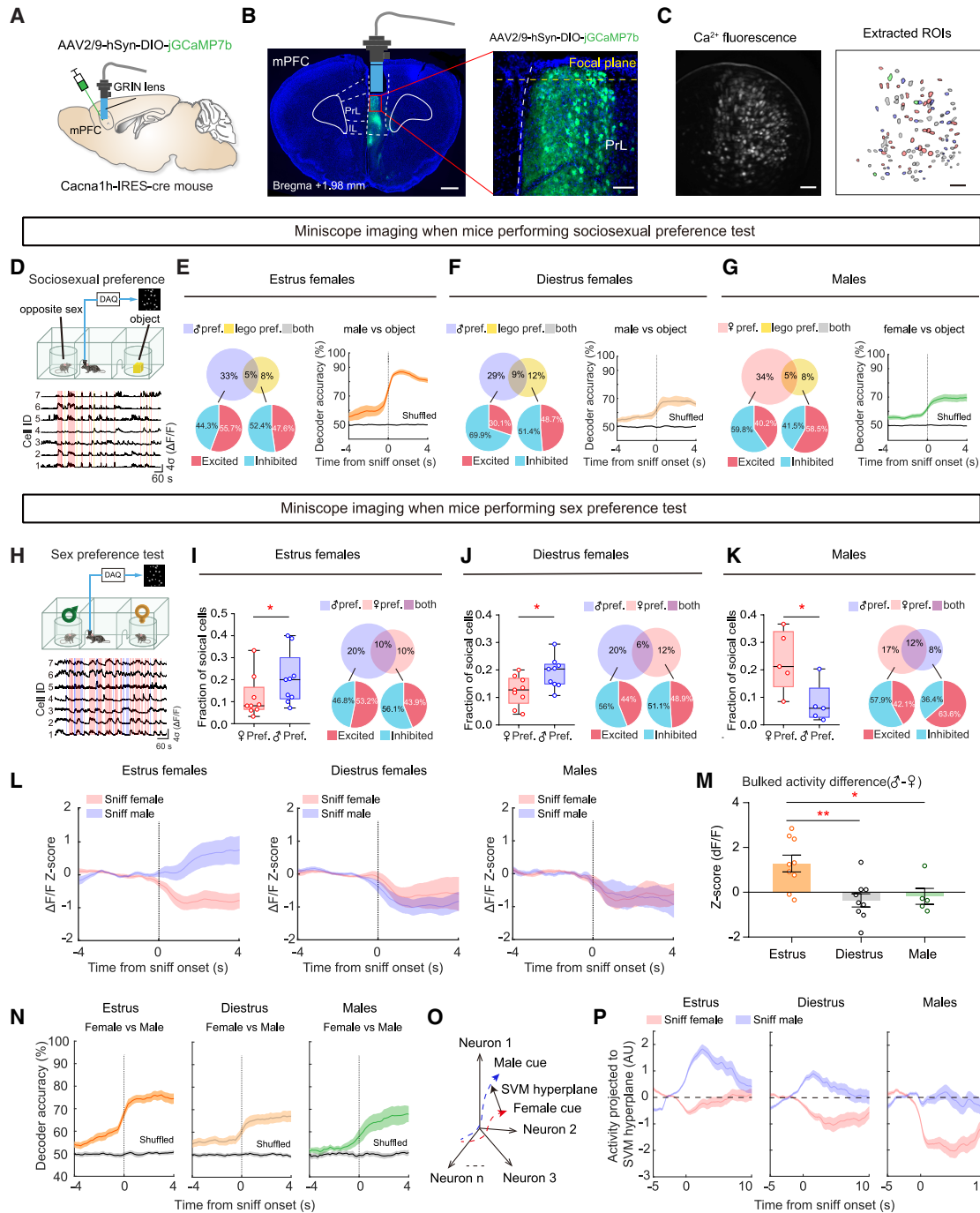


Figure 4. Estrus- and sex-specific representation of target-sex information by mPFC^{Cacna1h+} neurons

(A) AAV2/9-hSyn-DIO-jGCaMP7b injection into the mPFC of Cacna1h-IRES-Cre mice.
 (B) Expression of jGCaMP7b in the mPFC with a GRIN lens implanted above the injection site. Scale bars, 500 μ m (left) and 50 μ m (right).
 (C) Raw calcium fluorescence from a single imaging field (left). Extracted regions of interest (ROIs) corresponding to single neurons from the imaging field (right). Scale bars, 50 μ m.
 (D) Sociosexual preference test paradigm (top) and representative calcium traces from mPFC^{Cacna1h+} neurons (bottom).
 (E–G) Fraction of mPFC^{Cacna1h+} neurons responding to sniffing mouse of opposite sex vs. object in estrus females (E, left, $n = 510$ neurons from 8 mice), diestrus females (F, left, $n = 319$ neurons from 5 mice), and males (G, left, $n = 703$ neurons from 10 mice). Time-wise classifier performance for distinguishing between sniffing male and object (–4 to 4 s relative to sniff onset; E–G, right).
 (H) Sex preference test paradigm (top) and representative calcium traces from mPFC^{Cacna1h+} neurons (bottom).

(legend continued on next page)

and males than in estrus females (Figures 4E–4G). By contrast, male-responsive mPFC^{Cacna1h+} neurons were predominantly activated during estrus, indicating an estrus-specific shift in the excitation/inhibition (E/I) balance toward excitation (Figure 4E). To assess the encoding capabilities of mPFC^{Cacna1h+} neurons, we trained a linear support vector machine (SVM) classifier to distinguish opposite-sex and object trials based on population activity. Classifiers trained with estrus-state data achieved higher decoding accuracy than those trained with diestrus or male data (Figures 4E–4G and S4D). This enhanced encoding was further validated using pseudo-population analyses controlling for ensemble size effects (Figure S4E), highlighting the estrus-dependent enhancement of male cue representation by mPFC^{Cacna1h+} neurons.

To investigate the neural correlates of sex-specific social cues in mPFC^{Cacna1h+} neurons, we analyzed their calcium dynamics during male and female target investigation in sex preference tests (Figure 4H). Across all groups, a higher proportion of neurons responded to opposite-sex compared with same-sex targets (Figures 4I–4K). In estrus females, opposite-sex cues excited mPFC^{Cacna1h+} neurons, while in diestrus females and males, opposite-sex cues predominantly suppressed their activity, aligning with the observations from the sociosexual preference assay (Figures 4I–4L). Quantification of average neuronal activity confirmed selective activation in estrus females during male investigation trials (Figures 4L and 4M). By contrast, males exhibited decreased neuronal activity during female investigation trials (Figure 4L).

To investigate population-level encoding of social target sex, we trained an SVM classifier to discriminate between male and female investigation trials based on neural activity around sniff onset. Classification accuracy exceeded chance for all groups, with the highest performance achieved in estrus females (Figure 4N). Projecting neural activity onto the SVM hyperplane, which maximally separated male and female trials, revealed that the discrimination was primarily driven by opposite-sex responses in estrus females and males (Figures 4O and 4P). In males, same-sex-preferring neurons exhibited a higher area under receiver operating characteristic (auROC) bias toward opposite-sex targets compared with diestrus females (Figure S4J). Furthermore, dimensionality reduction using principal-component analysis (PCA) demonstrated a more distinct separation of opposite-sex trials from baseline compared with same-sex trials in both estrus females and males (Figures S4K and S4L). These findings highlight a significant

tuning bias of mPFC^{Cacna1h+} neurons toward opposite-sex cues in estrus females and males.

Collectively, these findings reveal that mPFC^{Cacna1h+} neurons encode social cues in an estrus- and sex-specific manner, with opposite-sex cues enhancing activity in estrus females but predominantly suppressing it in males. This differential encoding may underlie the sexually dimorphic modulation of sociosexual behaviors.

Distinct mPFC^{Cacna1h+} neuron subpopulations engage in both representing self-estrous states and distinguishing sex of sniffing targets

To determine whether mPFC^{Cacna1h+} neurons encode self-estrous states in females, we analyzed calcium imaging data across three stages: baseline in homecage, habituation in a three-chamber apparatus, and social target investigation (Figure 5A). Aligned mPFC^{Cacna1h+} neurons imaged across estrus and diestrus in the same female mouse were further analyzed (Figure 5B). These aligned-neuron analyses mirrored previous findings, showing a significant increase in activity during male sniffing in estrus females compared with their diestrus phase (Figure 5D). Additionally, an SVM classifier trained on estrus-state data achieved superior performance in predicting male- vs. female-directed sniffing behaviors (Figure 5E).

The aligned mPFC^{Cacna1h+} neurons exhibited similar spontaneous activities across estrus and diestrus in both homecage and habituation stages (Figures 5F and 5G), yet neural decoding analysis reliably distinguished between these states with notable accuracy (Figure 5H), indicating their ability to encode self-estrous states. Despite comparable mean spontaneous activity, this distinction suggests the presence of subpopulations with estrous phase-specific activity patterns.

To further characterize functional subpopulations, we applied K-means clustering (see STAR Methods) to partition aligned mPFC^{Cacna1h+} neurons across all female mice. Optimal clustering identified five distinct subpopulations ($K = 5$) (Figure S5B). A heatmap of cluster profiles revealed distinct activity patterns (Figure 5I), suggesting that each subpopulation contributes to specialized encoding functions. Cluster-based analysis of mPFC^{Cacna1h+} neuronal activity revealed significant differences in spontaneous firing between estrus and diestrus during home cage and habituation in most subpopulations (Figure 5K). Notably, clusters 2 and 3 exhibited distinct estrous-phase-dependent activity differences during male sniffing. Decoding analysis (Figures 5L and 5N) and fluorescence

(I–K) Fraction of mPFC^{Cacna1h+} neurons responding to sniffing female vs. male in individual (left) and pooled (right) estrus females (I, $n = 394$ neurons from 9 mice), diestrus females (J, $n = 384$ neurons from 9 mice), and males (K, $n = 266$ neurons from 5 mice). Mann-Whitney test (I) and two-tailed unpaired t test (J and K). (L) Averaged Z-scored calcium signal aligned to sniff onset for investigating female and male trials in estrus females ($n = 9$, left), diestrus females ($n = 9$, middle), and males ($n = 5$, right).

(M) Quantification of Z-scored calcium signal difference between sniffing male and female trials (0–4 s post-sniff onset) in estrus females, diestrus females, and males ($n = 9$ females, 5 males, one-way ANOVA, and Bonferroni's multiple comparisons test).

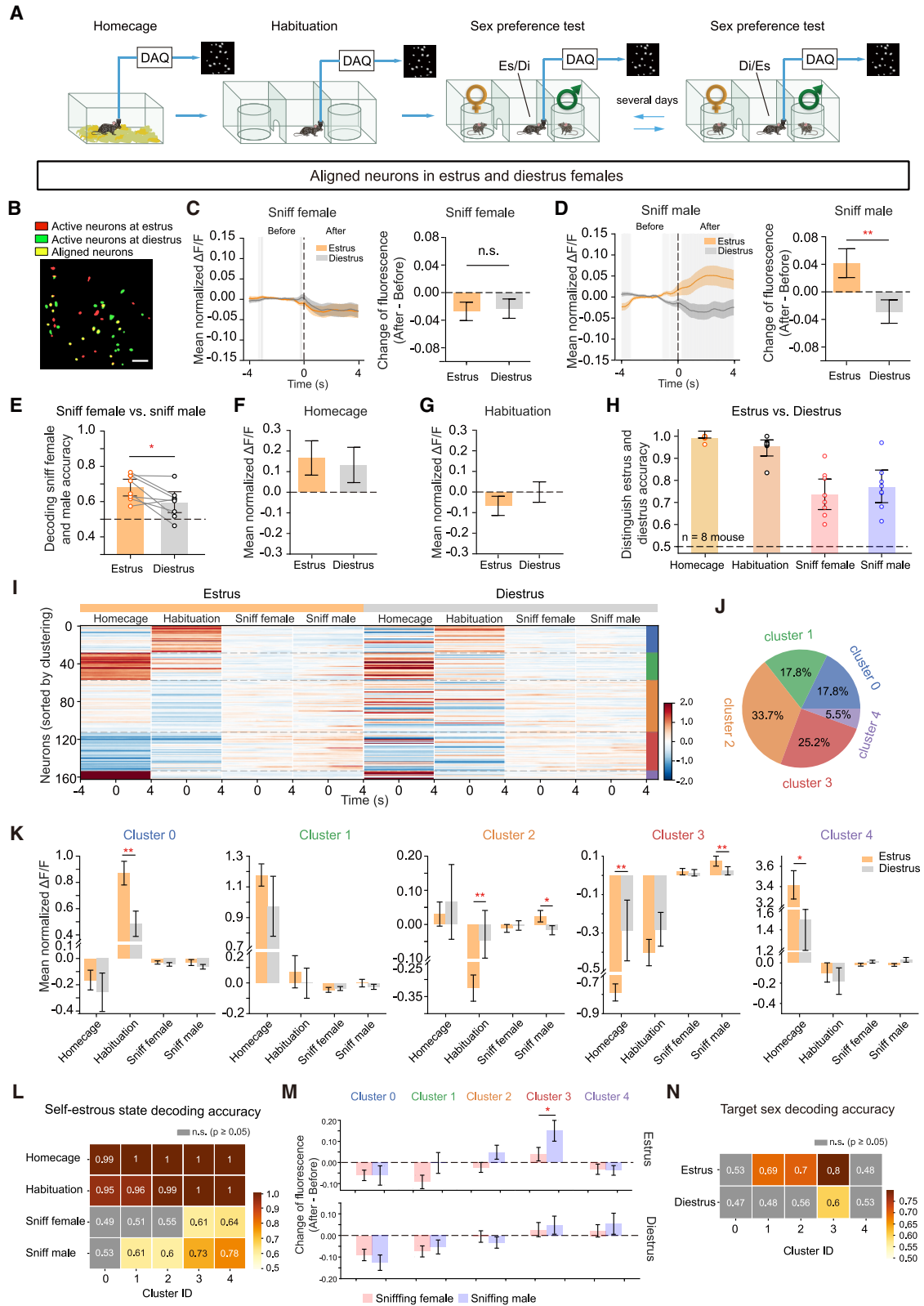
(N) Time-wise classifier performance for distinguishing between sniffing male and female (–4 to 4 s relative to sniff onset) in estrus females (left), diestrus females (middle), and males (right).

(O) Schematic of mPFC^{Cacna1h+} neural activity projection onto an SVM-optimized hyperplane during male/female investigation.

(P) mPFC^{Cacna1h+} neural activity during sniffing male (blue) and female (red) trials projected onto the SVM hyperplane in estrus females, diestrus females, and males.

* $p < 0.05$, ** $p < 0.01$; data represent mean \pm SEM.

See also Figures S3 and S4.



(legend on next page)

change ratio (Figure 5M) per cluster yielded consistent findings. Most neuronal clusters demonstrated optimal performance in decoding self-estrous states based on spontaneous activity data (Figure 5L), with cluster 3 achieving the highest accuracy in decoding social target sex during the sex preference test (Figure 5N). Clusters 4 and 0 primarily encoded self-estrous states, while clusters 1, 2, and 3 encoded both self-estrous states and target sex (Figures 5L and 5N), indicating a complex representation of mixed information. Interestingly, subpopulations in males paralleled those in females (Figures S5F–S5H), suggesting a conserved subpopulation architecture in both sexes.

Collectively, these findings demonstrate that mPFC^{Cacna1h+} neurons encode self-estrous states and distinguish the sex of sniffing targets, with distinct subpopulations representing different aspects of this multifaceted information. These results highlight the mPFC's critical role in integrating internal estrous states with external social cues.

Ovarian-hormone-induced *Cacna1h* upregulation drives estrus-specific activity changes of mPFC^{Cacna1h+} neurons

To investigate the molecular and cellular mechanisms underlying estrus-specific activity changes in mPFC^{Cacna1h+} neurons, we performed TRAP-seq (translating ribosome affinity purification followed by RNA sequencing) to identify the translational profiles of mPFC^{Cacna1h+} neurons across the estrous cycles⁴⁶ (Figures 6A and S6A). Hierarchical clustering identified five gene clusters with distinct expression patterns (Figure 6B). Cluster 3 genes, exhibiting peak expression during estrus, were significantly enriched in female-specific functions related to reproduction, synaptic plasticity, and calcium-ion-dependent exocytosis (Figures 6C and 6D). Notably, the fold enrichment of these GO terms in cluster 3 was substantially higher than in other estrous phases (Figure 6D). This suggests a female-spe-

cific function of mPFC^{Cacna1h+} neurons related to sex and the estrous cycle.

Notably, *Cacna1h*, a cluster 3 gene, may drive estrus-dependent synaptic potentiation under membrane hyperpolarization, reaching peak expression during estrus (Figure 6E), as confirmed by real-time quantitative PCR and RNAscope (Figures 6F and 6G). Moreover, *Cacna1h* mRNA levels increased dramatically in ovariectomized female mice receiving ovarian hormones to induce estrus (Figures 6H and 6I). The *Cacna1h* gene promoter region includes hormone response elements binding estrogen and progesterone receptors (ERE and PRE), with significantly stronger affinity for PR and ER α in estrus females compared with diestrus females and males (Figure 6J). These findings indicate that ovarian hormones directly regulate *Cacna1h* expression via a transcriptional pathway during estrus. This dynamic expression pattern was specific to *Cacna1h* and not observed for the other T-type calcium channel genes, *Cacna1g* and *Cacna1i* (Figures S6C and S6D).

The estrus-specific *Cacna1h* upregulation suggested enhanced Cav3.2-mediated T-type currents in mPFC^{Cacna1h+} neurons. To confirm this, we measured T-type calcium currents in mPFC^{Cacna1h+} neurons and found significantly larger amplitudes in estrus females compared with diestrus females and males (Figure 6K). This increased calcium influx enhanced mPFC^{Cacna1h+} neuron firing frequency, as evidenced by higher spike counts at each injected current step (>100 pA) during estrus. Blocking T-type currents with mibefradil reduced firing rates and eliminated the estrus-dependent excitability difference (Figure 6L), demonstrating that Cav3.2-mediated T-type currents drive estrus-specific hyperactivity in mPFC^{Cacna1h+} neurons.

The hyperpolarized RMP and hyperactivity of mPFC^{Cacna1h+} neurons during estrus suggest that T-type calcium current-induced rebound activation may contribute to this process. To investigate this, we examined rebound activity in mPFC^{Cacna1h+}

Figure 5. Distinct mPFC^{Cacna1h+} neuron subpopulations engage in both representing self-estrous states and distinguishing sex of sniffing targets

- (A) Calcium imaging of mPFC^{Cacna1h+} neurons in female mice across three distinct stages, which was performed during both the estrus and diestrus phases in the same female mouse.
- (B) Representative calcium imaging fields of view showing aligned mPFC^{Cacna1h+} neurons recorded in estrus and diestrus females. Scale bar, 50 μ m.
- (C and D) Calcium activity of aligned mPFC^{Cacna1h+} neurons during sniffing trials in estrus and diestrus. Colored shaded areas, SEM. Gray shading, time points with significant differences between estrus and diestrus ($n = 8$ mice).
- (E) Decoding accuracy of sniffing target sex using aligned mPFC^{Cacna1h+} neural activity in estrus and diestrus ($n = 8$ mice; Wilcoxon matched-pairs signed-rank test).
- (F and G) Spontaneous activity of aligned mPFC^{Cacna1h+} neurons in homecage (F) and 3-chamber habituation (G) ($n = 162$ neurons from 8 mice).
- (H) Decoding self-estrous states from mPFC^{Cacna1h+} neural activity across behavioral stages. Decoder trained on calcium activity predicted self-estrous state above chance level during all stages.
- (I) Clustering of mPFC^{Cacna1h+} neurons based on activity profiles across behavioral stages. Heatmap shows mean activity profiles of clustered neurons, with rows representing single neurons and columns representing behavioral stages. Color scale indicates normalized mean activity, colors on the right axis denote different clusters, and colors on the top distinguish estrus and diestrus.
- (J) The proportion of mPFC^{Cacna1h+} neurons assigned to each cluster. The color of each slice corresponds to the cluster colors in (I).
- (K) Mean activity of clusters in estrus and diestrus states during different behavioral stages.
- (L) Decoding accuracy of self-estrous state using clusters across behavioral contexts. Heatmap showing decoding accuracy for each cluster (columns) and behavior (rows). Colored entries, $p < 0.05$; gray entries, non-significant. Color bar indicates the accuracy range.
- (M) Fluorescence change ratio of clusters before and after the onset of sniff-female and sniff-male events in estrus (top) and diestrus (bottom) states.
- (N) Decoding accuracy of sniffing target sex using mPFC^{Cacna1h+} neuron clusters in estrus and diestrus. Matrix depicting decoding accuracy of each cluster (columns) during different estrous states (rows).

* $p < 0.05$, ** $p < 0.01$; n.s., not significant; data represent mean \pm SEM.

See also Figure S5.

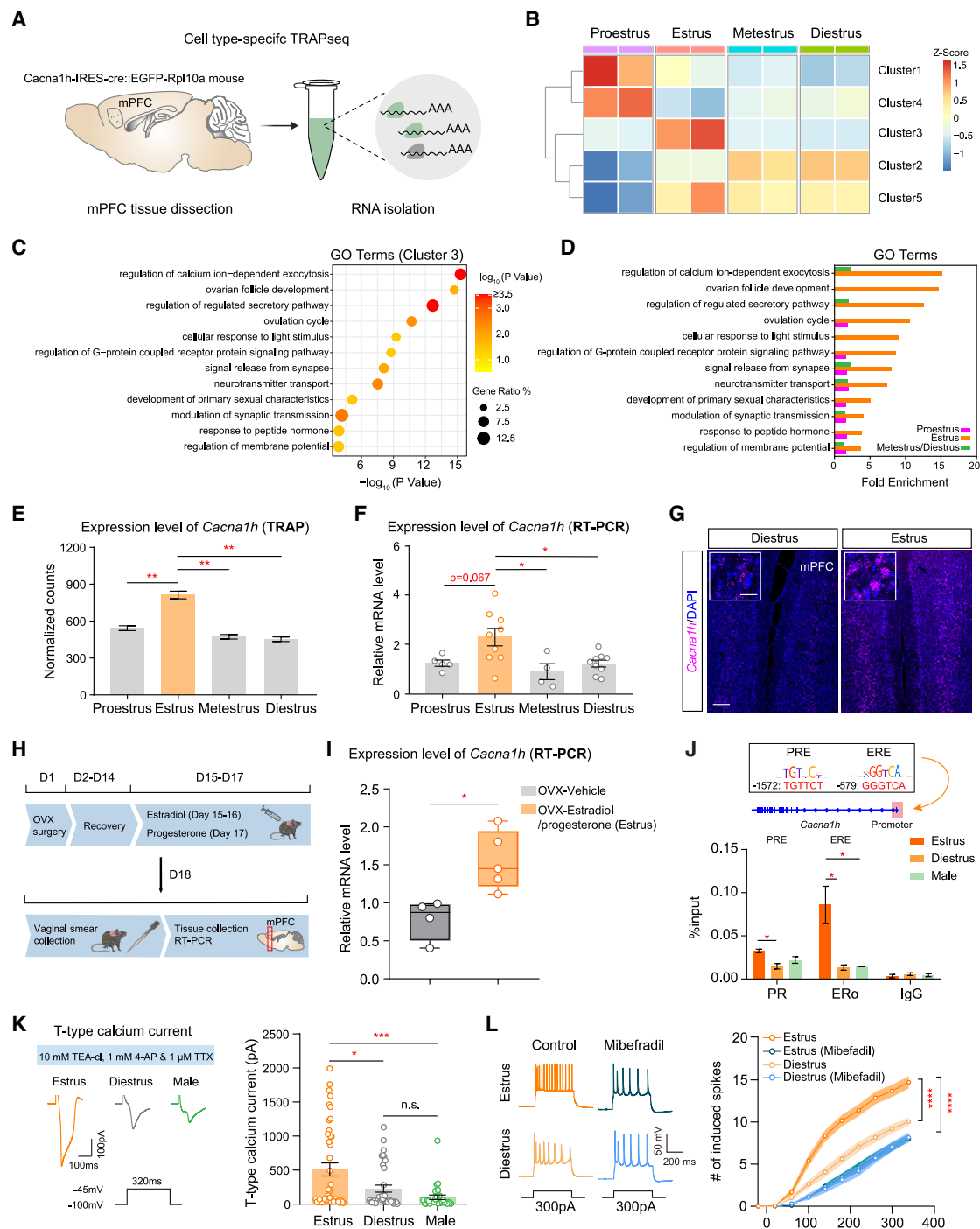


Figure 6. Ovarian-hormone-induced *Cacna1h* upregulation drives estrus-specific activity of mPFC *Cacna1h*⁺ neurons

(A) TRAP profiling of translating mRNAs in mPFC *Cacna1h*⁺ neurons.

(B) Hierarchical clustering of gene expression in mPFC *Cacna1h*⁺ neurons from females at four estrous phases. Five gene clusters are differentially expressed across the estrous cycle.

(C) GO analysis of DEGs in cluster 3 of estrus-sensitive genes.

(D) Comparative analysis of DEG enrichment in GO categories across estrous stages. Fold enrichment is shown as zero when the *p* value is not significant.

(E) TRAP counts of *Cacna1h* mRNA enrichment in mPFC *Cacna1h*⁺ neurons from females at different estrous phases (*n* = 2 samples/group, one-way ANOVA, and Bonferroni multiple comparisons tests).

(F) RT-qPCR of *Cacna1h* in the mPFC of females at four estrous stages (*n* = 4–9 mice/group).

(legend continued on next page)

neurons following inhibition by presynaptic OxtrINs *in vivo*. We optogenetically triggered oxytocin release by expressing ChrimsonR in the paraventricular nucleus (PVN) while recording calcium dynamics in mPFC^{Cacna1h+} neurons using fiber photometry⁴⁷ (Figure S6F). To isolate oxytocin's primary effect via OxtrINs, we blocked excitatory synaptic transmission and corticotropin-releasing factor (CRF) signaling to exclude confounding influences from excitatory Oxtr+ mPFC neurons and PVN-derived CRF peptides acting on CRF receptor 1-expressing mPFC neurons.³³ Optogenetic PVN stimulation evoked two distinct increases in mPFC^{Cacna1h+} activity: an immediate peak at light onset, likely reflecting disinhibition at inhibitory synapses, and a subsequent rebound activation at light offset (Figure S6G). This rebound activity was more pronounced in estrus than in diestrus (Figure S6I). Oxtr blockade reduced the rebound activity amplitude in estrus (Figure S6I), underscoring the crucial role of oxytocin/OxtrINs in mediating the enhanced rebound activation of mPFC^{Cacna1h+} neurons during estrus.

Taken together, our findings reveal that the estrus-specific elevation of *Cacna1h*, driven by ovarian hormones through a transcriptional pathway, enhances T-type currents, leading to estrus-specific electrophysiological changes in mPFC^{Cacna1h+} neurons. Furthermore, oxytocin, acting through OxtrINs, modulates the rebound activity of mPFC^{Cacna1h+} neurons in an estrus-dependent manner.

***Cacna1h* in the mPFC mediates estrus-specific and sexually opposing regulation of sociosexual behaviors**

To investigate the role of *Cacna1h* in sociosexual behaviors, we generated a conditional knockout (cKO) mouse line for the *Cacna1h* gene (*Cacna1h^{fl/fl}*) (Figures S7A and S7B). Expressing Cre virus in the mPFC of this mouse line significantly reduced *Cacna1h* expression (Figures S7C–S7E) and decreased T-type calcium current amplitudes to 16.7% of control levels (Figure S7F), confirming efficient *Cacna1h* deletion at both genetic and electrophysiological levels.

In females, mPFC-specific *Cacna1h* cKO significantly reduced male-directed sniffing (Figure 7A) and decreased male preference exclusively during estrus, without affecting other estrous stages (Figures 7C and S7I). Testing each female mouse across different estrous cycles revealed a consistent, estrus-phase-specific reduction in male-directed sniffing behavior (Figure 7B). During free social interactions, estrus-phase *Cacna1h* cKO females exhibited reduced male investigation and increased avoidance of male approaches (Figure 7D). Moreover, *Cacna1h* deletion in the

mPFC significantly reduced sexual receptivity in estrus females, as indicated by a decreased lordosis quotient (Figure 7E). Notably, conditional knockout of *Cacna1h* in the female mPFC did not alter estrous cycle length or phase duration (Figure 7F), suggesting that *Cacna1h* directly modulates sociosexual behaviors during estrus rather than affecting cycle progression.

By contrast, *Cacna1h* deletion in the male mPFC enhanced sociosexual interest, evidenced by increased female-directed sniffing duration (Figures 7G and 7I) and elevated preference for female counterparts (Figure 7H). Furthermore, *Cacna1h* deletion led to heightened sexual behaviors, including increased mounting and intromission toward females (Figures 7K–7N). Notably, mPFC *Cacna1h* deletion did not affect the time spent in same-sex social interaction or object investigation in either sex (Figure S7J). Moreover, it had no impact on locomotor activity, as assessed by total distance moved in the open field test, or baseline anxiety, as measured by open arm entries and duration in the elevated plus maze test and center duration in the open field test in both sexes (Table S1). These results suggest that *Cacna1h* specifically regulates opposite-sex sociosexual behaviors without influencing general sociability, locomotion, or baseline anxiety.

Taken together, these findings demonstrate that dynamic *Cacna1h* expression in the mPFC provides the molecular basis for the estrus-dependent and sex-specific regulation of sociosexual interests and sexual behaviors by mPFC^{Cacna1h+} neurons.

mPFC^{Cacna1h+} neurons exert sexually dimorphic top-down control of sociosexual behavior via AHNc-descending pathways

The AHN is a key sexually dimorphic region across several species.^{35–37,48–51} Our previous findings revealed that the estrous cycle modulates AHNc neuronal responses to sociosexual behavior and synaptic plasticity of AHNc-projecting mPFC neurons (Figures 1G–1K). Furthermore, *Cacna1h* is highly enriched in mPFC neurons projecting to the AHNc (Figure 1M). Based on these observations, we hypothesized that AHNc-descending pathways mediate the sex-specific function of mPFC^{Cacna1h+} neurons in regulating sociosexual behavior. To test this, we employed a circuit-specific chemogenetic approach to selectively inhibit hM4Di-expressing axonal terminals of mPFC^{Cacna1h+} neurons in the AHNc region via cannula-guided clozapine N-oxide (CNO) infusion (Figures S7K–S7M). Silencing these projections reduced social sniffing toward males in estrus females but not in diestrus females (Figure S7P). Intriguingly, inhibiting the same mPFC^{Cacna1h+} neurons-AHN pathway produced the

(G) *Cacna1h* levels in the mPFC of estrus and diestrus females using RNAscope. Scale bars, 50 μ m [inset] and 200 μ m.

(H) Experimental timeline of ovariectomy (OVX) and ovarian hormone supplementation.

(I) RT-qPCR of *Cacna1h* in the mPFC of OVX females receiving ovarian hormones or vehicle ($n = 4–6$ mice/group; two-tailed unpaired *t* test).

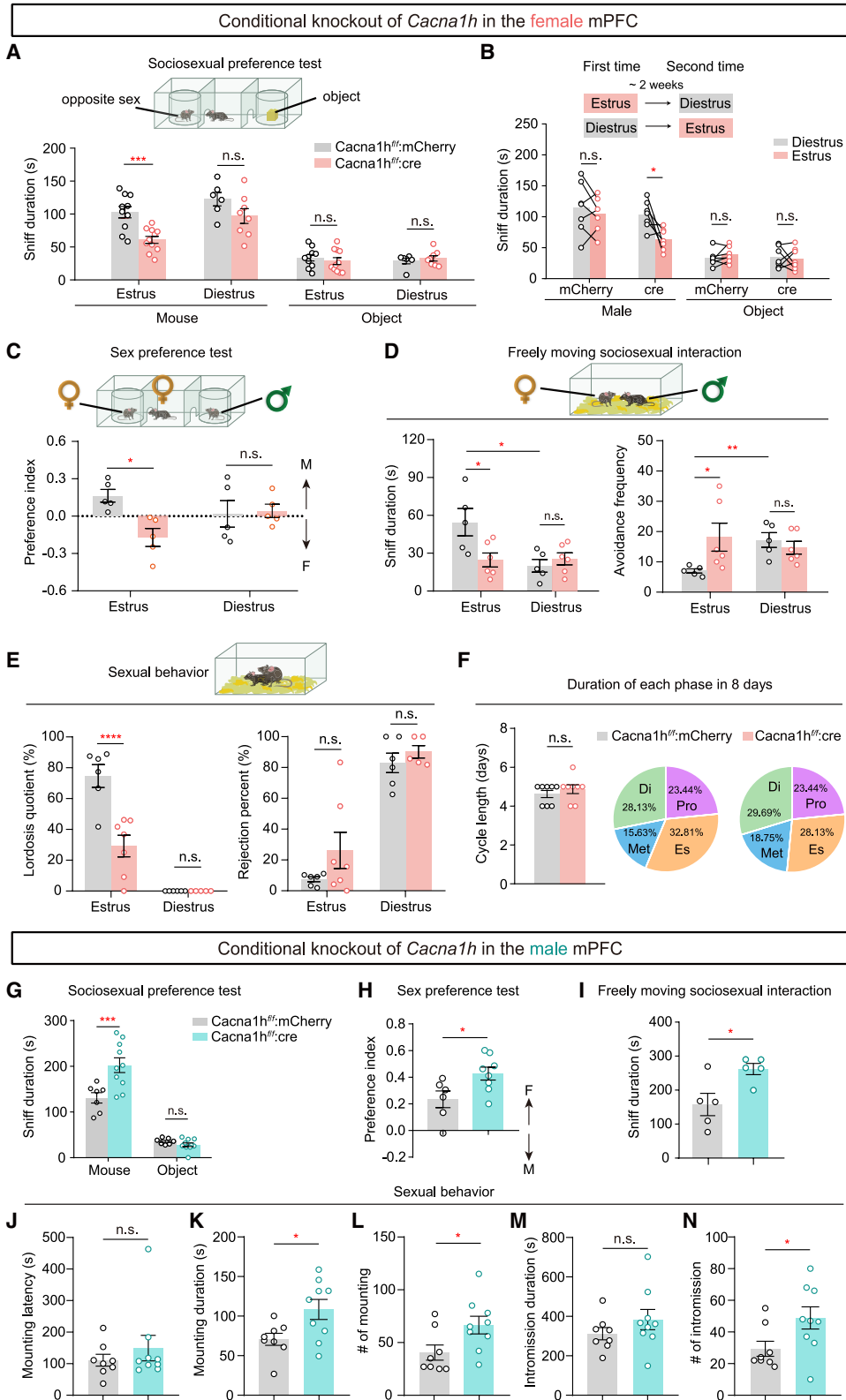
(J) Chromatin immunoprecipitation (ChIP) analysis of estrogen receptor α (ER α) and progesterone receptor (PR) binding to the *Cacna1h* promoter across the estrous cycle. Predicted estrogen response element (ERE) and progesterone response element (PRE) sites are shown (top). ER α and PR binding to the *Cacna1h* gene in estrus and diestrus is quantified as percentage of input DNA recovered (bottom).

(K) T-type calcium current recording strategy (top). Representative traces of T-type calcium currents at -45 mV in mPFC^{Cacna1h+} neurons from estrus and diestrus females and males (bottom left). Quantitation of T-type current amplitudes ($n = 29–42$ cells/group, one-way ANOVA, and Bonferroni multiple comparisons tests) (right).

(L) Induced spikes from mPFC^{Cacna1h+} neurons with and without mibefradil in estrus and diestrus females ($n = 22–33$ cells/group, two-way ANOVA, and Bonferroni multiple comparisons tests, right).

* $p < 0.05$, ** $p < 0.01$, *** $p < 0.001$, **** $p < 0.0001$; n.s., not significant; data represent mean \pm SEM.

See also Figure S6.



(legend on next page)

opposite effect in males, promoting their investigation of female conspecifics (Figure S7Q). Together, these findings demonstrate that mPFC^{Cacna1h+} neurons mediate estrous-dependent and sexually dimorphic regulation of sociosexual behavior through descending projections to the AHN.

DISCUSSION

We identified a population of *Cacna1h*-defined L5_PT neurons as primary estrous-sensitive neurons in the mPFC. These neurons form a circuit with OxtRNs and the AHN, promoting estrus-specific sociosexual and mating behaviors in females while suppressing these behaviors in males. mPFC^{Cacna1h+} neurons encode opposite-sex investigation, exhibiting enhanced activity in estrus females but suppression in males. They show a biased representation of opposite-sex cues in estrus females and males and mix-represented self-estrous state with target-sex information in females. Mechanistically, ovarian hormones upregulate *Cacna1h*-encoded T-type calcium channels in mPFC^{Cacna1h+} neurons during estrus, enhancing rebound excitation following inhibition from presynaptic OxtRNs. This modulation drives estrus-specific activity changes and mediates the sexually dimorphic effects of mPFC^{Cacna1h+} neurons on sociosexual behaviors. Our study provides direct evidence of how the mPFC integrates internal physiological states with external social cues to orchestrate adaptive innate social behaviors, unveiling a top-down mechanism underlying estrus-dependent and sexually dimorphic sociosexual behaviors (Figure S7R).

Estrus-sensitive mPFC neurons integrate internal states and external social cues to guide adaptive sociosexual behaviors

The mPFC is well-positioned to potentially integrate social cues and physiological states to guide adaptive social preferences, given its established roles in executive function,^{52,53} information integration,¹⁴ behavioral flexibility,^{15,54,55} and social behavior regulation.^{16–18} Despite the mPFC's involvement in estrus-dependent male investigation,³ the cortical mechanisms governing its dynamic control over the reproductive cycle remain largely

unexplored. Notably, non-specific excitatory mPFC neurons in females show similar proportions of male- and female-preferring cells,¹⁸ suggesting the need to identify cortical cell types that biased encoding of male cues across the estrous cycle.

Our study identifies a distinct population of estrus-sensitive mPFC^{Cacna1h+} neurons that exhibit sexually dimorphic encoding of opposite-sex cues and regulate estrus-specific sociosexual behaviors. We demonstrate that these neurons shift toward excitation in responses to male targets and show improved decoding accuracy for conspecific sex during estrus phase (Figures 4 and 5). This enhanced social cue representation may serve as a neural mechanism for prioritizing sociosexual interactions with potential mates when females are most receptive, optimizing reproductive success.

We also reveal that mPFC^{Cacna1h+} neurons encode internal estrous states in females, with mixed representation of social and physiological information, providing direct evidence to support the hypothesis that mPFC integrates internal states and external social cues to guide appropriate social decisions.²¹ Further, we demonstrate that mPFC^{Cacna1h+} neurons exert sexually dimorphic top-down control of sociosexual preference via AHN-descending pathways (Figures S7K–S7Q). The AHN has strong bidirectional connectivity with estrogen receptor type 1-expressing neurons in the ventrolateral subdivision of the ventromedial hypothalamus (VMHv),⁵⁶ which play a critical role in promoting female sexual behaviors during estrus.^{4,57,58} These connections may facilitate the top-down regulation of the transition from sociosexual interaction to sexual receptivity in females during ovulation. Our findings establish the mPFC as a hub for integrating diverse streams of information to flexibly guide context-specific, sexually dimorphic sociosexual interactions, advancing our understanding of the neural basis of innate social behaviors.

Cellular and molecular mechanisms driving the dynamic encoding of estrous states and target sex in mPFC^{Cacna1h+} neurons

In the mPFC, ovarian hormone receptor expression levels do not correlate with changes in sex-hormone-regulated IEG networks

Figure 7. *Cacna1h* in the mPFC regulates sociosexual behaviors in estrus-specific and sexually dimorphic manners

(A) mPFC *Cacna1h* deletion in female mice decreased their sniffing time toward males during estrus but not diestrus ($n = 6–11$ mice/group; two-way ANOVA, Bonferroni multiple comparisons tests).

(B) Each female mouse was examined twice for sociosexual preference during both estrus and diestrus phases, with a minimum 2-week interval ($n = 7$ mice/group; two-tailed paired t test).

(C) mPFC *Cacna1h* ablation in estrus females significantly reduced sex preference toward males ($n = 5$ mice/group; two-way ANOVA, Bonferroni multiple comparisons tests).

(D) Conditional knockout of *Cacna1h* in estrus females significantly reduced freely moving social interaction and increased avoidance frequency toward males ($n = 5–6$ mice/group; two-way ANOVA, Bonferroni multiple comparisons tests).

(E) Ablation of *Cacna1h* in estrus females significantly reduced lordosis quotient in response to male mounts ($n = 5–7$ mice/group; two-way ANOVA, Bonferroni multiple comparisons tests).

(F) Estrous cycle length did not significantly differ between *Cacna1h*^{fl/fl}::Cre and *Cacna1h*^{fl/fl}::mCherry females ($n = 8$ mice/group; Mann-Whitney test).

(G) mPFC *Cacna1h* deletion in male mice increased sniffing time toward females ($n = 7–10$ mice/group; two-way ANOVA, Bonferroni multiple comparisons tests).

(H and I) mPFC *Cacna1h* ablation in males significantly increased preference for females in the sex preference test (H) and social interaction with females during freely moving encounters (I) ($n = 5–8$ mice/group; two-tailed unpaired t test).

(J–N) Conditional knockout of *Cacna1h* in males increased mounting and intromission behaviors toward females ($n = 8–9$ mice/group; Mann-Whitney test for J, L, and N; two-tailed unpaired t test for K and M).

* $p < 0.05$, ** $p < 0.01$, *** $p < 0.001$, **** $p < 0.0001$; n.s., not significant; data represent mean \pm SEM.

See also Figure S7.

across mPFC subpopulations (Figures 1D and 1E), prompting the question of how mPFC tracks internal hormonal states. scRNA-seq identified mPFC^{Cacna1h+} neurons as the most sensitive to ovarian hormone changes among mPFC neural types (Figure 1E). Our results further indicate that Cav3.2 T-type calcium channels, encoded by *Cacna1h*, are the primary driving force in generating estrus-specific activity patterns in mPFC^{Cacna1h+} neurons, thus linking internal physiological state switches to adaptive sociosexual behaviors.

We showed that OxtRINs monosynaptically connect with AHN-projecting neurons enriched with *Cacna1h* (Figures 1J and 1M). During estrus, ovarian hormones upregulate *Cacna1h* via the transcriptional pathway, increasing the expression of Cav3.2 T-type channels in mPFC^{Cacna1h+} neurons (Figures 6I and 6J). Social sniffing⁵⁹ or PVN stimulation triggers oxytocin release in the mPFC, activating OxtRINs and hyperpolarizing their postsynaptic mPFC^{Cacna1h+} neurons (Figures 1J and 1L). This hyperpolarization allows more Cav3.2 channels to recover from voltage-dependent inactivation, resulting in heightened rebound activation of mPFC^{Cacna1h+} neurons specifically during estrus (Figures 6K, 6L, and S6I). Consequently, when estrus females investigate males, the activity of mPFC^{Cacna1h+} neurons shifts from inhibition to excitation, updating the representation of male cues in the mPFC (Figure 4). Furthermore, the varied T-type currents observed in layer 5 mPFC pyramidal neurons may account for the heterogeneous activity patterns of mPFC^{Cacna1h+} subpopulations between estrus and diestrus (Figure 5K). Ultimately, the upregulation of Cav3.2 channels by ovarian hormones, combined with the actions of oxytocin on OxtRINs, is the critical mechanism driving estrus-specific activity patterns in mPFC^{Cacna1h+} neurons.

Despite the impact of sex hormones on a variety of genes, Cav3.2 channels act at an early stage to regulate membrane hyperpolarization during social approach due to their low-voltage activated properties.^{41,60} Cav3.2 activation initiates a cascade of events: depolarization of the membrane potential, opening of high-voltage gated channels, and changes in neuronal excitability and synaptic efficacy. The Cav3.2-mediated mechanism precisely modulates mPFC^{Cacna1h+} neural activity based on hormonal fluctuations, enabling adaptive female preference toward males tailored to the specific demands of the estrous cycle. Further investigation into T-type calcium channels in females may uncover additional estrus-dependent and sex-specific behavioral adaptations to internal states.

Sexually dimorphic top-down roles of the mPFC in sexual behavior

Sexual behavior exhibits notable sexual dimorphism in both normal sexual behaviors and disorders.^{61–63} Hyposexuality affects women approximately twice the rate of men,^{64–66} while hypersexuality is more than two times prevalent in men.^{67–69} Despite these observed differences, the neural mechanisms underlying this sexual dimorphism remain unexplored.

In males, enhanced PFC activity correlates with sexual inhibition,^{67,70} while PFC dysfunction is linked to hypersexual behaviors.^{71,72} Conversely, during ovulation, characterized by peak estrogen levels, women display increased mPFC activity

in response to erotic stimulation compared with other cycle phases.^{73,74}

Our findings reveal a previously unrecognized sexually dimorphic function of mPFC^{Cacna1h+} neurons in modulating sexual behaviors. These neurons exhibit robust sex differences in gene expression (Figure S1F), neural activity in response to opposite-sex social stimuli (Figures 4D–4M), and distinct representation of target sex information (Figures 4H–4P). Chemogenetic manipulation and *Cacna1h* deletion demonstrate the necessity of these neurons in promoting female sexual behavior while suppressing male sexual activity (Figures 2, 3, and 7). Our study provides a framework for understanding the top-down regulation of adaptive reproductive behaviors. Importantly, dysregulation of mPFC^{Cacna1h+} neurons and the *Cacna1h* gene may contribute to hypersexuality in males and hyposexuality in females, identifying T-type calcium channels as potential therapeutic targets for sex-specific treatments of sexual dysfunction.

Limitations of the study

While our study demonstrates that mPFC^{Cacna1h+} neurons cyclically encode target-sex and self-estrous states to regulate sociosexual behaviors, GCaMP photobleaching limits long-term recordings across a full estrous cycle. Future studies using chronic *in vivo* electrophysiology with optotagged mPFC^{Cacna1h+} neurons could reveal how their activity tracks hormonal cycles in naturalistic settings. The coordination between the mPFC and subcortical regions like the VMHv, which are critical for female sexual behaviors, remains unclear. Future studies using large-scale electrophysiological recordings could elucidate the sensory inputs to the mPFC and the multi-level regulatory mechanisms across circuits mediating sociosexual interactions and sexual behaviors. Finally, while our findings suggest sexually dimorphic roles for mPFC^{Cacna1h+} neurons and *Cacna1h* gene in sexual behaviors, their relevance to humans remains unknown. Investigating prefrontal *Cacna1h* expression or mutations in individuals with sexual dysfunction could provide valuable translational insights into sexually dimorphic behavioral disorders.

RESOURCE AVAILABILITY

Lead contact

Further information and requests for reagents should be directed to and will be fulfilled by the lead contact, Kun Li (kli@mail.tsinghua.edu.cn).

Materials availability

All materials/mouse lines generated in this study are available from the lead contact with a completed materials transfer agreement.

Data and code availability

- The scRNA-seq and TRAP-seq data have been uploaded at Gene Expression Omnibus (GEO: GSE227852 and GSE283376, respectively). All data reported in this paper will be shared by the lead contact upon request.
- All custom code used in this study has been deposited at Zenodo: <https://doi.org/10.5281/zenodo.15203046>.
- Any additional information required to reanalyze the data reported in this paper is available from the lead contact upon request.

ACKNOWLEDGMENTS

We thank Cuidong Wang at Rockefeller University for technical assistance with TRAP experiments and Dr. Diane Lipscombe at Brown University for kindly providing the *Cacna1h*-IRES-Cre knockin mouse line. Some schematic diagrams were created in [Biorender.com](https://biorender.com). This work was supported by STI2030-Major Projects (2021ZD0203000 and 2021ZD0203002), the National Science Foundation of China (32171016), the Tsinghua University Dushi Program, and a Leon Levy Neuroscience Fellowship (to K.L.).

AUTHOR CONTRIBUTIONS

Y.W., X.S., F.Z., K.L., and X.C. conducted behavioral manipulations, electrophysiology, fiber photometry, and data analysis. K.L. performed TRAP-seq, with X.S. analyzing the data. X.S. and F.Z. conducted scRNA-seq, while X.S. analyzed the data. F.Z. performed RT-qPCR and ChIP experiments. L.W. and Y.W. conducted Miniscope imaging, with Y.Z., J.M., G. Q., B.M., and X.J. analyzing the data. G.Q., N.Y., and P.R. assisted with fiber photometry experiments. Y.W. and X.S. prepared the figures. K.L., Y. W., and X.S. wrote the manuscript with input from co-authors. I.I.-T., N. H., and K.L. supervised the study. K.L. conceived and designed the project.

DECLARATION OF INTERESTS

The authors declare no competing interests.

DECLARATION OF GENERATIVE AI AND AI-ASSISTED TECHNOLOGIES IN THE WRITING PROCESS

During the preparation of this work, the authors used ChatGPT and DeepSeek for grammar and spelling checks. After using this tool, the authors reviewed and edited the content as needed and take full responsibility for the content of the published article. No generative AI tools were used to produce any original ideas or content.

STAR★METHODS

Detailed methods are provided in the online version of this paper and include the following:

- [KEY RESOURCES TABLE](#)
- [EXPERIMENTAL MODEL AND STUDY PARTICIPANT DETAILS](#)
- [METHOD DETAILS](#)
 - Identification of the female estrous cycle
 - Behavioral testing
 - Stereotaxic surgeries
 - Brain slice electrophysiological recordings
 - RNA sequencing
 - Transcription factor (TF) motif analysis
 - Chromatin immunoprecipitation (ChIP) assays
 - Calcium imaging
 - RNAscope
 - c-Fos immunohistochemistry staining
 - Ovariectomy surgery and hormonal priming
 - Real-time quantitative PCR
- [QUANTIFICATION AND STATISTICAL ANALYSIS](#)

SUPPLEMENTAL INFORMATION

Supplemental information can be found online at <https://doi.org/10.1016/j.cell.2025.04.035>.

Received: March 10, 2023
Revised: December 2, 2024
Accepted: April 25, 2025
Published: May 20, 2025

REFERENCES

1. Butcher, R.L., Collins, W.E., and Fugo, N.W. (1974). Plasma concentration of LH, FSH, prolactin, progesterone and estradiol-17 β throughout the 4-day estrous cycle of the rat. *Endocrinology* *94*, 1704–1708. <https://doi.org/10.1210/endo-94-6-1704>.
2. DeLeon, D.D., Zelinski-Wooten, M.B., and Barkley, M.S. (1990). Hormonal basis of variation in oestrous cyclicity in selected strains of mice. *J. Reprod. Fertil.* *89*, 117–126. <https://doi.org/10.1530/jrf.0.0890117>.
3. Nakajima, M., Görlich, A., and Heintz, N.J.C. (2014). Oxytocin modulates female sociosexual behavior through a specific class of prefrontal cortical interneurons. *Cell* *159*, 295–305. <https://doi.org/10.1016/j.cell.2014.09.020>.
4. Inoue, S., Yang, R., Tantry, A., Davis, C.-h., Yang, T., Knoedler, J.R., Wei, Y., Adams, E.L., Thombare, S., and Golf, S.R. (2019). Periodic remodeling in a neural circuit governs timing of female sexual behavior. *Cell* *179*, 1393–1408.e16. <https://doi.org/10.1016/j.cell.2019.10.025>.
5. Jaric, I., Rocks, D., Cham, H., Herchek, A., and Kundakovic, M. (2019). Sex and estrous cycle effects on anxiety- and depression-related phenotypes in a two-hit developmental stress model. *Front. Mol. Neurosci.* *12*, 74. <https://doi.org/10.3389/fnmol.2019.00074>.
6. Steiner, M., Dunn, E., and Born, L. (2003). Hormones and mood: from menarche to menopause and beyond. *J. Affect. Disord.* *74*, 67–83. [https://doi.org/10.1016/s0165-0327\(02\)00432-9](https://doi.org/10.1016/s0165-0327(02)00432-9).
7. Altemus, M., Sarvaiya, N., and Neill Epperson, C. (2014). Sex differences in anxiety and depression clinical perspectives. *Front. Neuroendocrinol.* *35*, 320–330. <https://doi.org/10.1016/j.yfrne.2014.05.004>.
8. Li, S.H., and Graham, B.M. (2017). Why are women so vulnerable to anxiety, trauma-related and stress-related disorders? The potential role of sex hormones. *Lancet Psychiatry* *4*, 73–82. [https://doi.org/10.1016/S2215-0366\(16\)30358-3](https://doi.org/10.1016/S2215-0366(16)30358-3).
9. Wang, G.H. (1923). *The relation between 'spontaneous' activity and oestrous cycle in the white rat. In Comparative Psychology Monographs, 2 (University of California), p. 27.*
10. Dey, S., Chamero, P., Pru, J.K., Chien, M.S., Ibarra-Soria, X., Spencer, K.R., Logan, D.W., Matsunami, H., Peluso, J.J., and Stowers, L. (2015). Cyclic Regulation of Sensory Perception by a Female Hormone Alters Behavior. *Cell* *161*, 1334–1344. <https://doi.org/10.1016/j.cell.2015.04.052>.
11. Beach, F.A. (1976). Sexual attractivity, proceptivity, and receptivity in female mammals. *Horm. Behav.* *7*, 105–138. [https://doi.org/10.1016/0018-506x\(76\)90008-8](https://doi.org/10.1016/0018-506x(76)90008-8).
12. McHenry, J.A., Otis, J.M., Rossi, M.A., Robinson, J.E., Kosyk, O., Miller, N. W., McElligott, Z.A., Budygin, E.A., Rubinow, D.R., and Stuber, G.D. (2017). Hormonal gain control of a medial preoptic area social reward circuit. *Nat. Neurosci.* *20*, 449–458. <https://doi.org/10.1038/nn.4487>.
13. Ring, J.R. (1944). The estrogen-progesterone induction of sexual receptivity in the spayed female mouse. *Endocrinology* *34*, 269–275. <https://doi.org/10.1210/endo-34-4-269>.
14. Euston, D.R., Gruber, A.J., and McNaughton, B.L. (2012). The role of medial prefrontal cortex in memory and decision making. *Neuron* *76*, 1057–1070. <https://doi.org/10.1016/j.neuron.2012.12.002>.
15. Barbas, H., and Zikopoulos, B. (2007). The prefrontal cortex and flexible behavior. *Neuroscientist* *13*, 532–545. <https://doi.org/10.1177/1073858407301369>.
16. Scheggia, D., Managò, F., Maltese, F., Bruni, S., Nigro, M., Dautan, D., Latruske, P., Contarini, G., Gomez-Gonzalo, M., Reque, L.M., et al. (2020). Somatostatin interneurons in the prefrontal cortex control affective state discrimination in mice. *Nat. Neurosci.* *23*, 47–60. <https://doi.org/10.1038/s41593-019-0551-8>.
17. Bicks, L.K., Koike, H., Akbarian, S., and Morishita, H. (2015). Prefrontal Cortex and Social Cognition in Mouse and Man. *Front. Psychol.* *6*, 1805. <https://doi.org/10.3389/fpsyg.2015.01805>.

18. Kingsbury, L., Huang, S., Raam, T., Ye, L.S., Wei, D., Hu, R.K., Ye, L., and Hong, W. (2020). Cortical Representations of Conspecific Sex Shape Social Behavior. *Neuron* 107, 941–953.e7. <https://doi.org/10.1016/j.neuron.2020.06.020>.
19. Padilla-Coreano, N., Batra, K., Patarino, M., Chen, Z., Rock, R.R., Zhang, R., Hausmann, S.B., Weddington, J.C., Patel, R., Zhang, Y.E., et al. (2022). Cortical ensembles orchestrate social competition through hypothalamic outputs. *Nature* 603, 667–671. <https://doi.org/10.1038/s41586-022-04507-5>.
20. Bhattarai, J.P., Etyemez, S., Jaaro-Peled, H., Janke, E., Leon Tolosa, U.D., Kamiya, A., Gottfried, J.A., Sawa, A., and Ma, M. (2022). Olfactory modulation of the medial prefrontal cortex circuitry: Implications for social cognition. *Semin. Cell Dev. Biol.* 129, 31–39. <https://doi.org/10.1016/j.semcdb.2021.03.022>.
21. Yizhar, O., and Levy, D.R. (2021). The social dilemma: prefrontal control of mammalian sociability. *Curr. Opin. Neurobiol.* 68, 67–75. <https://doi.org/10.1016/j.conb.2021.01.007>.
22. Pletzer, B., Harris, T.-A., Scheuringer, A., and Hidalgo-Lopez, E. (2019). The cycling brain: menstrual cycle related fluctuations in hippocampal and fronto-striatal activation and connectivity during cognitive tasks. *Neuropsychopharmacology* 44, 1867–1875. <https://doi.org/10.1038/s41386-019-0435-3>.
23. Zeidan, M.A., Igoe, S.A., Linnman, C., Vitalo, A., Levine, J.B., Klibanski, A., Goldstein, J.M., and Milad, M.R. (2011). Estradiol modulates medial prefrontal cortex and amygdala activity during fear extinction in women and female rats. *Biol. Psychiatry* 70, 920–927. <https://doi.org/10.1016/j.biopsych.2011.05.016>.
24. Chen, W., Shields, J., Huang, W., and King, J.A. (2009). Female fear: influence of estrus cycle on behavioral response and neuronal activation. *Behav. Brain Res.* 201, 8–13. <https://doi.org/10.1016/j.bbr.2009.01.019>.
25. Luine, V., Serrano, P., and Frankfurt, M. (2018). Rapid effects on memory consolidation and spine morphology by estradiol in female and male rodents. *Horm. Behav.* 104, 111–118. <https://doi.org/10.1016/j.yhbeh.2018.04.007>.
26. Shansky, R.M., Hamo, C., Hof, P.R., Lou, W., McEwen, B.S., and Morrison, J.H. (2010). Estrogen promotes stress sensitivity in a prefrontal cortex–amygdala pathway. *Cereb. Cortex* 20, 2560–2567. <https://doi.org/10.1093/cercor/bhq003>.
27. Figueiredo, H.F., Dolgas, C.M., and Herman, J.P. (2002). Stress activation of cortex and hippocampus is modulated by sex and stage of estrus. *Endocrinology* 143, 2534–2540. <https://doi.org/10.1210/endo.143.7.8888>.
28. Lui, J.H., Nguyen, N.D., Grutzner, S.M., Darmanis, S., Peixoto, D., Wagner, M.J., Allen, W.E., Kebschull, J.M., Richman, E.B., Ren, J., et al. (2021). Differential encoding in prefrontal cortex projection neuron classes across cognitive tasks. *Cell* 184, 489–506.e26. <https://doi.org/10.1016/j.cell.2020.11.046>.
29. Gao, L., Liu, S., Gou, L., Hu, Y., Liu, Y., Deng, L., Ma, D., Wang, H., Yang, Q., Chen, Z., et al. (2022). Single-neuron projectome of mouse prefrontal cortex. *Nat. Neurosci.* 25, 515–529. <https://doi.org/10.1038/s41593-022-01041-5>.
30. Auger, A.P., and Blaustein, J.D. (1997). Progesterone treatment increases Fos-immunoreactivity within some progestin receptor-containing neurons in localized regions of female rat forebrain. *Brain Res.* 746, 164–170. [https://doi.org/10.1016/s0006-8993\(96\)01190-0](https://doi.org/10.1016/s0006-8993(96)01190-0).
31. Mieczkowski, K., Kitowska, K., Braun, M., Galikowska-Bogut, B., Gorska-Arcisz, M., Piasecka, D., Stawiska, K., Zaczek, A.J., Nejc, D., Kordek, R., et al. (2022). FGF7/FGFR2–JunB signalling counteracts the effect of progesterone in luminal breast cancer. *Mol. Oncol.* 16, 2823–2842. <https://doi.org/10.1002/1878-0261.13274>.
32. Zhang, Y.L., Wen, X.D., Guo, X., Huang, S.Q., Wang, T.T., Zhou, P.T., Li, W., Zhou, L.F., and Hu, Y.H. (2021). Progesterone suppresses the progression of colonic carcinoma by increasing the activity of the GADD45 α /JNK/c-Jun signalling pathway. *Oncol. Rep.* 45, 95. <https://doi.org/10.3892/or.2021.8046>.
33. Li, K., Nakajima, M., Ibañez-Tallon, I., and Heintz, N. (2016). A cortical circuit for sexually dimorphic oxytocin-dependent anxiety behaviors. *Cell* 167, 60–72.e11. <https://doi.org/10.1016/j.cell.2016.08.067>.
34. Lo, L., and Anderson, D.J. (2011). A Cre-dependent, anterograde transsynaptic viral tracer for mapping output pathways of genetically marked neurons. *Neuron* 72, 938–950. <https://doi.org/10.1016/j.neuron.2011.12.002>.
35. Tobet, S.A., Zahniser, D.J., and Baum, M.J. (1986). Sexual dimorphism in the preoptic/anterior hypothalamic area of ferrets: effects of adult exposure to sex steroids. *Brain Res.* 364, 249–257. [https://doi.org/10.1016/0006-8993\(86\)90837-1](https://doi.org/10.1016/0006-8993(86)90837-1).
36. Bleier, R., Byne, W., and Siggelkow, I. (1982). Cytoarchitectonic sexual dimorphisms of the medial preoptic and anterior hypothalamic areas in guinea pig, rat, hamster, and mouse. *J. Comp. Neurol.* 212, 118–130. <https://doi.org/10.1002/cne.902120203>.
37. Swaab, D.F., and Fliers, E. (1985). A sexually dimorphic nucleus in the human brain. *Science* 228, 1112–1115. <https://doi.org/10.1126/science.3992248>.
38. Singer, J.J. (1968). Hypothalamic control of male and female sexual behavior in female rats. *J. Comp. Physiol. Psychol.* 66, 738–742. <https://doi.org/10.1037/h0026519>.
39. Cruz, M.E., Flores, A., and Domínguez, R. (2014). The cholinergic system of the preoptic–anterior hypothalamic areas regulates the ovarian follicular population in an asymmetric way. *Endocrine* 47, 913–922. <https://doi.org/10.1007/s12020-014-0266-2>.
40. Cain, S.M., and Snutch, T.P. (2010). Contributions of T-type calcium channel isoforms to neuronal firing. *Channels (Austin)* 4, 475–482. <https://doi.org/10.4161/chan.4.6.14106>.
41. Perez-Reyes, E. (2003). Molecular physiology of low-voltage-activated t-type calcium channels. *Physiol. Rev.* 83, 117–161. <https://doi.org/10.1152/physrev.00018.2002>.
42. Huang, Z., Lujan, R., Kadurin, I., Uebele, V.N., Renger, J.J., Dolphin, A.C., and Shah, M.M. (2011). Presynaptic HCN1 channels regulate Ca_v3.2 activity and neurotransmission at select cortical synapses. *Nat. Neurosci.* 14, 478–486. <https://doi.org/10.1038/nn.2757>.
43. Schaukowitz, K., Reese, A.L., Kim, S.-K., Kilaru, G., Joo, J.-Y., Kavalali, E.T., and Kim, T.-K. (2017). An intrinsic transcriptional program underlying synaptic scaling during activity suppression. *Cell Rep.* 18, 1512–1526. <https://doi.org/10.1016/j.celrep.2017.01.033>.
44. Splawski, I., Yoo, D.S., Stotz, S.C., Cherry, A., Clapham, D.E., and Keating, M.T. (2006). CACNA1H mutations in autism spectrum disorders. *J. Biol. Chem.* 281, 22085–22091. <https://doi.org/10.1074/jbc.M603316200>.
45. Viggiano, M., D’Andrea, T., Cameli, C., Posar, A., Visconti, P., Scaduto, M. C., Colucci, R., Rochat, M.J., Ceroni, F., Milazzo, G., et al. (2022). Contribution of CACNA1H Variants in Autism Spectrum Disorder Susceptibility. *Front. Psychiatry* 13, 858238. <https://doi.org/10.3389/fpsy.2022.858238>.
46. Heiman, M., Schaefer, A., Gong, S., Peterson, J.D., Day, M., Ramsey, K.E., Suárez-Fariñas, M., Schwarz, C., Stephan, D.A., Surmeier, D.J., et al. (2008). A translational profiling approach for the molecular characterization of CNS cell types. *Cell* 135, 738–748. <https://doi.org/10.1016/j.cell.2008.10.028>.
47. Soden, M.E., Yee, J.X., and Zweifel, L.S. (2023). Circuit coordination of opposing neuropeptide and neurotransmitter signals. *Nature* 619, 332–337. <https://doi.org/10.1038/s41586-023-06246-7>.
48. Commins, D., and Yahr, P. (1984). Adult testosterone levels influence the morphology of a sexually dimorphic area in the Mongolian gerbil brain. *J. Comp. Neurol.* 224, 132–140. <https://doi.org/10.1002/cne.902240112>.
49. Crosby, E., and Showers, M. (1969). Comparative anatomy of the preoptic and hypothalamic areas. In *The hypothalamus*, W. Haymaker, E. Anderson, and W.T. Nauta, eds. (Charles C Thomas), pp. 61–135.
50. Vasey, P.L., and Pfaus, J.G. (2005). A sexually dimorphic hypothalamic nucleus in a macaque species with frequent female–female mounting and same-sex sexual partner preference. *Behav. Brain Res.* 157, 265–272. <https://doi.org/10.1016/j.bbr.2004.07.005>.

51. Allen, L.S., Hines, M., Shryne, J.E., and Gorski, R.A. (1989). Two sexually dimorphic cell groups in the human brain. *J. Neurosci.* 9, 497–506. <https://doi.org/10.1523/JNEUROSCI.09-02-00497.1989>.
52. Tomita, H., Ohbayashi, M., Nakahara, K., Hasegawa, I., and Miyashita, Y. (1999). Top-down signal from prefrontal cortex in executive control of memory retrieval. *Nature* 401, 699–703. <https://doi.org/10.1038/44372>.
53. Smith, E.E., and Jonides, J. (1999). Storage and executive processes in the frontal lobes. *Science* 283, 1657–1661. <https://doi.org/10.1126/science.283.5408.1657>.
54. Ragozzino, M.E. (2007). The contribution of the medial prefrontal cortex, orbitofrontal cortex, and dorsomedial striatum to behavioral flexibility. *Ann. N. Y. Acad. Sci.* 1121, 355–375. <https://doi.org/10.1196/annals.1401.013>.
55. Rougier, N.P., Noelle, D.C., Braver, T.S., Cohen, J.D., and O'Reilly, R.C. (2005). Prefrontal cortex and flexible cognitive control: rules without symbols. *Proc. Natl. Acad. Sci. USA* 102, 7338–7343. <https://doi.org/10.1073/pnas.0502455102>.
56. Lo, L., Yao, S., Kim, D.W., Cetin, A., Harris, J., Zeng, H., Anderson, D.J., and Weissbourd, B. (2019). Connectional architecture of a mouse hypothalamic circuit node controlling social behavior. *Proc. Natl. Acad. Sci. USA* 116, 7503–7512. <https://doi.org/10.1073/pnas.1817503116>.
57. Knoedler, J.R., Inoue, S., Bayless, D.W., Yang, T., Tantry, A., Davis, C.-h., Leung, N.Y., Parthasarathy, S., Wang, G., and Alvarado, M. (2022). A functional cellular framework for sex and estrous cycle-dependent gene expression and behavior. *Cell* 185, 654–671.e22. <https://doi.org/10.1016/j.cell.2021.12.031>.
58. Yin, L., Hashikawa, K., Hashikawa, Y., Osakada, T., Lischinsky, J.E., Diaz, V., and Lin, D. (2022). VMHvl^{Cckar} cells dynamically control female sexual behaviors over the reproductive cycle. *Neuron* 110, 3000–3017.e8. <https://doi.org/10.1016/j.neuron.2022.06.026>.
59. Qian, T., Wang, H., Wang, P., Geng, L., Mei, L., Osakada, T., Wang, L., Tang, Y., Kania, A., Grinevich, V., et al. (2023). A genetically encoded sensor measures temporal oxytocin release from different neuronal compartments. *Nat. Biotechnol.* 41, 944–957. <https://doi.org/10.1038/s41587-022-01561-2>.
60. Huguenard, J.R. (1996). Low-threshold calcium currents in central nervous system neurons. *Annu. Rev. Physiol.* 58, 329–348. <https://doi.org/10.1146/annurev.ph.58.030196.001553>.
61. Poepl, T.B., Langguth, B., Rupprecht, R., Safron, A., Bzdok, D., Laird, A.R., and Eickhoff, S.B. (2016). The neural basis of sex differences in sexual behavior: A quantitative meta-analysis. *Front. Neuroendocrinol.* 43, 28–43. <https://doi.org/10.1016/j.yfrne.2016.10.001>.
62. Graziottin, A. (2004). Sexual arousal: similarities and differences between men and women. *J. Mens Health Gen.* 1, 215–223. <https://doi.org/10.1016/j.jmhg.2004.07.026>.
63. Rupp, H.A., and Wallen, K. (2008). Sex differences in response to visual sexual stimuli: a review. *Arch. Sex. Behav.* 37, 206–218. <https://doi.org/10.1007/s10508-007-9217-9>.
64. Chivers, L., and Dawson, S.J. (2014). Gender Differences and Similarities in Sexual Desire. *Curr. Sex. Health Rep.* 6, 211–219. <https://doi.org/10.1007/s11930-014-0027-5>.
65. Brotto, L.A. (2010). The DSM diagnostic criteria for Hypoactive Sexual Desire Disorder in men. *J. Sex. Med.* 7, 2015–2030. <https://doi.org/10.1111/j.1743-6109.2010.01860.x>.
66. Brotto, L.A. (2010). The DSM diagnostic criteria for hypoactive sexual desire disorder in women. *Arch. Sex. Behav.* 39, 221–239. <https://doi.org/10.1007/s10508-009-9543-1>.
67. Kuiper, L.B., Frohmader, K.S., and Coolen, L.M. (2017). Maladaptive Sexual Behavior Following Concurrent Methamphetamine and Sexual Experience in Male Rats is Associated with Altered Nucleus Accumbens Activity in Frontal Cortex. *Neuropsychopharmacology* 42, 2011–2020. <https://doi.org/10.1038/npp.2017.1>.
68. Engel, J., Kessler, A., Veit, M., Sinke, C., Heitland, I., Kneer, J., Hartmann, U., and Kruger, T.H.C. (2019). Hypersexual behavior in a large online sample: Individual characteristics and signs of coercive sexual behavior. *J. Behav. Addict.* 8, 213–222. <https://doi.org/10.1556/2006.8.2019.16>.
69. Walton, M.T., Cantor, J.M., and Lykins, A.D. (2017). An Online Assessment of Personality, Psychological, and Sexuality Trait Variables Associated with Self-Reported Hypersexual Behavior. *Arch. Sex. Behav.* 46, 721–733. <https://doi.org/10.1007/s10508-015-0606-1>.
70. Beaugregard, M., Lévesque, J., and Bourgoin, J. (2001). Neural correlates of conscious self-regulation of emotion. *J. Neurosci.* 21, RC165. <https://doi.org/10.1523/JNEUROSCI.21-18-j0001.2001>.
71. Vitale, C., Santangelo, G., Trojano, L., Verde, F., Rocco, M., Grossi, D., and Barone, P. (2011). Comparative neuropsychological profile of pathological gambling, hypersexuality, and compulsive eating in Parkinson's disease. *Mov. Disord.* 26, 830–836. <https://doi.org/10.1002/mds.23567>.
72. Evrensel, A., Tarhan, N., Ceylan, M.E., and Cömert, G. (2015). Inappropriate sexual behaviour due to frontal dementia. *BMJ Case Rep.* 2015, bcr2014207864. <https://doi.org/10.1136/bcr-2014-207864>.
73. Zhu, X., Wang, X., Parkinson, C., Cai, C., Gao, S., and Hu, P. (2010). Brain activation evoked by erotic films varies with different menstrual phases: an fMRI study. *Behav. Brain Res.* 206, 279–285. <https://doi.org/10.1016/j.bbr.2009.09.027>.
74. Abler, B., Kumpfmüller, D., Grön, G., Walter, M., Stingl, J., and Seeringer, A. (2013). Neural correlates of erotic stimulation under different levels of female sexual hormones. *PLoS One* 8, e54447. <https://doi.org/10.1371/journal.pone.0054447>.
75. Krashes, M.J., Koda, S., Ye, C.P., Rogan, S.C., Adams, A.C., Cusher, D.S., Maratos-Flier, E., Roth, B.L., and Lowell, B.B. (2011). Rapid, reversible activation of AgRP neurons drives feeding behavior in mice. *J. Clin. Invest.* 121, 1424–1428. <https://doi.org/10.1172/JCI46229>.
76. Chen, T.W., Wardill, T.J., Sun, Y., Pulver, S.R., Renninger, S.L., Baohan, A., Schreiter, E.R., Kerr, R.A., Orger, M.B., Jayaraman, V., et al. (2013). Ultrasensitive fluorescent proteins for imaging neuronal activity. *Nature* 499, 295–300. <https://doi.org/10.1038/nature12354>.
77. Fenno, L.E., Mattis, J., Ramakrishnan, C., Hyun, M., Lee, S.Y., He, M., Tucciarone, J., Selimbeyoglu, A., Berndt, A., Grosenick, L., et al. (2014). Targeting cells with single vectors using multiple-feature Boolean logic. *Nat. Methods* 11, 763–772. <https://doi.org/10.1038/nmeth.2996>.
78. Hao, Y., Hao, S., Andersen-Nissen, E., Mauck, W.M., 3rd, Zheng, S., Butler, A., Lee, M.J., Wilk, A.J., Darby, C., Zager, M., et al. (2021). Integrated analysis of multimodal single-cell data. *Cell* 184, 3573–3587.e29. <https://doi.org/10.1016/j.cell.2021.04.048>.
79. Gu, Z.G., Eils, R., and Schlesner, M. (2016). Complex heatmaps reveal patterns and correlations in multidimensional genomic data. *Bioinformatics* 32, 2847–2849. <https://doi.org/10.1093/bioinformatics/btw313>.
80. Dobin, A., Davis, C.A., Schlesinger, F., Drenkow, J., Zaleski, C., Jha, S., Batut, P., Chaisson, M., and Gingeras, T.R. (2013). STAR: ultrafast universal RNA-seq aligner. *Bioinformatics* 29, 15–21. <https://doi.org/10.1093/bioinformatics/bts635>.
81. Anders, S., Pyl, P.T., and Huber, W. (2015). HTSeq—a Python framework to work with high-throughput sequencing data. *Bioinformatics* 31, 166–169. <https://doi.org/10.1093/bioinformatics/btu638>.
82. Love, M.I., Huber, W., and Anders, S. (2014). Moderated estimation of fold change and dispersion for RNA-seq data with DESeq2. *Genome Biol.* 15, 550. <https://doi.org/10.1186/s13059-014-0550-8>.
83. Dong, Z., Mau, W., Feng, Y., Pennington, Z.T., Chen, L., Zaki, Y., Rajan, K., Shuman, T., Aharoni, D., and Cai, D.J. (2022). Minian, an open-source microscope analysis pipeline. *eLife* 11, e70661. <https://doi.org/10.7554/eLife.70661>.
84. Sheintuch, L., Rubin, A., Brande-Eilat, N., Geva, N., Sadeh, N., Pinchasof, O., and Ziv, Y. (2017). Tracking the Same Neurons across Multiple Days in Ca2+ Imaging Data. *Cell Rep.* 21, 1102–1115. <https://doi.org/10.1016/j.celrep.2017.10.013>.
85. McLean, A.C., Valenzuela, N., Fai, S., and Bennett, S.A.L. (2012). Performing vaginal lavage, crystal violet staining, and vaginal cytological

- evaluation for mouse estrous cycle staging identification. *J. Vis. Exp.* 67, e4389. <https://doi.org/10.3791/4389>.
86. Lenschow, C., and Lima, S.Q. (2020). In the mood for sex: neural circuits for reproduction. *Curr. Opin. Neurobiol.* 60, 155–168. <https://doi.org/10.1016/j.conb.2019.12.001>.
87. Yao, Z., Liu, H., Xie, F., Fischer, S., Adkins, R.S., Aldridge, A.I., Ament, S. A., Bartlett, A., Behrens, M.M., Van den Berge, K., et al. (2021). A transcriptomic and epigenomic cell atlas of the mouse primary motor cortex. *Nature* 598, 103–110. <https://doi.org/10.1038/s41586-021-03500-8>.
88. Huang da, W., Sherman, B.T., and Lempicki, R.A. (2009). Systematic and integrative analysis of large gene lists using DAVID bioinformatics resources. *Nat. Protoc.* 4, 44–57. <https://doi.org/10.1038/nprot.2008.211>.
89. Hochgerner, H., Singh, S., Tibi, M., Lin, Z., Skarbianskis, N., Admati, I., Ophir, O., Reinhardt, N., Netser, S., Wagner, S., and Zeisel, A. (2023). Neuronal types in the mouse amygdala and their transcriptional response to fear conditioning. *Nat. Neurosci.* 26, 2237–2249. <https://doi.org/10.1038/s41593-023-01469-3>.
90. Hsiao, K., Noble, C., Pitman, W., Yadav, N., Kumar, S., Keele, G.R., Terceiros, A., Kanke, M., Conniff, T., Cheleuitte-Nieves, C., et al. (2020). A Thalamic Orphan Receptor Drives Variability in Short-Term Memory. *Cell* 183, 522–536.e19. <https://doi.org/10.1016/j.cell.2020.09.011>.
91. Yin, X., Wang, Y., Li, J., and Guo, Z.V. (2022). Lateralization of short-term memory in the frontal cortex. *Cell Rep.* 40, 111190. <https://doi.org/10.1016/j.celrep.2022.111190>.

STAR★METHODS

KEY RESOURCES TABLE

REAGENT or RESOURCE	SOURCE	IDENTIFIER
Antibodies		
Rabbit anti-c-Fos	Cell Signaling Technology	Cat#2250s; RRID: AB_2247211
Rabbit anti-RFP	Rockland	Cat#600-401-3; RRID: AB_2209751
Goat anti-Rabbit, Alexa Fluor 594 conjugate	Thermo Fisher Scientific	Cat#A32740; RRID: AB_2762824
Mouse anti-GFP	MSKCC Antibody & Bioresource Core Facility	Cat#Htz-GFP-19C8; RRID: AB_2716737
Mouse anti-GFP	MSKCC Antibody & Bioresource Core Facility	Cat#Htz-GFP-19F7; RRID: AB_2716736
Rabbit anti-Progesterone Receptor	Cell Signaling Technology	Cat#8757; RRID: AB_2797144
Rabbit anti-Estrogen Receptor α	Cell Signaling Technology	Cat#8644; RRID: AB_2617128
Bacterial and virus strains		
H129 Δ TK-TT	PNI Viral Core Facility; Lo and Anderson ³⁴	N/A
AAVretro-EGFP-Rpl10a	Janelia Viral Tools facility	N/A
AAV5-DIO-EGFP-Rpl10a	Janelia Viral Tools facility	N/A
AAV5-Ef1 α -DIO-hChR2-mCherry	Karl Deisseroth	Addgene Cat#20297-AAV5
AAV5-Ef1 α -DIO-EYFP	Karl Deisseroth	Addgene Cat#27056-AAV5
AAV2-hSyn-DIO-hM4D(Gi)-mCherry	Krashes et al. ⁷⁵	Addgene Cat#44362-AAV2
AAV2-hSyn-DIO-hM3D(Gq)-mCherry	Krashes et al. ⁷⁵	Addgene Cat#44361-AAV2
AAV2-hSyn-DIO-mCherry	Bryan Roth	Addgene Cat#50459-AAV2
AAV1-Syn-Flex-GCaMP6f	Chen et al. ⁷⁶	Addgene Cat#100833-AAV1
AAV9-hSyn-DIO-jGCaMP7b	Taitool	Cat#S0592-9
AAV9-hSyn-ChrimsonR-tdTomato-WPRE-pA	Taitool	Cat#S0217-9
AAV8-Ef1 α -mCherry-IRES-Cre	Fenno et al. ⁷⁷	Addgene Cat#55632-AAV8
AAV8-Ef1 α -mCherry	Karl Deisseroth	Addgene Cat#114470-AAV8
Chemicals, peptides, and recombinant proteins		
Picrotoxin (PTX)	Tocris	Cat#1128
D-APV	Sigma-Aldrich	Cat#A5282
CNQX	Sigma-Aldrich	Cat#C127
Tetrodotoxin (TTX)	MREDA	Cat#M046335
4-Aminopyridine (4-AP)	Sigma-Aldrich	Cat#275875
TEA-CI	Sigma-Aldrich	Cat#T2265
Mibefradil	Sigma-Aldrich	Cat#M5441
Oxytocin acetate salt	BACHEM	Cat#H-2510.0025
Clozapine N-oxide (CNO)	Sigma-Aldrich	Cat#C0832
Oxytocin receptor antagonist (Oxtra)	MCE	Cat# HY-108677
CRFR1 antagonist (CRFR1A)	MCE	Cat#HY-135542
17 β -estradiol benzoate	Sigma-Aldrich	Cat#E8875
Progesterone	Sigma-Aldrich	Cat#P0130
Corn oil	Sigma-Aldrich	Cat#C8267
Papain	Worthington	Cat#LK003178
Percoll	Sigma-Aldrich	Cat#P4937
Recombinant RNase inhibitor	Takara	Cat#2313A
DAPI	Sigma-Aldrich	Cat#D9542
Normal Donkey Serum	Jackson ImmunoResearch	Cat#017-000-121

(Continued on next page)

Continued

REAGENT or RESOURCE	SOURCE	IDENTIFIER
Crystal violet	Sigma-Aldrich	Cat#C6158
Dynabeads MyOne Streptavidin T1	Thermo Fisher Scientific	Cat#65601
SUPERase-In RNase Inhibitor	Ambion	Cat#AM2696
RNasin Ribonuclease Inhibitor	Promega	Cat# N2515
Recombinant Protein L, Biotinylated	Pierce	Cat#29997
TSA Plus Cyanine 3	Akoya Biosciences	Cat#NEL744001KT
TSA Plus Fluorescein	Akoya Biosciences	Cat#NEL741001KT
Retrograde tracer CTB-555	Thermolife	Cat#C34776
Fluorescent red retrobeads	LumaFluor Inc.	N/A
Critical commercial assays		
RNeasy Plus Micro Kit	QIAGEN	Cat#74034
Ovation RNA-seq System V2	NuGEN	Cat#7102-32
NEBNext® Ultra™ II DNA Library Prep Kit for Illumina®	New England Biolabs	Cat#E7645S
NEBNext® Multiplex Oligos for Illumina®	New England Biolabs	Cat#E7500S
Bioanalyzer High Sensitivity DNA Analysis	Agilent	Cat#5067-4626
RNAscope® Multiplex Fluorescent Reagent Kit v2	Advanced Cell Diagnostics	Cat#323100
QIAwave RNA Mini Kit	QIAGEN	Cat#74536
PrimeScript™ RT reagent Kit with gDNA Eraser	TaKaRa	Cat#RR047A
PowerUp™ SYBR™ Green	Thermo Fisher Scientific	Cat#A25742
Chromium Next GEM Single Cell 3' Library & Gel Bead Kit v3.1	10X Genomics	Cat#PN-1000268
Chromium Next GEM Chip G Single Cell Kit	10X Genomics	Cat#PN-1000127
SimpleChIP® Plus Enzymatic Chromatin IP Kit	Cell Signaling Technology	Cat#9003
Deposited data		
mPFC scRNA-seq data	This paper	NCBI GEO: GSE227852
TRAP-seq data of AHN-projecting mPFC neurons and mPFC ^{Cacna1h+} neurons	This paper	NCBI GEO: GSE283376
Experimental models: Organisms/strains		
Mouse: Cacna1h-IRES-Cre	Provided by Diane Lipscombe	N/A
Mouse: C57BL/6NCya-Cacna1h ^{em1flox/Cya}	This paper	Strain #: S-CKO-12414
Mouse: Oxtr-Cre ON82	Nakajima et al. ³	N/A
Mouse: Rosa26-flox-EGFP-Rpl10a	The Jackson Laboratory	Strain #: 022367;RRID:IMSR_JAX:022367
Mouse: C57BL/6J	The Jackson Laboratory and Beijing Vital River Laboratory Animal Technology Company (Imported from The Jackson Laboratory)	Strain #: 000664
Oligonucleotides		
RNAscope® Probe-Mm-Oxtr	Advanced Cell Diagnostics	Cat#412171
RNAscope® Probe-Mm-Slc17a7-C2	Advanced Cell Diagnostics	Cat#416631-C2
RNAscope® Probe-Mm-Sst-C3	Advanced Cell Diagnostics	Cat#404631-C3
RNAscope® Probe-Mm-Cacna1h	Advanced Cell Diagnostics	Cat#459751
Real-time qPCR primers of <i>Oxtr</i> ; Forward:TGTCTGGTCA CTGTGCACTC; Reverse:CTAGGCTTTTTGGAAGCGCC	This paper	N/A
Real-time qPCR primers of <i>Cacna1h</i> Forward:GAACGT GGTCTTTACAACGGC; Reverse:GCACATAGTTCCCA AAGTCA	This paper	N/A
Real-time qPCR primers of <i>GAPDH</i> ; Forward:CATGGC CTTCCGTGTTCCCTA; Reverse:GCCTGCTTCACCAC CTTCTT	This paper	N/A

(Continued on next page)

Continued

REAGENT or RESOURCE	SOURCE	IDENTIFIER
Real-time qPCR primers of <i>Pr</i> ; Forward:ACCCCAGAAATG TTGCCAGT; Reverse:GTGACTTCTTTTCTTGCCCC	This paper	N/A
Real-time qPCR primers of <i>Esr1</i> ; Forward:CAGCACCTGC GGAGAGAG; Reverse:GAGACAAAGACATCCCGGCG	This paper	N/A
Software and algorithms		
Miniscope data process pipeline	This paper	https://doi.org/10.5281/zenodo.15203046
CellRanger (3.0.2)	10x Genomics	https://www.10xgenomics.com/support/software/cell-ranger
Seurat (4.0.2)	Hao et al. ⁷⁸	https://github.com/satijalab/seurat
ComplexHeatmap (2.6.2)	Gu et al. ⁷⁹	https://github.com/jokergoo/ComplexHeatmap
STAR (2.3.0e_r291)	Dobin et al. ⁸⁰	https://github.com/alexdobin/STAR
HTSeq (0.6.0)	Anders et al. ⁸¹	https://htseq.readthedocs.io
DESeq2 (1.34.0)	Love et al. ⁸²	https://bioconductor.org/packages/release/bioc/html/DESeq2.html
MiniAn	Dong et al. ⁸³	https://github.com/deniseailab/minian
CellReg	Sheintuch et al. ⁸⁴	https://github.com/zivlab/CellReg
ZEN Digital Imaging for Light Microscopy	ZEISS	http://www.zeiss.com/microscopy/en_us/products/microscope-software/zen.html ; RRID:SCR_013672
CellSens Standard	Olympus	https://www.olympus-lifescience.com.cn ; RRID:SCR_014551
FV31S-SW Viewer software (Ver.2.6)	Olympus	https://www.olympus-lifescience.com.cn
Ethovision XT v15.0 software	Noldus	https://www.noldus.com ; RRID:SCR_000441
GraphPad Prism 8	GraphPad Software	https://www.graphpad.com/ ; RRID:SCR_002798
Adobe Photoshop 2020	Adobe	http://www.adobe.com ; RRID:SCR_014199
Adobe Illustrator 2020	Adobe	http://www.adobe.com ; RRID:SCR_010279
MATLAB	Mathworks	https://www.mathworks.cn/en/products/matlab.html ; RRID:SCR_001622
Python (3.9.10)	Python Software Foundation	http://www.python.org ; RRID: SCR_008394
R Project for Statistical Computing (4.1.2)	The R Foundation	https://www.r-project.org ; RRID: SCR_001905

EXPERIMENTAL MODEL AND STUDY PARTICIPANT DETAILS

All experimental procedures in this study were performed in accordance with the Tsinghua or Rockefeller University guidelines and animal protocols, which were approved by Tsinghua University or The Rockefeller University Institutional Animal Care and Use Committee (IACUC). Wild-type (C57BL/6J, 8 weeks) mice were purchased from The Jackson Laboratory (Strain #: 000664) and Beijing Vital River Laboratory Animal Technology Company (Imported from The Jackson Laboratory, Strain #: 000664). Oxtr-Cre ON82 mouse line was generated at The Rockefeller University.³ *Cacna1h*-IRES-Cre knock-in mouse line was kindly provided by Dr. Diane Lipscombe at Brown University. The conditional knockout mouse line of *Cacna1h* (*Cacna1h*^{fl/fl}) mouse was generated using CRISPR/Cas9 genome editing by Cyagen Biosciences Company (Strain #: S-CKO-12414). In detail, single guide RNAs (sgRNA1 and sgRNA2) targeting *Cacna1h* functional coding region exon 6 were designed, and the donor vector containing exon 6 flanked by two loxP sites and the two homology arms was used as a template. Through homologous recombination in embryonic stem cells, the loxP sites were inserted into the *Cacna1h* exon 6. The correctly targeted embryonic stem cell clones were selected and used to generate chimeric mice, which were then bred with wild-type mice to obtain heterozygous *Cacna1h*^{fl/+} mice. Further breeding of heterozygous mice resulted in the establishment of the homozygous *Cacna1h*^{fl/fl} mouse line. *Rosa26*-flox-EGFP-Rpl10a line was purchased from Jackson Laboratories (Strain #: 022367). *Cacna1h*-IRES-Cre mouse was crossed with *Rosa*-flox-EGFP-Rpl10a line to generate the *Cacna1h*-EGFP-Rpl10a (*Cacna1h*-TRAP) line. All male or female mice used in this study were healthy, aged 3-5 months, same-sex group housed (4-5 mice per cage) unless otherwise specified (See [method details](#)), and were housed on a 12:12 light-dark cycle and were provided food and water ad libitum. The animals were drug/test naïve and had not been involved in any previous procedures. The behavioral experiments were conducted in a blind manner.

METHOD DETAILS

Identification of the female estrous cycle

The estrous cycle of female mice consists of four stages: proestrus, estrus, metestrus, and diestrus, determined by cytological evaluation of vaginal smears.⁸⁵ To assess the cycle, the female mouse's tail was gently grasped, and the vaginal opening was rinsed with sterile saline using a 200 μ l pipette tip. Approximately 100 μ l of residual liquid was then aspirated and released five to eight times to collect the lavage. The pipette tip was never inserted into the vaginal canal to prevent vaginal stimulation. The smears were dried, stained with 0.1% crystal violet (Sigma-Aldrich, C6158), and examined for cytological composition. Proestrus was identified by round nucleated epithelial cells, estrus by anucleated keratinized cells, which appeared smaller and arranged in loose clusters early in estrus, and larger, more evenly dispersed later. Metestrus was characterized by a mix of keratinized epithelial cells and neutrophils, while diestrus featured predominantly neutrophils with few nucleated epithelial cells.

Behavioral testing

Sociosexual preference test

The sociosexual preference test for male and female mice was conducted in a three-chamber social interaction box, as previously described.^{3,33} In brief, prior to the behavioral test, both the subject mice and age-matched, opposite-sex target mice were acclimated to the testing environment for at least one hour. The test consisted of two sessions: habituation (10 minutes of free exploration) and test (10 minutes of exploration with an opposite-sex target mouse and novel object in wire cups). 'Sniff duration' was defined as the total time of subject's nose-point was detected near the wire cup in the social interaction zone, and was manually scored with Ethovision XT v15.0 software. The three-chamber apparatus was sequentially cleaned using 84 disinfectant (5%) and purified water after the behavioral test of each mouse. Post-behavioral testing, estrous cycle phases of experimental females were determined via blind assignment following vaginal cytology. The chemogenetic inhibition experiments of mPFC^{Cacna1h} neurons during the sociosexual preference test in both male and female mice were conducted using animals housed at Rockefeller University, and all other behavioral experiments were performed using mice housed at Tsinghua University. For chemogenetic manipulation, CNO (1 mg/kg) (Sigma-Aldrich, C0832) was administered intraperitoneally 30 minutes before the habituation. For pathway-specific manipulation, CNO (3 μ M) diluted in artificial cerebrospinal fluid (ACSF) and infused into the AHNc through the bilateral cannula (500 nl per side), 30 minutes before testing.

Sex preference test

To test the mouse sex preference between male and female target mice, the sex preference test was performed in a three-chamber social interaction box as previously described.⁵⁸ To assess sex preference in female subjects, sexually experienced males were used as targets in wire cups; for male subjects, male targets were sexually naïve. Prior to the behavioral test, subject mice were single housed for at least one week, and both the subject and target animals were habituated to the chamber for 30 min per day for at least two days. The test consisted of two sessions: habituation (10 minutes of free exploration) and test (exploration with a female and a sexually experienced male in wire cups). The sniff duration for each target was manually scored. The sex preference index was calculated as (sniffing male - sniffing female) / (sniffing male + sniffing female) for females, and as (sniffing female - sniffing male) / (sniffing female + sniffing male) for males.

Sexual behavior test

All sexual behavior experiments were conducted during the dark phase of the circadian cycle. Subject mice were single-housed for at least one week, and both subject and age-matched, opposite-sex target mice were acclimated to the dark environment with infrared illumination for at least one hour prior to testing. For male sexual behavior, a hormonally-primed receptive female was introduced into the male's home cage, and interactions were allowed until male ejaculation or for up to 30 min without ejaculation. Mounting, intromission, and ejaculation were manually scored. For female sexual receptivity test, an estrus or diestrus female was introduced into the home cage of a sexually experienced male, which had been primed by a receptive female 30 minutes prior. The female mouse was allowed to interact with primed male until male ejaculation or for up to 30 min without ejaculation. Female sexual receptivity was measured by the lordosis quotient, calculated as the ratio of lordosis events to male mounts with intromission. Female rejection was calculated as the percentage of quick escape events relative to the total number of male mounts or mount attempts.

Freely moving sociosexual interaction test

Prior to the behavioral test, subject mice were single-housed for at least one week, and both subject and age-matched opposite-sex target mice were habituated to a cylindrical testing arena (35 cm diameter \times 30.5 cm height) for 30 minutes per day over two days. On the test day, the subject mouse was placed in the arena and allowed to habituate for 5-10 minutes. An opposite-sex target mouse was then introduced, and their social interactions were recorded for up to 10 minutes. Social behaviors, including sniffing (subject actively sniffing the target) and avoidance (quick escape, kicking, or boxing when approached by the target⁸⁶) were manually scored with Ethovision XT v15.0 software.

Elevated plus maze

The apparatus comprises a central platform (5 \times 5 cm), two open arms (30 \times 5 cm), and two enclosed arms (30 \times 5 \times 15 cm). The maze was placed 40 cm above the floor, and the light intensity of the maze was adjusted to 110 lux at the start of each experimental day. The test mouse was placed in the central platform facing an open arm and was allowed to move freely in the maze for 10 min. The distance moved and the time spent in the open arms were automatically analyzed by Ethovision XT v15.0 software.

Open field test

Mice were individually introduced into the central zone of the open field apparatus (40 × 40 × 40 cm). The mice were allowed to freely explore their surroundings. Parameters including total distance traveled and the amount of time spent in the central area of the open field were recorded and automatically analyzed for 5 min by Ethovision XT v15.0 software.

Stereotaxic surgeries

Mice were maintained anesthesia and performed surgeries on a stereotaxic frame (RWD, China). Viruses were injected into either the mPFC (AP, +2.00 and +1.80 mm; ML, ±0.35 mm; DV, -1.75 mm), the AHNc (AP, -0.60 mm; ML, ±0.55 mm; DV, -4.95 mm) or the PVN (AP, -0.59 mm; ML, +1.10 mm; DV, -4.80 mm) with calibrated glass pipettes connected to an infusion pump (WPI, USA) at 20 nl/min. To map OxtRIN-connected mPFC projection populations, Cre-dependent H129ΔTK-TT virus was injected into the mPFC of OxtR-Cre ON82 mice (100 nl for each site). To label mPFC^{AHNc-projecting} neurons, CTB-555 was unilaterally injected into the AHNc (150 nl for each site). To label mPFC^{AHNc-projecting} neurons for brain slice electrophysiological recording, red retrobeads were bilaterally injected into the AHNc (100 nl for each site). For pathway-specific chemogenetic manipulation, the chemogenetic viruses were bilaterally injected into the mPFC (200 nl for each site), and the cannulae (250 μm inner diameters) were implanted above the AHNc (AP, -0.60 mm; ML, ±0.55 mm; DV, -4.25 mm) and fixed with dental cement. For optogenetic or fiber photometry experiment, the optic fiber was positioned 0.2 mm above the viral injection sites (mPFC, 400 μm core, NA 0.50; PVN, 200 μm core, NA 0.37). For micro-endoscopic imaging, the GRIN lens (diameter 1.0 mm, length 4.38 mm, catalog no. NEM-050-06-08-520-S-1.0p) was implanted into mPFC (AP, +2.00 mm; ML, -0.40 mm; DV, -1.55 mm) and secured by Krazy Glue and dental cement. The surface of the GRIN lens was protected by Kwik-Sil. After the surgery, mice were placed on a heating pad for recovery and were allowed to recover in their homecage for another 3 weeks before behavioral assays. All viruses (See [STAR Methods](#)) were aliquoted at 1–5 × 10¹² vg/ml for injection.

Brain slice electrophysiological recordings

Brain slice preparation

Adult mice were anesthetized with avertin (2.5% w/v, i.p.) and perfused with 20 mL chilled dissection buffer (oxygenated with 95% O₂, 5% CO₂, 110.0 mM Choline chloride, 25.0 mM NaHCO₃, 1.25 mM NaH₂PO₄, 2.5 mM KCl, 0.5 mM CaCl₂, 7 mM MgCl₂, 25.0 mM Glucose, 11.6 mM Sodium ascorbate, 3.1 mM Pyruvate acid). After decapitation, coronal mPFC slices of 300 μm were sectioned in chilled dissection buffer using a VT1200s vibratome (Leica). The brain slices were incubated in oxygenated ACSF (118 mM NaCl, 2.5 mM KCl, 26 mM NaHCO₃, 1 mM NaH₂PO₄, 10 mM glucose, 1.3 mM MgCl₂ and 2.5 mM CaCl₂, oxygenated with 95% O₂ and 5% CO₂) to recover for 60 minutes at 32°C and then kept at room temperature.

Whole-cell patch-clamp recordings

Whole-cell patch-clamp recordings were performed in the mPFC layer 5 pyramidal neurons with or without fluorescence labeling at 30 °C using a temperature control system (HCT-10, ALA). Signals were recorded using MultiClamp 700B and Digital 1550B (Axon Instruments). Data analysis was performed offline with Clampfit 11.1 (Molecular Devices).

For voltage-clamp recording, the patch pipette (5–8 MΩ) was filled with internal solution containing (in mM): 115 CsMeSO₃, 20 CsCl, 10 HEPES, 2.5 MgCl₂, 4 Na₂ATP, 0.4 Na₃GTP, 10 Na-phosphocreatine, and 0.6 EGTA. To measure sEPSCs and sIPSCs, cells were clamped at -70 mV and 10 mV respectively. Recordings in which series resistance exceeded 30 MΩ were excluded. For current-clamp recording, the internal solution contained (in mM): 130 K-gluconate, 5 KCl, 10 HEPES, 2.5 MgCl₂, 4 Na₂ATP, 0.4 Na₃GTP, 10 Na-phosphocreatine, 0.6 EGTA. Resting membrane potential (RMP) was measured under I = 0 pA mode right after breaking into cells. To measure current-induced firing rate of cells, sequential currents were injected from -20 pA to 340 pA in a 40 pA step during 500 ms. Oxytocin (100 nM, BACHEM, H-2510.0025) and mibefradil (10 nM, Sigma-Aldrich, M5441) were perfused with ACSF to measure their effects on RMP or current-induced firing rate.

To measure light-evoked postsynaptic currents, 470 nm blue light (3 mW, 5 ms) was delivered to the patched cells in the mPFC brain slice by an optic fiber. Cells were clamped at -70 mV for eEPSCs and 10 mV for eIPSCs. Picrotoxin (100 μM, Tocris, 1128) was perfused with ACSF to validate the IPSCs, CNQX (20 μM, Sigma-Aldrich, C127) and D-APV (50 μM, Sigma-Aldrich, A5282) were used to confirm the EPSCs. Peak amplitude was determined by subtracting the baseline value. Synaptic latency was calculated as the interval between the start of light stimulation and the current onset time. To assess the paired pulse ratio, two brief light pulses with 150 ms intervals for eEPSCs and 350 ms intervals for eIPSCs were delivered to the mPFC slices. To isolate monosynaptic responses, eEPSCs and eIPSCs were elicited by a single 5 ms light pulse in the presence of 4-AP (1 mM, Sigma-Aldrich, 275875) and TTX (1 μM, MREDA, M046335).

To isolate T-type calcium currents pharmacologically, 1 μM TTX, 10 mM TEA-Cl (Sigma-Aldrich, T2265), and 1 mM 4-AP were perfused with ACSF in the mPFC slices. The cells were clamped with depolarizing holding potentials (from -110 mV to -45 mV, 300 ms duration). The T-type currents were identified by subtracting traces at two different holding potentials. The amplitude of T-type currents was determined as the peak current in subtracted traces.

RNA sequencing

scRNA-seq and data analysis

The fresh mPFC tissues were extracted using a brain matrix from two estrus female mice, two diestrus female mice, and two male mice. The dissected tissue was transferred to a 15 ml tube containing 20 U/mL pre-activated papain (Worthington, LK003178, 37 °C

for 30 min) and 0.1 U/ μ L recombinant RNase inhibitor (Takara, 2313A). Papain digestion was performed at 34 °C for 20 min. Following digestion, the papain solution was replaced with ice-cold, carbogen-bubbled ACSF (pH 7.2–7.4, 125 mM NaCl, 2.5 mM KCl, 25 mM NaHCO₃, 1.25 mM NaH₂PO₄, 25 mM glucose, 1 mM MgCl₂, and 1 mM CaCl₂, oxygenated with 95% O₂ and 5% CO₂) containing 1% fetal bovine serum (FBS) and 0.1 U/ μ L recombinant RNase inhibitor. The tissue pieces were dissociated using gentle pipetting, to obtain single-cell suspensions. Subsequently, the suspensions were filtered through a 35 μ m cell strainer (Corning, 352235) to remove debris, and then layered onto 30% Percoll (Sigma, P4937, diluted by ACSF containing 1% FBS and 0.1 U/ μ L recombinant RNase inhibitor), followed by centrifugation at 700 g for 10 minutes at 4 °C. After two washes, the cells were resuspended in 1 \times PBS with 0.02% BSA and 0.1 U/ μ L recombinant RNase inhibitor. The cell viability and concentration were determined, and 15000 single cells per sample were uploaded onto 10 \times Genomics 3' library chips, using the Single Cell 3' Library & Gel Bead kit (v.3.1), as per the manufacturer's instructions.

The resulting libraries were sequenced on an Illumina NovaSeq 6000, and the reads were aligned and quantified using the Cell Ranger (version 3.0.2) pipeline on the reference mouse genome (mm10) (https://www.gencodegenes.org/mouse/release_M10.html). Downstream analysis was performed using the R package Seurat (version 4.0.2),⁷⁸ where genes detected in fewer than 3 cells were removed, and cells with nCount_RNA > 1000 and nCount_RNA < 30000, and nFeature_RNA > 500 and nFeature_RNA < 7000 were retained. Potential low-quality cells were filtered out based on a mitochondrial or ribosomal gene percentage greater than 20%. To correct for batch effects, the expression matrices across all three conditions (estrus, diestrus, and males) were integrated using FindIntegrationAnchors and IntegrateData functions of Seurat. We then identified 5000 highly variable genes using FindVariableGenes and performed principal component analysis (PCA) with RunPCA. Dimension reduction was performed with t-distributed stochastic neighbor embedding (t-SNE) using RunTSNE. Next, we performed cell clustering with FindClusters (resolution = 0.2) and identified cluster markers using FindAllMarkers with the default parameters. We used Snap25 to identify the neuron clusters. A total of 5705 high-quality neurons were extracted, including 827 neurons from estrus, 1901 neurons from diestrus, and 2977 neurons from males. To annotate subclusters of mPFC neurons, clustering analysis was performed with FindClusters (resolution = 0.5), and annotation was used with well-known marker genes of the whole cortex or mPFC single cell RNA-seq and the dataset from Allen Brain Atlas.^{28,29,87} Finally, we used FindMarkers with the default parameters to find DEGs among different estrus/sex state comparisons (estrus vs diestrus, estrus vs males, diestrus vs males). To elucidate how ovarian hormone fluctuations impact individual cell types, DEGs were identified using a p-value cutoff (< 0.05) for the estrus vs. diestrus comparison within each cell type. They were clustered based on the Euclidean distance calculated using their $-\log_{10}(p_val)$ and the hierarchical clustering algorithm in the R package stats (version 4.0.3). The resulting clusters were visualized using a heatmap generated with the ComplexHeatmap R package (version 2.6.2).⁷⁹ DEGs with similar patterns were grouped closely and identified by colors on the heatmap. These cell-type-specific DEG clusters were termed gene modules responding to ovarian hormone fluctuations. We used DAVID⁸⁸ to perform GO enrichment analysis, and filtered enriched Biological Process terms with GeneCount \geq 2 and p-value < 0.05. We removed synonymous and unassociated GO terms for clarity.

To identify neurons with high IEG expression and determine estrous cycle- or sex-specific activated clusters, a set of estrogen- or progesterone-regulated IEGs (*Fos*, *Jun*, *Junb*, *Npas4*, *Nr4a1*, *Btg2*, *Tns1*, *Ptgs2*, *Per1*, *Per2*, *Mcl1*, *Dusp6*, *Irs2*, *Kdm6b*, *Ifrd1*, *Cdkn1a* and *Pim1*) was selected,^{30–32} the 90th percentile expression for each IEG in estrus, diestrus or male samples was calculated.⁸⁹ The neuron was defined “IEG^{high} cell” if the expression of any IEGs exceeded the 90th percentile. ΔIEG^{high} cell percentage among different estrus/sex state comparisons (estrus vs diestrus, estrus vs males, diestrus vs males) was calculated by the difference of IEG^{high} cell percentage of each comparison.

Pathway-specific TRAPseq and cell type-specific TRAPseq

For pathway-specific TRAPseq, retrograde viruses rAAV2-EGFP-Rpl10a (Janelia Viral Tools facility, 500 nl for each site) were injected into the AHNc of wild type mice. The mPFC regions from three male and five female mice with AHNc virus injection were used for independent TRAP replicates. For cell type-specific TRAPseq, three male and eight female *Cacna1h-IRES-Cre::EGFP-Rpl10a* mice of four distinct estrous cycles were used for independent TRAP replicates. The TRAP procedure was performed as described previously.⁴⁶ The mPFC cortices were dissected in dissection buffer (1 \times HBSS, 2.5 mM HEPES-KOH 35 mM Glucose, 4 mM NaHCO₃, RNase-free water, freshly added 100 μ g/mL cycloheximide) using a brain matrix one month after retrograde viral infection. The tissues were immediately homogenized in an ice-cold homogenization buffer (150 mM KCl, 10 mM HEPES pH 7.4, 5 mM MgCl₂, 0.5 mM dithiothreitol (Sigma-Aldrich, D9779), 100 μ g/mL cycloheximide (Inalco, 1758-9310), 20 U/ μ L SUPERase-In RNase Inhibitor (Ambion, AM2696), 40 U/ μ L RNasin Ribonuclease Inhibitor (Promega, N2515), and EDTA-free protease inhibitors) in the cold room using a motor-driven Teflon glass homogenizer. Polyribosomes were immunoprecipitated by monoclonal anti-EGFP antibodies (MSKCC Antibody & Bioresource Core Facility, a mixture of clones 19C8 and 19F7) that have been conjugated to Dynabeads MyOne Streptavidin T1 (Thermo Fisher Scientific, 65601), which were pre-incubated with Recombinant Protein L (Pierce, 29997) for 16 hours at 4 °C on an end-over-end rotator. The RNeasy Plus Micro Kit (QIAGEN, 74034) was used to extract and purify RNAs from ribosomes according to the manufacturer's instructions. The RNA quality was evaluated using an Agilent 2100 Bioanalyzer (Agilent Technologies, USA). Then, using a total of 5 ng mRNA from each IP and INPUT sample, cDNA was synthesized and further amplified using the Ovation RNA-seq System V2 Kit (NuGEN, 7102-32). cDNA fragments of 200 bp were end-repaired and ligated with adapters for NextSeq 500 technology using NEBNext Ultra™ II DNA Library Prep Kit (New England Biolabs, E7645L) and NEBNext® Multiplex

Oligos (New England Biolabs, E7500S) for Illumina. The cDNA libraries were sequenced on the NextSeq 500 System (Illumina Inc., San Diego, CA, USA). The quality of libraries was evaluated by using Bioanalyzer High Sensitivity DNA Analysis (Agilent, 5067-4626) on the Agilent 2200 TapeStation system.

Sequencing reads were aligned to the UCSC mm10 reference genome with STAR (version 2.3.0e_r291).⁸⁰ Aligned reads were quantified by the 'htseq-count' module of 'HTSeq' framework (version 0.6.0).⁸¹ Differential gene expression analysis was performed using DESeq2 (version 1.34.0).⁸² Genes were identified as differentially expressed with a false discovery rate (FDR) adjusted p value < 0.05 and log₂Fold Change > 1.2 or < -1.2. To identify all DEGs linked with female estrous cycle, we performed pairwise comparisons of four samples collected at different estrous phases (proestrus, estrus, metestrus and diestrus) and extracted DEGs in at least one pairwise comparison. The DEGs were hierarchically clustered into 5 clusters with distinct expression patterns across the estrous cycle. We used DAVID to perform the GO enrichment analysis, and enriched Biological Process terms were filtered with GeneCount ≥ 2 and p value < 0.05. The synonymous and unassociated GO terms were removed for clarity. Fold Enrichment was calculated by GeneRatio/BgRatio.

Transcription factor (TF) motif analysis

To identify the putative TF binding sites in the promoter of *Cacna1h*, we scanned the promoter region (±2 kb) of *Cacna1h* by FIMO (MEME suite v5.4.1) (<https://meme-suite.org/meme/tools/fimo>) to identify TF motifs occurrences with parameters as follows: P value < 10⁻⁴, a first-order Markov background model, and position weight matrices (PWMs) from the mouse HOCOMOCO motif database (v11) (https://hocomoco11.autosome.org/downloads_v11).

Chromatin immunoprecipitation (ChIP) assays

ChIP assay was performed using the SimpleChIP® Plus Enzymatic Chromatin IP Kit (Cell Signaling Technology, 9003) according to the manufacturer's protocol. Using the Bioruptor® Pico sonication device (Diagenode) to break nuclear membrane. Equal volumes of chromatin were immunoprecipitated with either antibody against Progesterone Receptor A/B (Cell Signaling Technology, 8757T), Estrogen Receptor α (Cell Signaling Technology, 8644T), mouse IgG as a negative control, or mouse H3 as a positive control. Primers 5'-ACCCAGAAATGTTGCCAGT-3' and 5'-GTGACTTCTTTTCTTGGCCCC-3' were designed to amplify the region of PR-binding site of *Cacna1h* promoter. Primers 5'-CAGCACCTGCGGAGAGAG-3' and 5'-GAGACAAAGACATCCCGGCG-3' were designed to amplify the region of ERα-binding site of *Cacna1h* promoter.

Calcium imaging

Fiber photometry recording and data analysis

The fiber photometry system used for recording calcium signals was built as previously described.⁹⁰ In brief, GCaMP6f fluorescence and isosbestic autofluorescence signals were excited by the fiber photometry system using 473 nm (Thorlabs M470F3) and 405 nm (Thorlabs M405FP1) LEDs, and collimated into a dichroic mirror holder with a 425 nm long pass filter (Thorlabs DMLP425R). This is further passed into another 495 nm long pass dichroic (Semrock FF495-Di02-25x36) to direct the light from LEDs into the fiber patch cord (Doric lenses, 400 μm core, 0.48 NA) via a 10×/0.5 NA Objective lens (Nikon CFI SFluor 10x, Product No. MRF00100). The light intensity at the interface between the fiber tips was adjusted to 10-50 μW. The emitted GCaMP6f fluorescence is transmitted back from the same cable, redirected by the 495 nm long pass dichroic to a GFP emission filter (Semrock FF01-520/35-25) and focused onto a high sensitivity sCMOS camera (Prime 95b, Photometrics) for amplification and recording. A custom-made JK flip-flop was used to alternate between 405 nm and 470 nm which takes the trigger input from the sCMOS and alternatively triggers the two LEDs. Bulk activity signals were collected using the PVCAM software, and data were further post-processed and analyzed using custom MATLAB scripts.

To synchronize animal behaviors with calcium signals, the behavior-relevant TTL inputs were triggered by Ethovision XT software. Signals F473 nm and F405 nm were alternatively recorded while the animals were performing sociosexual preference test. The signal was processed at a frame rate of 7.5 Hz. The 405 nm signal was scaled to best fit the 470 nm signal using the least squared regression. After subtracting this scaled 405 nm fluorescence from the 470 nm signal, we got the ΔF/F by dividing this value by the scaled 405 nm signal: $F_n(t) = 100 \times [F_{470}(t) - F_{405fit}(t)] / F_{405fit}(t)$. Behavioral events were manually time-stamped on the recorded animal tracking videos using EthoVision program. For the peri-event time histogram (PETH) analysis, the average activity from -5-3 s around behavioral bout onset of each mouse was calculated across all trials. Then mean F_0 and the standard deviation SD_0 of baseline signals were calculated from -5 to -3 s prior to each onset. And the ΔF/F Z-Score of a given behavior was constructed by $[F_n(t) - F_0] / SD_0$. The change of mean fluorescence was defined as the averaged ΔF/F Z-Score between 0-3 s minus the averaged ΔF/F Z-Score between -3-0 s. As to the trial-by-trial analyses, ΔF/F Z-score of each trial was processed by the same method but without averaging F_0 across trials. Post-processing and plotting of data were performed with the custom MATLAB scripts.

Miniscope imaging

For micro-endoscopic imaging, AAV2/9-hSyn-DIO-jGCaMP7b-WPRE-pA was injected into the mPFC of *Cacna1h*-IRES-Cre mice (250 nl for each site). Two weeks after virus injection, the cortex above the injection sites was removed and the GRIN lens was implanted. Two to three weeks after the implantation of the GRIN lens in the mouse brain, GCaMP expression was checked by Miniscope V4 system (UCLA Miniscope, from OpenEphys). The Miniscope was slowly lowered to the surface of the GRIN lens. If clear

GCaMP-expressing neurons were in focus, the baseplate was fixed with dental cement. Before the behavioral testing, mice were habituated wearing the Miniscope while freely moving for at least 3 times within 1 week.

Extraction of single cell calcium signals

The raw calcium fluorescence videos were processed with MiniAn,⁸³ an open-source package based on CNMF. The footprints and traces were then manually checked. Cells with abnormal footprints or signals were excluded from analysis. The pipeline based on MATLAB is available at <https://zenodo.org/records/15220481>.

Single cell response analysis

To identify responsive neurons, we applied the receiver operating characteristic (ROC) analysis based on behavior tags and neural response. The area under ROC (auROC) measured modulation by specific behaviors. A null distribution was generated via 1000 circular permutations of calcium signals. Neurons exceeding the 97.5th percentile were classified as activated, those below the 2.5th percentile as inhibited, and those with multiple responses as mixed.

To obtain average single-cell responses, activity from 5 s before to 5 s after behavior bout onset of each neuron was averaged. Responses were z-scored using the mean (Fm) and standard deviation (s.d.) over a 2 s baseline (–5 to –3 s). Bouts shorter than 4 s or with intervals under 5 s were excluded.

Classifying sniffing object with support vector machine (SVM)

For time-evolving decoding, we constructed a linear SVM classifier with LibSVM for each 10 frames with randomly selected 15 (in sociosexual preference test) or 25 (in sex preference test) neurons to decode the trial type (sniffing mouse or sniffing object). Sessions with at least 5 (sociosexual) or 10 (sex preference) trials were included (trials with a gap of less than 3 seconds and a duration of less than 1 second were excluded). We then randomly selected 5 trials for classifying mice against object and 10 trials for classifying male against female in each trial type for each category. The accuracy is reported as mean accuracy of 5-fold cross validation. The process was repeated 50 times.

For statistics, we constructed a SVM classifier for data from 0–2 s activity (60 frames in total and down sampled into 20 frames) after sniffing onset with all the other parameters the same as above.

A pseudo-neuron population was constructed to assess whether lower accuracy in male or diestrus female mice stems from fewer recorded neurons or a smaller proportion contributing to decoding. For each session, we randomly selected 5 trials, aligned neuron activity across sessions, and trained using 1 to 100 randomly chosen neurons. Decoding was repeated 30 times, with accuracy reported as the mean from leave-one-out cross-validation (LOOCV).

Analysis of population activity in low dimensional space

To determine the contribution of neural data from each trial type to SVM classification in sex preference behavior, we projected neural data onto the SVM hyperplane. This draws parallels with the concept of coding direction, which best separates the response vectors of different trial types.⁹¹ For n-neurons population we obtained an $n \times 1$ SVM weight or hyperplane direction (HD) which best separates the sniffing male and female response. With activity vector denoted as x , and the projected activity of each frame is then formulated as $HD^T \cdot x$. The absolute projected value reflects the distance to the classification plane, with larger distances indicating greater contribution. Additionally, lower projection results (smaller dot product with SVM weight) may suggest that neurons responsive to certain trial types are assigned smaller weights, thereby contributing less to classification.

To visualize the distribution of dataset, the neural data of each trial was projected onto a 2-dimensional principal component plane. The plane was calculated based on 0–2 s activity of each trial and activity of baseline period.

Decoding estrus and diestrus state with each behavior

A linear SVM was trained for each mouse to classify estrus vs. diestrus based on neural activity during specific behaviors. Only neurons recorded in both states were used (neurons were aligned with CellReg⁸⁴). Neural activity of each trial (0–4 s after behavior onset) served as a sample for training and testing. We randomly selected the minimum number of trials from each state 50 times and reported the mean accuracy (Figure 5H) to ensure balanced sampling. The behavior onset time of each homecage and habituation trial was randomly sampled 100 times to solve the problem of no behavior onset.

Decoding sex of social targets with estrus or diestrus neural activity

A linear SVM decoder of each mouse was trained to distinguish sniffing female and sniffing male behavior with neural activity in specific self-estrus state. In each mouse, only the neurons that were recorded in both estrus and diestrus state were selected for decoding. Neural activity of each trial (0–4 s after behavior onset) served as a sample. To balance the number of samples, the minimum number of sniffing female and male trials were selected 50 times and reported the mean accuracy (Figure 5E).

Clustering and finding subpopulations

Neurons recorded in both the estrus and diestrus states were selected. A total of 162 neurons across all mice were retained for further analysis. We employed the K-means clustering algorithm to classify and extract subpopulations of mPFC^{Cacna1h+} neurons that respond during different stages of the estrus and diestrus states (Figure 5I). The number of clusters is determined by a combination of Sum of Squared Errors (SSE) and Silhouette Coefficient. SSE is the sum of squares of the distances from each point to the nearest cluster center. Lower SSE value suggests a better solution. The Silhouette Coefficient combines clustering density with the degree of separation with higher values indicating better clustering structure. Cluster number is selected based on the elbow of SSE and the local maximum of average Silhouette Coefficient (Figures S5B and S5C).

Optogenetic activation and fiber photometry recording experiment

The experimental protocol of optogenetic activation and fiber photometry recording was based on previous research.⁴⁷ AAV2/9-hSyn-DIO-jGCaMP7b-WPRE-pA was injected into the mPFC (250 nl for each site), and AAV2/9-hSyn-ChrimsonR-tdTomato-WPRE-pA was injected into the PVN (200 nl for each site) of *Cacna1h-IRES-Cre* female mice, followed by optic fiber implantation in the mPFC. The CRFR1 antagonist NBI-27914 (10 mg/kg; MCE, HY-135542) was administered intraperitoneally, and calcium signals of mPFC^{*Cacna1h*⁺} neurons were recorded 30 min after drug treatment. Subsequently, a mixture of CNQX (1 mg/kg; Sigma-Aldrich, C127) and D-APV (10 mg/kg; Sigma-Aldrich, A5282) was administered intraperitoneally, and recordings were performed 10 min later. For OxtR blockade, the OxtR A L-368,899 (10 mg/kg; MCE; HY-108677) was injected intraperitoneally, and recordings were made 20 min later. PVN neurons were optogenetically activated with 589 nm yellow light (2 mW, 3 s square wave) after a 2-min baseline. The calcium signal of mPFC^{*Cacna1h*⁺} neurons was collected using a Doric photometry recording system (blue light: 470 nm, 20 μ W; purple light: 405 nm, 2 μ W). Custom MATLAB code was used to extract and analyze the GCaMP signal surrounding each stimulation. Peak amplitudes of the first signal peak during stimulus onset and the rebound peak after light cessation were quantified.

RNAscope

To detect RNA expression in the mPFC, mice were perfused with PBS followed by 4% paraformaldehyde solution (PFA). Brains were post-fixed in 4% PFA overnight and dehydrated in a 30% sucrose solution at 4 °C for 36 h. The mPFC region was sliced in 14- μ m sections by cryostat and mounted on Fisher brand slides. The sections were air-dried at room temperature and then stored at -80 °C until use. On the day of staining, the slides were rinsed with PBS after drying for 1 hour at 65 °C. The sections were treated with RNAscope® Hydrogen Peroxide solution to eliminate non-specific background signals. Then the sections were recovered in pre-heated Target Retrieval Reagent and digested by RNAscope® Protease III. To detect the target RNAs, commercial RNA-specific probes (ACDbio RNAscope®) were hybridized with the sections. In order to magnify the probe signals, sections were further sequentially incubated in a cascade of signal amplification reagents. TSA Plus Cyanine 3 and TSA Plus Fluorescein (Akoya Biosciences, NEL744001KT and NEL741001KT) were linked to the probes to visualize target genes. To access the percentage of colocalization between target genes and mCherry+ signals, the slides were blocked by 3% Normal Donkey Serum (Jackson ImmunoResearch, 017-000-121) for 1 hour at room temperature following the RNA hybridization protocol. Then the slides were incubated with primary anti-RFP (Rockland, 600-401-379, 1:500) antibody for 16 hours at 4 °C, followed by secondary Alexa-594 antibody (Thermo Fisher Scientific, A32740, 1:1000) for 1 hour at room temperature. Finally, the sections were counterstained with DAPI (Sigma-Aldrich, D9542, 1:10000) and mounted with antifade mounting solutions in preparation for imaging. In accordance with the ACD guidelines, the RNA levels of target genes identified by RNAscope probes were manually quantified by counting the number of punctate dots in individual cells.

c-Fos immunohistochemistry staining

Estrus and diestrus females underwent the sociosexual preference test. As a baseline control, a separate group was presented with a novel object in the wire cup on one side and an empty cup on the other, allowing an equivalent duration of exploration. After 1.5 hours, the mice were deeply anesthetized by avertin (2.5% w/v, i.p.) and perfused with PBS followed by 4% PFA. The brains were post-fixed in 4% PFA overnight and dehydrated in a 30% sucrose solution at 4 °C. For immunofluorescent staining, the brains were cryosectioned into 40 μ m (Leica, CM3050S), blocked with 3% Normal Donkey Serum diluted in PBST (0.1% Triton X-100 diluted in PBS), and incubated with primary anti-c-Fos (Cell Signaling Technology, 2250s, 1:500) antibody for 36 hours at 4 °C. Goat anti-Rabbit Alexa 594 (Thermo Fisher Scientific, A32740, 1:1000) was used as the secondary antibody. All sections were imaged using Olympus IXplore Spin Spinning Disk Microscope with 10X objective lens. For cell counting, the images were registered to the standard Allen Mouse Brain Reference Atlas to analyze the c-Fos-positive cell numbers in different brain regions.

Ovariectomy surgery and hormonal priming

Bilateral ovaries were removed by cautery excision, and meloxicam (4 mg/kg) was administered subcutaneously for 3 days post-surgery. Two weeks after recovery, OVX mice were randomized into control and experimental groups. To induce estrus, the experimental group received 17 β -estradiol benzoate (Sigma-Aldrich, E8875) (10 μ g/mouse on day 1 and 5 μ g/mouse on day 2) and progesterone (Sigma-Aldrich, P0130) (50 μ g/mouse on day 3) dissolved in corn oil (Sigma-Aldrich, C8267) via subcutaneous injection.⁵⁷ Controls received equivalent vehicle injections. Estrus stages were determined by vaginal smear cytology 24 hours after progesterone administration. mPFC tissues were then dissected for RT-qPCR analysis.

Real-time quantitative PCR

The mPFC tissues were dissected from wild-type mice, *Cacna1h*^{*fl/fl*} mouse line and ovariectomized female mice. Total RNAs were extracted and purified by the QIAwave RNA Mini Kit (QIAGEN, 74536). The first strand cDNAs were reverse transcribed from RNAs by PrimeScript™ RT reagent Kit with gDNA Eraser (TaKaRa, RR047A). Quantitative real-time PCR was performed using PowerUp™ SYBR™ Green (Thermo Fisher Scientific, A25742) in a BioRad system. RNA quantification was analyzed by the delta Ct method with *Gapdh* as an endogenous control. Brain samples of different groups in the same experiment were processed in parallel.

QUANTIFICATION AND STATISTICAL ANALYSIS

Statistical parameters including the sample size, scale bars, statistical test used, and statistical significance were reported in the Figures, Figure Legends, and [Table S1](#). All the data in the figures were judged to be statistically significant when $p < 0.05$ by two-tailed Student's t -test, one-way ANOVA or two-way ANOVA. In the figures, asterisks indicate statistical significance (*, $p < 0.05$; **, $p < 0.01$; ***, $p < 0.001$; ****, $p < 0.0001$) as compared to controls. For the Student's t -test, if the data satisfied the normality, parametric methods were used. But if the data did not follow the normal distribution, the nonparametric Mann-Whitney test was used. All values are presented as mean \pm SEM unless otherwise stated. Age-matched mice were randomly assigned to the control or experimental groups. The mice in the control group were age-matched littermates whenever possible. All statistic and data analyses were performed by Prism, MATLAB, and R.

Supplemental figures

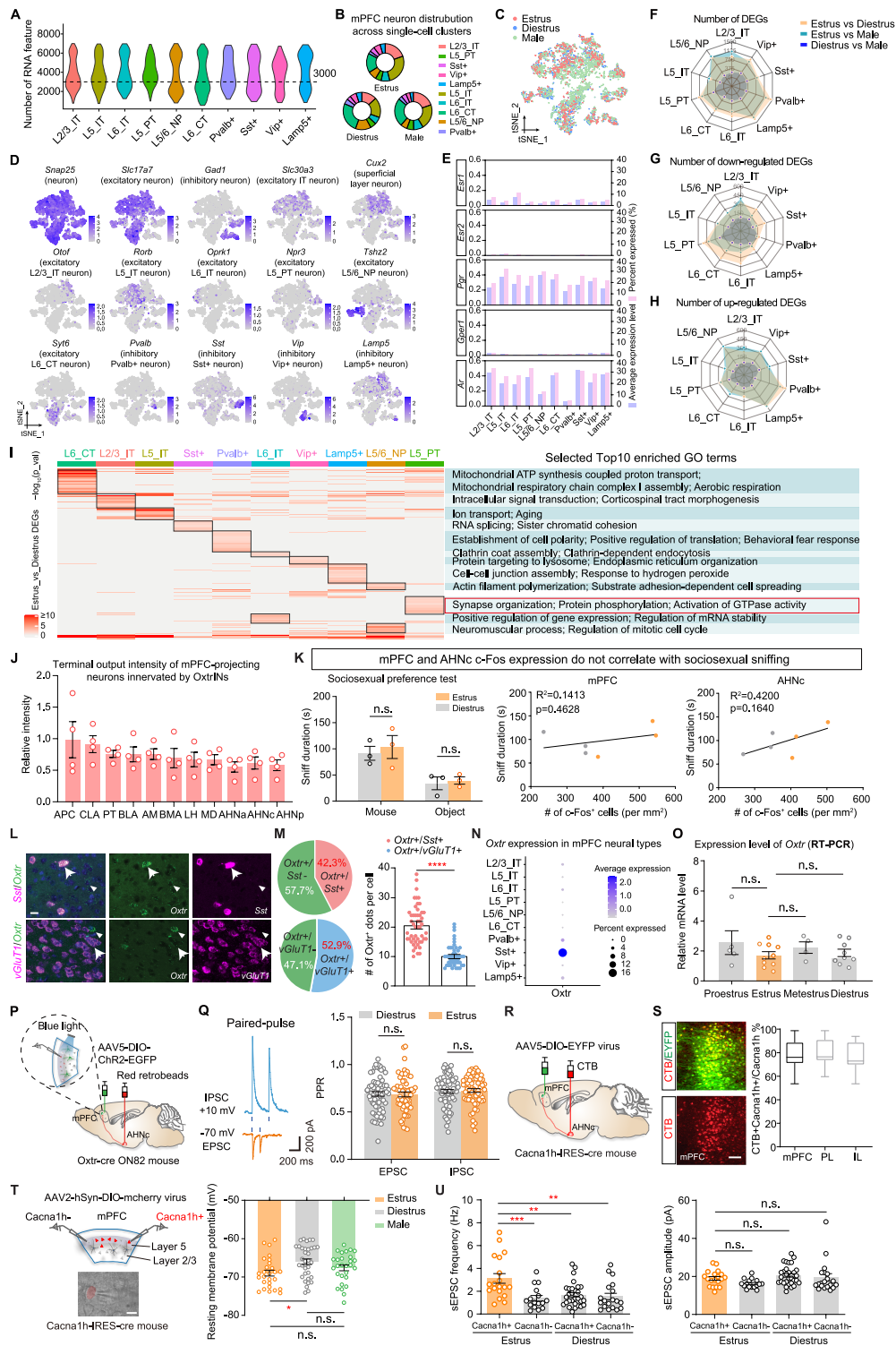
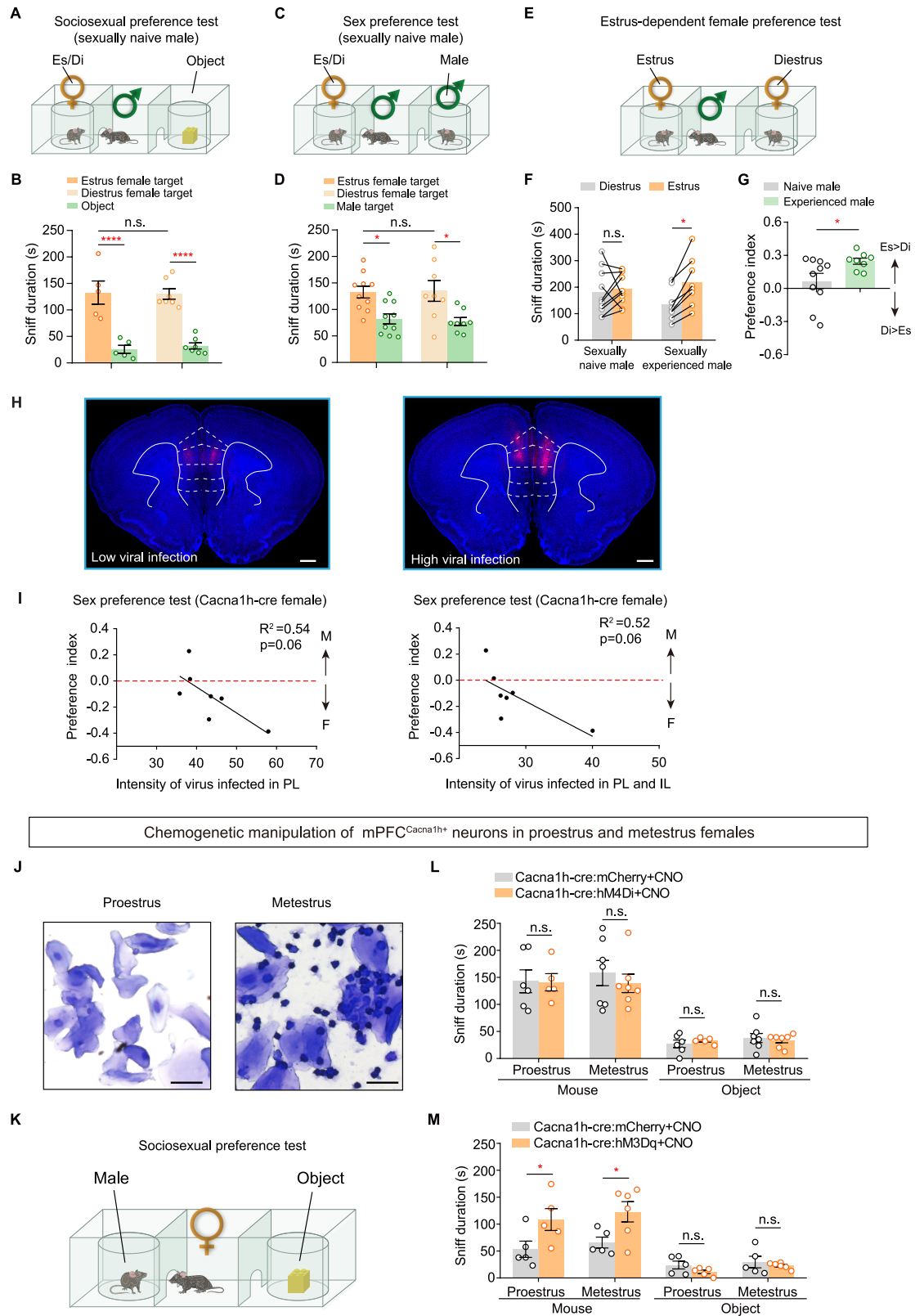


Figure S1. Single-cell transcriptomic analysis and characterization of OxtRINs and Cacna1h⁺ neurons in the mPFC across estrous states and sex, related to Figure 1

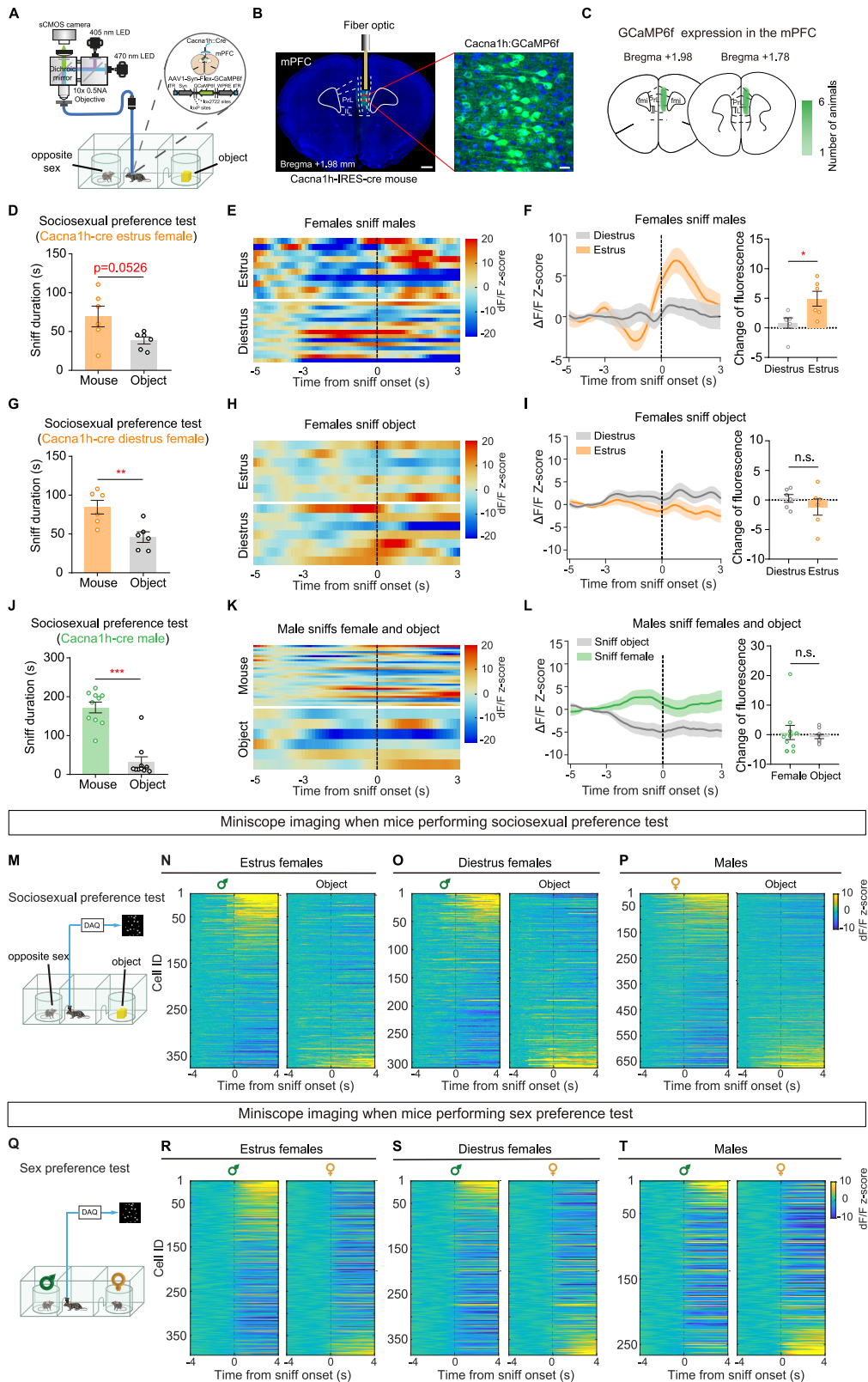
- (A) Violin plot showing the number of genes detected in each neural type.
- (B) Donut plot showing the proportion of mPFC neuron clusters under the different sample conditions.
- (C) t-SNE visualization of mPFC neuron clusters, colored according to different sample conditions.
- (D) t-SNE visualization of marker genes expressed in 10 neural clusters identified in the mPFC. The expression level is depicted from gray (low) to blue (high).
- (E) The expression level and percentage of hormone receptor genes including *Esr1*, *Esr2*, *Pgr*, *Gper1*, and *Ar*, in each mPFC neural clusters.
- (F–H) Radial plot of DEGs in neural cluster comparisons: showcases counts of all (F), down-regulated (G), and up-regulated DEGs (H) across estrus vs. diestrus, estrus vs. male, and diestrus vs. male.
- (I) Heatmap shows gene modules of cell-type-specific DEGs in estrus vs. diestrus comparison of each neuron cluster. Right, selected Top10 enriched GO terms.
- (J) Quantitative analysis of infection intensity in neurons labeled by the H129ΔTK-TT virus, which receive inputs from OxtRIN-innervated projection neurons in the mPFC. $n = 4$ mice.
- (K) Analysis of male-directed sniffing duration in female mice used for c-Fos labeling (left). Correlation of c-Fos expression and male-directed sniffing duration of female mice in mPFC (middle) and AHNc (right). $n = 3$ mice/group. Two-way ANOVA, Bonferroni multiple comparisons tests (left).
- (L) RNAscope *in situ* hybridization of endogenous *Sst*, *vGluT1*, and *Oxtr* in the mPFC. Representative images showing the co-localization of *Sst* (magenta) and *Oxtr* (green) mRNAs in the mPFC neurons (top, arrow indicates *Sst*+/*Oxtr*+ neuron; arrowhead indicates *Sst*-/*Oxtr*+ neuron; scale bar, 20 μ m). Representative images showing the co-expression of *vGluT1* (magenta) and *Oxtr* (green) mRNAs in the mPFC neurons (bottom, arrow indicates *vGluT1*+/*Oxtr*+ neuron; arrowhead indicates *vGluT1*-/*Oxtr*+ neuron).
- (M) Pie charts showing the percentage of endogenous *Sst*+/*Oxtr*+ neurons and *vGluT1*+/*Oxtr*+ neurons to *Oxtr*+ neurons in the mPFC, respectively (left). Quantitation of *Oxtr*+ dots as shown by RNAscope signals in *Sst*+/*Oxtr*+ neurons and *vGluT1*+/*Oxtr*+ neurons (right) ($n = 50$ cells/group; two-tailed unpaired t test).
- (N) Dot plot demonstrating the percentage of cells expressing the *Oxtr* gene across distinct mPFC neuronal types.
- (O) RT-qPCR of *Oxtr* mRNA expression in the mPFC of females across four distinct estrous phases ($n = 4$ –10 mice/group, one-way ANOVA, and Bonferroni multiple comparisons tests).
- (P) Strategy for measuring the paired pulse ratio in mPFC^{AHNc-projecting} neurons.
- (Q) Quantification of the PPR of IPSC and EPSC in mPFC^{AHNc-projecting} neurons from females in estrus and diestrus groups. The PPR is defined as the second evoked amplitude divided by the first evoked amplitude. $n = 56$ –67 cells from 3 mice/group (right). Two-way ANOVA, Bonferroni multiple comparisons tests.
- (R) Injection of AAV5-DIO-EYFP into the mPFC and CTB-555 into the AHNc of *Cacna1h*-IRES-Cre mouse.
- (S) Co-localization of EYFP-labeled mPFC^{Cacna1h+} neurons and CTB-positive mPFC^{AHNc-projecting} neurons in the mPFC (left). Quantitative analysis of the ratio of AHNc-projecting mPFC^{Cacna1h+} neurons to the total population of *Cacna1h*-expressing neurons in the prelimbic (PL), infralimbic (IL), and overall mPFC regions (right). Scale bar, 100 μ m.
- (T) mPFC scheme showing the recordings in *Cacna1h*+ neurons and *Cacna1h*- neurons in the mPFC (left). Scale bar, 20 μ m. RMP recorded from mPFC^{Cacna1h+} neurons in the indicated groups. $n = 27$ –35 cells/group (right). One-way ANOVA, Bonferroni multiple comparisons tests.
- (U) sEPSCs frequency (left) and amplitude (right) of mPFC^{Cacna1h+} neurons and mPFC^{Cacna1h-} neurons in estrus and diestrus females ($n = 16$ –30 cells/group, one-way ANOVA, and Bonferroni multiple comparisons tests).
- * $p < 0.05$, ** $p < 0.01$, *** $p < 0.001$, **** $p < 0.0001$; n.s., not significant; data represent mean \pm SEM.



(legend on next page)

Figure S2. Sexual experience and mPFC^{Cacna1h⁺} neuron activity regulate sociosexual preference in males and females, related to Figures 2 and 3

- (A) Schematic diagram showing sexually naive males sniffing an estrus female or diestrus female and an object in sociosexual preference test.
- (B) Quantification of male sniffing behaviors toward female or object in sociosexual preference test. $n = 5-7$ mice/group. Two-way ANOVA, Bonferroni multiple comparisons tests.
- (C) Schematic illustration showing sexually naive males sniffing an estrus female or diestrus female and a male in sex preference test.
- (D) Quantification of sniff duration by sexually naive males toward estrus or diestrus females and males in sex preference test. $n = 8-10$ mice/group. Two-way ANOVA, Bonferroni multiple comparisons tests.
- (E) Schematic illustration showing sexually naive and experienced males sniffing estrus and diestrus females during an estrus-dependent female preference test.
- (F and G) Quantification of sniff duration toward estrus and diestrus females (F) and calculation of preference index (G) in sexually naive and experienced males during the estrus-dependent female preference test. $n = 8-10$ mice/group. Two-tailed paired t test (F) and two-tailed unpaired t test (G).
- (H) Representative confocal images of *Cacna1h-Cre::hM4Di* mice showing low and high hM4Di-mCherry virus expression in the mPFC. Scale bars, 500 μm .
- (I) Graphs illustrating the intensity infected by hM4Di-mCherry virus in the PL and the combined PL and IL regions of estrus females, plotted against the preference index.
- (J) Representative images illustrating proestrus and metestrus stages identified through vaginal cytology. Scale bar, 25 μm .
- (K) Chemogenetic manipulation of mPFC^{Cacna1h⁺} neurons in sociosexual preference assays.
- (L) Chemogenetic inhibition of mPFC^{Cacna1h⁺} neurons in female mice does not alter their investigation toward males during proestrus and metestrus phases. $n = 5-7$ mice/group. Two-way ANOVA, Bonferroni multiple comparisons tests.
- (M) Chemogenetic activation of mPFC^{Cacna1h⁺} neurons in females increases the social interest toward males during both proestrus and metestrus phases. $n = 5-6$ mice/group. Two-way ANOVA, Bonferroni multiple comparisons tests.
- * $p < 0.05$, **** $p < 0.0001$; n.s., not significant; data represent mean \pm SEM.



(legend on next page)

Figure S3. Estrous- and sex-dependent activity of mPFC^{Cacna1h+} neurons during social preference tests, related to Figure 4

- (A) Fiber photometry setup to record calcium signal of mPFC^{Cacna1h+} neurons during the sociosexual preference test.
- (B) Coronal section showing the expression of AAV1-Syn-Flex-GCaMP6f in the mPFC of Cacna1h-IRES-Cre mice with an optic fiber implanted above the virus infection site. Scale bars, 500 μ m (left) and 20 μ m (right).
- (C) The sample brain slices illustrating the infection site of AAV1-Syn-Flex-GCaMP6f-WPRE-SV40 virus in the mPFC.
- (D, G, and J) Quantification of sociosexual preference behavior in fiber photometry-recorded estrus female (D), diestrus female (G), and male mice (J). $n = 6$ –10 mice/group. Two-tailed unpaired t test (D–G) and Mann-Whitney test (J).
- (E) Heatmap of GCaMP6f signals in mPFC^{Cacna1h+} neurons as an estrus female (top) and a diestrus female (bottom) sniff a male. The GCaMP6f signal is aligned to the time point of sniffing onset. The color scale is determined by the normalized Z score.
- (F) Peri-event plot of Z-scored dF/F GCaMP6f signals when estrus and diestrus females sniffing males (left). Quantitative analysis of the change in calcium signals before and after the onset of sniffing males (right). $n = 6$ mice/group. Solid lines indicate mean. Shaded areas indicate SEM. Two-tailed unpaired t test.
- (H) Heatmap of GCaMP6f signals in mPFC^{Cacna1h+} neurons as an estrus female (top) and a diestrus female (bottom) sniff object.
- (I) Peri-event plot of Z-scored dF/F GCaMP6f signals when estrus and diestrus females sniffing objects (left). Quantitative analysis of change in calcium signals before and after the onset of sniffing objects (right). $n = 6$ mice/group. Solid lines indicate mean. Shaded areas indicate SEM. Two-tailed unpaired t test.
- (K) Heatmap of GCaMP6f signals in mPFC^{Cacna1h+} neurons as a male sniffs a female (top) and an object (bottom).
- (L) Peri-event plot of Z-scored dF/F GCaMP6f signals when males sniffing females and objects (left). Quantitative analysis of change in calcium signals before and after the sniffing onset (right). $n = 10$ mice/group. Solid lines indicate mean. Shaded areas indicate SEM. Mann-Whitney test.
- (M) Experimental setup for imaging neuronal activity during sociosexual preference test.
- (N–P) Heatmap of average peri-event calcium signals in individual mPFC^{Cacna1h+} neurons as estrus females (N), diestrus females (O), or males (P) sniff mouse of opposite sex and object, ranked by maximum response during 0–4 s after sniff onset.
- (Q) Experimental setup for imaging neuronal activity during sex preference test.
- (R–T) Heatmap of mPFC^{Cacna1h+} neuronal responses to sniffing female and male conspecifics in estrus females (R), diestrus females (S), and males (T). Peri-event calcium signals aligned to sniff onset (0 s).

* $p < 0.05$, ** $p < 0.01$, *** $p < 0.001$; n.s., not significant; data represent mean \pm SEM.

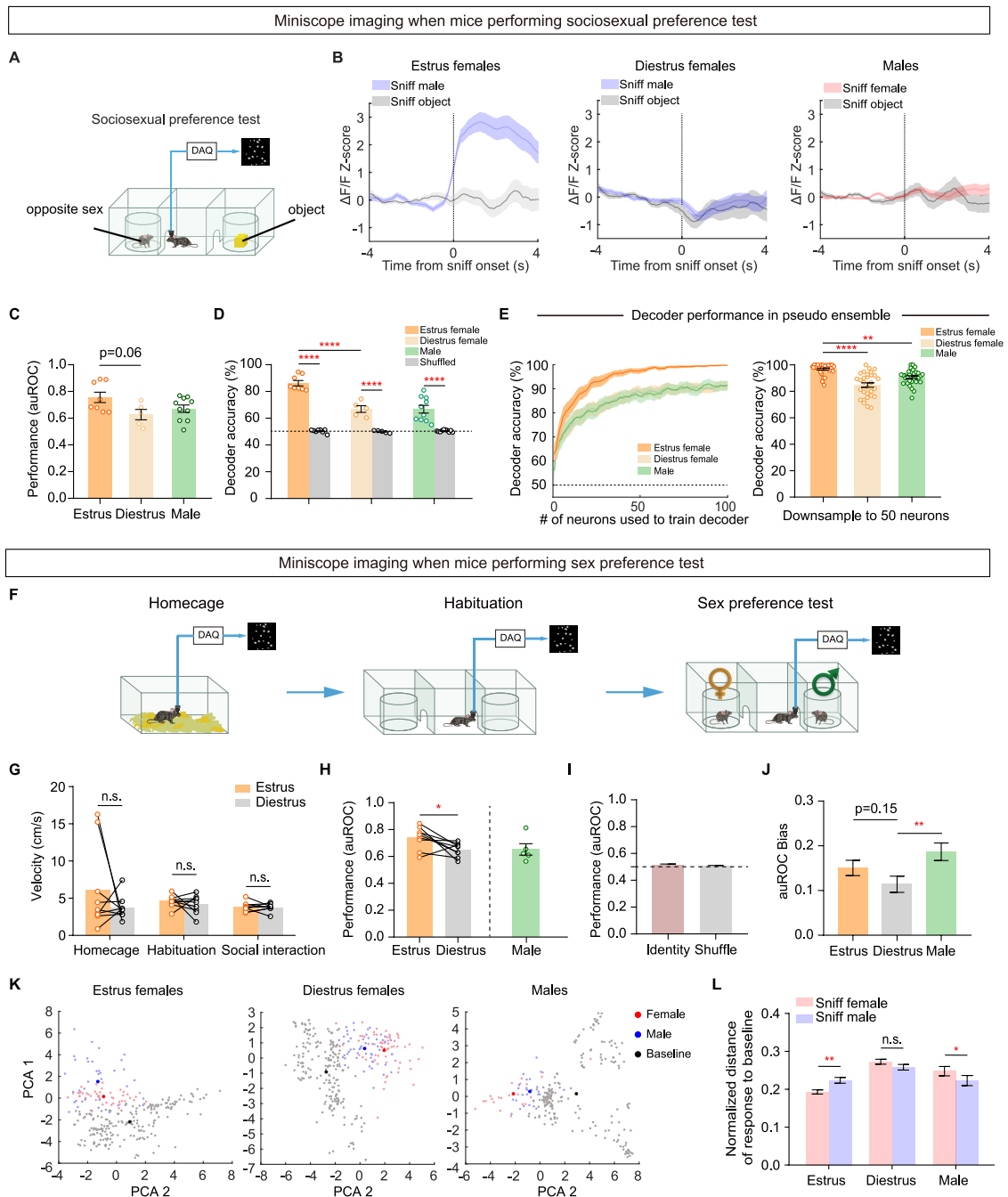


Figure S4. Estrous- and sex-dependent population coding of social stimuli by mPFC^{Cacna1h+} neurons, related to Figure 4

(A) Calcium imaging of mPFC^{Cacna1h+} neurons via Miniscope during sociosexual preference testing.
 (B) Bulk calcium signals from recorded neurons in estrus, diestrus females, and male mice during sniffing of opposite sex and objects.
 (C) Performance of unsupervised classifier (K-means clustering) distinguishing sniffing opposite sex vs. object using neural response during 0–2 s relative to sniff onset in estrus, diestrus females, and males ($n = 8$ estrus females, 5 diestrus females, and 10 males; one-way ANOVA, Bonferroni multiple comparisons tests).
 (D) SVM decoder performance distinguishing sniffing opposite sex vs. object based on neural responses 0–2 s post-sniff in estrus, diestrus females, and males ($n = 8$ estrus females, 5 diestrus females and 10 males; two-way ANOVA, Bonferroni multiple comparisons tests).
 (E) Classifier performance as a function of ensemble size (1–100) trained with pseudo neural ensembles recorded in estrus, diestrus females, and males (left). Classifier performance in randomly sampled 50 neurons from pseudo neuron ensembles recorded in estrus, diestrus females, and males (right) ($n = 30$ times bootstrap, one-way ANOVA, and Bonferroni multiple comparisons tests).
 (F) Calcium imaging of mPFC^{Cacna1h+} neurons with Miniscope in the homecage, during habituation in a three-chamber setup, and investigation in sex preference test.

(legend continued on next page)

(G) The velocity of estrus and diestrus females in homecage, during habituation, and in social investigation phases ($n = 9$ females; Wilcoxon matched-pairs signed-rank test is used if the data unsatisfied normal distribution test; otherwise, a paired t test is used).

(H) SVM classifier performance distinguishing male vs. female targets based on neural responses 0–2 s post-sniff onset in estrus females, diestrus females, and males ($n = 9$ females and 5 males; two-tailed paired t test).

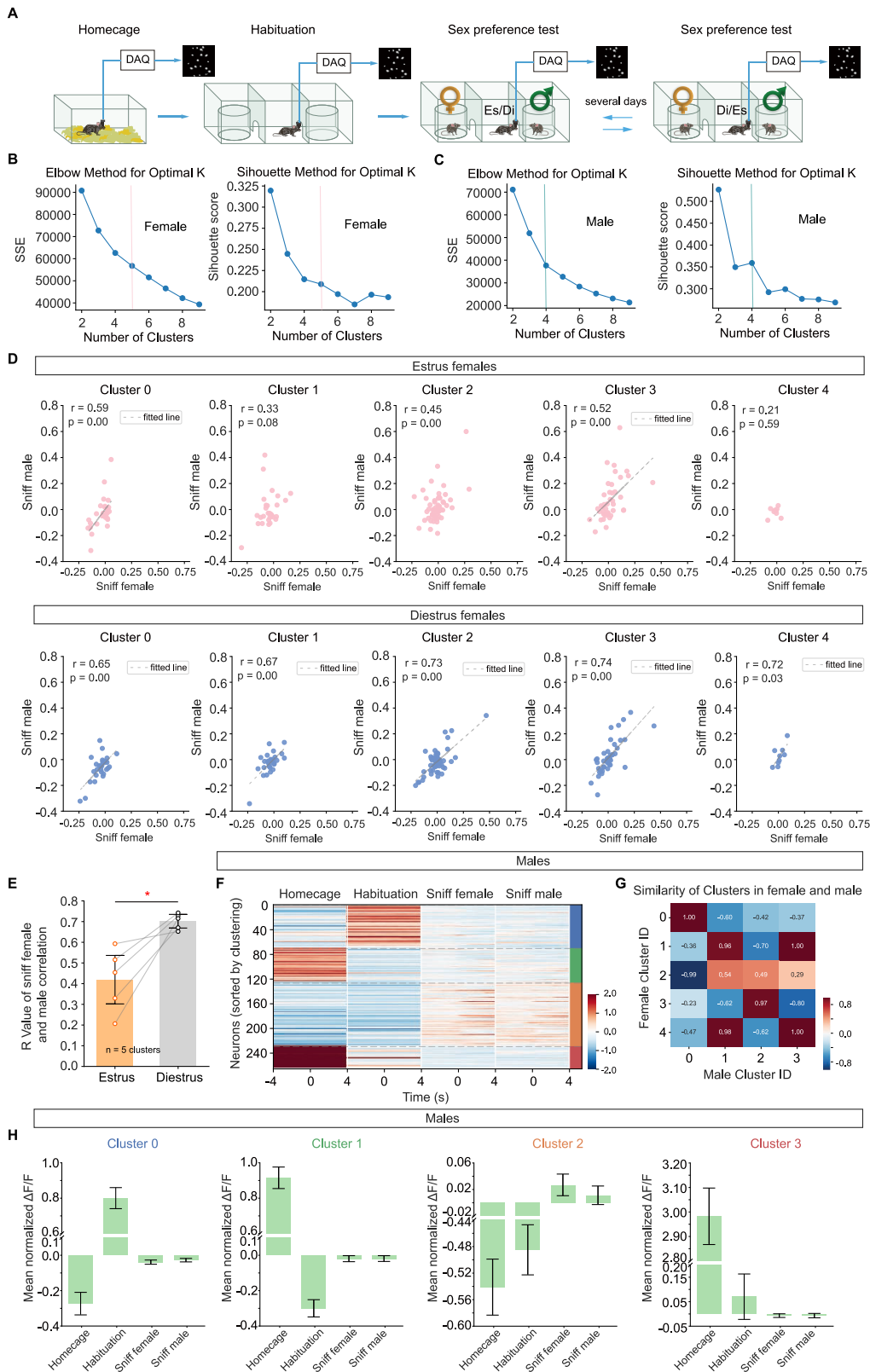
(I) Performance of SVM classifier in differentiating same-sex targets to assess the influence of mouse identity rather than sex on classifier accuracy, compared against label-shuffled data. $n = 8$ estrus females, 8 diestrus females, and 4 males.

(J) The auROC bias of same-sex excited neurons toward opposite-sex stimuli, calculated as $|\text{auROC} - 0.5|$ ($n = 38$ estrus neurons, 31 diestrus neurons, and 34 male neurons; one-way ANOVA, Bonferroni multiple comparisons tests).

(K) Example scheme of average male (blue) and female (red) sniffing trial activities within 2 s post-onset and a 10 s random baseline (gray, non-behavior time) projected onto a 2-dimensional principal component plane.

(L) Euclidian distance comparison of all trails from baseline in estrus, diestrus females and males ($n = 417$ female bouts vs. 353 male bouts in estrus females, 425 female bouts vs. 315 male bouts in diestrus females, and 215 female bouts vs. 201 male bouts in males).

* $p < 0.05$, ** $p < 0.01$, **** $p < 0.0001$; n.s., not significant; data represent mean \pm SEM.



(legend on next page)

Figure S5. Distinct mPFC^{Cacna1h+} neuron clusters exhibit sex- and estrous-dependent responses to social stimuli, related to Figure 5

(A) Timeline of sex preference test.

(B and C) K-means clustering evaluation for female (B) and male (C) mPFC^{Cacna1h+} neurons using the sum of squared errors (SSEs) and silhouette score. Optimal K determined by the elbow point in SSE and the local maximum in silhouette score.

(D) Linear regression of mPFC^{Cacna1h+} neuron activity of each cluster in response to sniff female and male stimuli during estrus (top) and diestrus (bottom). The fitted line is plotted only when r value > 0.5 and p value < 0.05 .

(E) Difference in correlation coefficients (r values) between mPFC^{Cacna1h+} neuron activity during sniffing female and male stimuli across estrus states ($n = 5$ clusters; two-tailed paired t test).

(F) Clustering of mPFC^{Cacna1h+} neurons in males. Colors on the right indicate different clusters.

(G) Similarity matrix of clusters identified in female and male mPFC^{Cacna1h+} neurons, based on Pearson correlation coefficients.

(H) Mean activity of mPFC^{Cacna1h+} neurons of each cluster in males.

* $p < 0.05$; data represent mean \pm SEM.

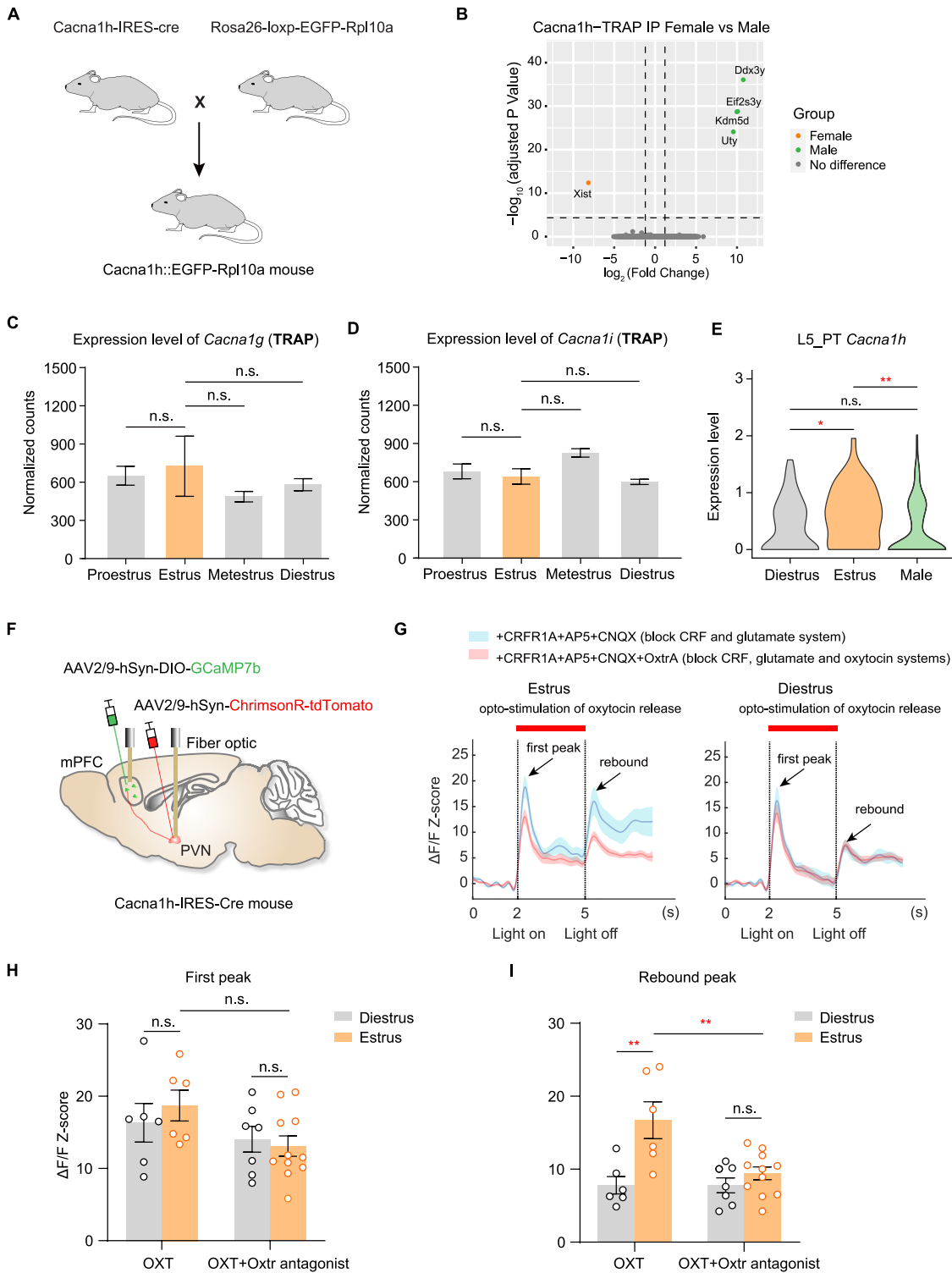


Figure S6. Translational profiling and oxytocin-evoked rebound excitation of mPFC^{Cacna1h+} neurons across estrous states, related to Figure 6

(A) Cacna1h-IRES-Cre mouse was bred to Rosa26-loxp-EGFP-Rpl10a mouse to generate Cacna1h-IRES-Cre::Rpl10a-EGFP mouse.

(B) Volcano plot for genes enriched in female vs. male mPFC^{Cacna1h+} IP samples identified by TRAP-seq. Green dots denote genes significantly enriched in male mPFC^{Cacna1h+} neurons with adjusted $p < 0.05$ and \log_2 fold change > 1.2 , and orange dots denote genes significantly enriched in the female mPFC^{Cacna1h+} neurons with adjusted $p < 0.05$ and \log_2 fold change < -1.2 . $n = 8$ female samples and 3 male samples.

(legend continued on next page)

(C and D) TRAP analysis of *Cacna1g* (C) and *Cacna1i* (D) expression in the mPFC of females across estrous phases ($n = 2$ samples/group, one-way ANOVA, and Bonferroni multiple comparisons tests).

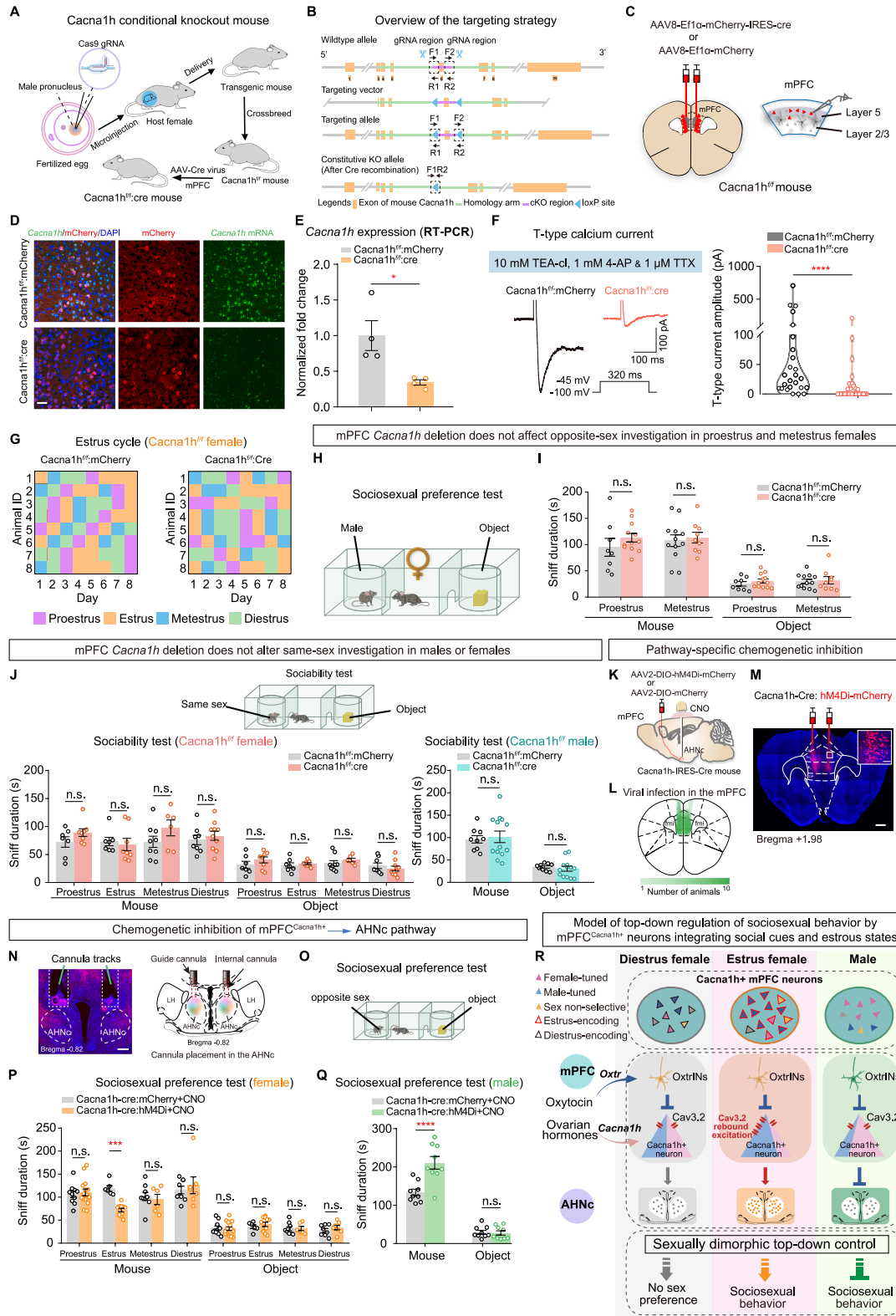
(E) Comparison of *Cacna1h* expression between diestrus, estrus female, and male in the L5_PT cell type identified by scRNA-seq.

(F) Viral injections and fiber implantations in *Cacna1h*-IRES-Cre mice. AAV2/9-hSyn-ChrimsonR-tdTomato was injected into the PVN for optogenetic activation of oxytocin release, and AAV2/9-hSyn-DIO-GCaMP7b was injected into the mPFC for calcium imaging of *Cacna1h*⁺ neurons. Optic fibers were implanted in the PVN for optogenetic stimulation and in the mPFC for fiber photometry.

(G) Average calcium activity of mPFC^{*Cacna1h*+} neurons in response to 3 s light stimulation of PVN neurons with pharmacological blockade of CRF, glutamate, or oxytocin signaling in estrus and diestrus female mice. The first peak following light onset suggests disinhibition of mPFC^{*Cacna1h*+} neurons, while the second peak after light offset indicates rebound activity. The right bar denotes the light stimulation period. CRFR1A, CRF receptor 1 antagonist; AP5, NMDA receptor antagonist; CNQX, AMPA/Kainate receptor antagonist.

(H and I) Quantification of Z-scored $\Delta F/F$ GCaMP7b signals for the first (H) and rebound (I) peaks of mPFC^{*Cacna1h*+} neuron activity in estrus and diestrus female mice. The amplitude of rebound activity, induced by oxytocin stimulation of inhibitory *Oxtr*-expressing mPFC neurons, was significantly higher in mPFC^{*Cacna1h*+} neurons during estrus compared with diestrus phases. *Oxtr* antagonist treatment abolished the increased rebound activity in estrus. Two-way ANOVA, Bonferroni multiple comparisons tests.

* $p < 0.05$, ** $p < 0.01$; n.s., not significant; data represent mean \pm SEM.



(legend on next page)

Figure S7. mPFC^{Cacna1h^{fl/fl}} neurons drive sexually dimorphic top-down control of sociosexual interest via AHNc-descending pathways, related to Figure 7

(A and B) Schematic representation of conditional *Cacna1h* knockout in the mPFC (A). Overview of the strategy for constructing the *Cacna1h^{fl/fl}* mouse line to conditionally knockout *Cacna1h* (B).

(C) Injection of AAV8-Ef1 α -mCherry-IRES-Cre or AAV8-Ef1 α -mCherry into the mPFC of *Cacna1h^{fl/fl}* mouse.

(D) Representative images of *Cacna1h* mRNA and virus expression in the mPFC of *Cacna1h^{fl/fl}* mice. Scale bar: 50 μ m.

(E) Quantification of *Cacna1h* mRNA expression in the mPFC using RT-qPCR in *Cacna1h^{fl/fl}*:mCherry and *Cacna1h^{fl/fl}*:Cre groups. $n = 4$ mice/group. Two-tailed unpaired t test.

(F) Electrophysiological validation of the conditional *Cacna1h* knockout in mPFC neurons. Representative traces of T-type calcium currents recorded from layer 5 pyramidal neurons in the mPFC slices of control (*Cacna1h^{fl/fl}*) and conditional *Cacna1h* knockout (*Cacna1h^{fl/fl}*; Cre) mice (left). Quantification of the peak T-type calcium current amplitude in layer 5 pyramidal neurons of the mPFC in control (*Cacna1h^{fl/fl}*) and conditional *Cacna1h* knockout (*Cacna1h^{fl/fl}*; Cre) mice (right). $N = 25$ –30 cells/group. Mann-Whitney test.

(G) Layout of the estrous states of *Cacna1h^{fl/fl}* female mice assigned by vaginal smear in 8 days.

(H) The strategy of sociosexual preference test.

(I) Conditional deletion of *Cacna1h* in the mPFC of female mice does not affect the duration of sniffing opposite sex during proestrus and metestrus phases. $n = 8$ –12 mice/group. Two-way ANOVA, Bonferroni multiple comparisons tests.

(J) Conditional deletion of *Cacna1h* in the mPFC of female and male mice did not affect sniffing same-sex social targets in females across estrous cycles (left) and males (right). $n = 6$ –13 mice/group. Two-way ANOVA, Bonferroni multiple comparisons tests.

(K) Pathway-specific chemogenetic inactivation strategy.

(L) Overlay of AAV8-Ef1 α -mCherry-IRES-Cre and AAV8-EF1 α -mCherry expression in the mPFC of *Cacna1h^{fl/fl}* mice. Green intensity indicates the number of mice with viral expression in each area.

(M) Coronal sections showing the expression of hm4Di-mCherry in the mPFC (scale bars, 100 μ m [inset] and 500 μ m).

(N) Coronal sections showing the cannula tracks above the mCherry⁺ axon terminals in the AHNc (scale bar, 200 μ m, left) and cannula locations of chemogenetic inhibition experiments (right).

(O) The strategy of sociosexual preference test.

(P and Q) Chemogenetic suppression of mPFC^{Cacna1h^{fl/fl}} neurons-AHNc pathway decreased sociosexual interests specifically when female mice in estrus. $n = 6$ –15 mice/group. Two-way ANOVA, Bonferroni multiple comparisons tests (P). Chemogenetic inhibition of mPFC^{Cacna1h^{fl/fl}} neurons-AHNc pathway in male mice enhanced their sociosexual preference for female mice. $n = 9$ mice/group. Two-way ANOVA, Bonferroni multiple comparisons tests (Q).

(R) Model of sexually dimorphic top-down regulation of sociosexual behavior by mPFC^{Cacna1h^{fl/fl}} neurons. In females, mPFC^{Cacna1h^{fl/fl}} neurons exhibit mixed representation of internal estrous state and target-sex information. During estrus phase, these neurons are tuned to male cues and display more selective encoding of male-related information. Ovarian hormones upregulate *Cacna1h*-encoded T-type calcium channels via a genomic pathway, enabling enhanced rebound excitation following inhibition from oxytocin-responsive interneurons. This modulation drives estrus-specific activity changes in mPFC^{Cacna1h^{fl/fl}} neurons, promoting sociosexual interests and sexual behavior through projections to the AHN. During diestrus, the low level of *Cacna1h* leads to insufficient T-type calcium channels, preventing the robust rebound activation observed in estrus females and ultimately diminishing selectivity for male cues compared with the heightened preference exhibited during estrus. Conversely, in males, mPFC^{Cacna1h^{fl/fl}} neurons are biased toward the representation of female cues. However, due to low *Cacna1h* expression, these neurons exhibit a primarily inhibitory response to sociosexual stimuli, suppressing sociosexual interests and sexual behavior via the AHN pathway.

* $p < 0.05$, ** $p < 0.001$, *** $p < 0.0001$; n.s., not significant; data represent mean \pm SEM.